DISS. ETH No. 21381

NUMERICAL ANALYSIS OF PHOTONIC NANO STRUCTURES IN LAYERED GEOMETRIES

A dissertation submitted to the

ETH ZÜRICH

for the degree of

Doctor of Sciences

presented by

AYTAÇ ALPARSLAN

B.S. in Electrical and Electronics Engineering
M.S. in Electrical and Computer Engineering
Koç University, Istanbul, Turkey

born January 23, 1983

citizen of Turkey

accepted on the recommendation of

Prof. Dr. Ch. Hafner, examiner
Prof. Dr. M. I. Aksun, co-examiner
Prof. Dr. L. Novotny, co-examiner

2013

DISS. ETH No. 21381

NUMERICAL ANALYSIS OF PHOTONIC NANO STRUCTURES IN LAYERED GEOMETRIES

A dissertation submitted to the

ETH ZÜRICH

for the degree of

Doctor of Sciences

presented by

AYTAÇ ALPARSLAN

B.S. in Electrical and Electronics Engineering
M.S. in Electrical and Computer Engineering
Koç University, Istanbul, Turkey

born January 23, 1983

citizen of Turkey

accepted on the recommendation of

Prof. Dr. Ch. Hafner, examiner
Prof. Dr. M. I. Aksun, co-examiner
Prof. Dr. L. Novotny, co-examiner

2013

Acknowledgments

This thesis was written as a result of the scientific research conducted at the Laboratory for Electromagnetic Fields and Microwave Electronics (*Institut für Feldtheorie und Höchstfrequenztechnik*, IFH) of the Swiss Federal Institute of Technology Zurich (*Eidgenössische Technische Hochschule Zürich*, ETH). The work was funded by the Swiss National Science Foundation (SNF No. 200021-119813/1).

First of all, I would like to thank my supervisor Christian Hafner for his scientific guidance and providing the financial support during my PhD studies. Instead of a boss he was a friend with whom I could discuss anything anytime (from politics to electromagnetics or organizing a good barbecue party). Without him and his implementation of MMP in an open source environment (OpenMaX), this thesis would not be possible. I also would like to thank Lukas Novotny who accepted to be a co examiner of this dissertation. His PhD thesis was a brilliant source which gave ideas and motivation during this work. A very special thanks go to my previous supervisor İrşadi Aksun, who first introduced me the analysis of layered media around the last year of my undergraduate studies. His encouragement and endless guidance throughout my scientific career, including this thesis, was irreplaceable. I thank him for teaching me how to conduct scientific research and being a good friend and a source of inspiration. I also thank him for accepting to be a co examiner in this thesis.

I also would like to acknowledge my friends I met during my time at IFH ETH Zürich. I very much enjoyed the countless lunches we went together with Dimitra Psychogiou, during which we shared ideas and discussed both scientific and personal issues. I knew that she was always there for a chat and I would like to thank her for being a best friend. I also cannot forget the time I spent with Jan Paška, including the pingpong matches, barbecues and sessions, thanks a lot dude! Finally my friends at the institute, Dr. Patrick Leidenberger, Dr. Johannes Hoffmann, Christoph Böcklin (also for translating the abstract), Dr. Sascha Schnepp, Dr. Dirk Baumann, Ueli Koch, Mustafa Boyvat, Mengyu Wang and Nemat Dolatsha I thank you guys for your friendship and numerous technical and non technical conversations we had.

The final thanks go to my family, who provided the endless support and love that made it easier for me to achieve my goals in life. Even if I did not call or come to visit you as much as a good son should, I know that you are always there and will always support me, thank you.

Abstract

Layered geometries play a very important role in electromagnetics (EM). Their unique features (guided/surface waves, localization of energy, transmission and reflection characteristics, etc) were used in a vast number of applications in the microwave and radio frequency regimes for decades. Recently, following the improvements in the fabrication techniques of structures with dimensions comparable with the wavelength of the visible spectrum, layered geometries have become quite popular in nano photonics. Following this increased interest, it has been highly desirable to analyze nano structures built in layered geometries in an efficient and reliable way. The method of multiple multipoles (MMP), which is a semi-analytic boundary discretization method, is a very strong candidate for such an analysis. But the complexity of classical MMP solutions (that use homogenous medium basis functions) increases dramatically with the number of layers, since special truncation techniques are needed for infinitely long boundaries of the layered media that requires advanced user experience. In order to tackle this problem and to use the advantages of MMP with no additional complexity, layered media Green's functions in 2D and 3D geometries are included in the MMP analysis.

In MMP, linear combinations of analytical solutions of Maxwell's equations (called expansions) are used for the general analysis of structures in presence of EM radiation. Therefore, the layered media Green's functions (which require the numerical evaluation of oscillatory and singular integrals, called Sommerfeld integrations) should be obtained with a high accuracy for using them as new expansion sets in MMP. In this thesis, numerical techniques for obtaining layered media Green's functions in 2D and 3D settings with very high accuracy, are introduced. The impact of the Sommerfeld integration path on the efficiency of layered media Green's function calculations is analyzed in detail. As a result of this analysis, several rules for the shape of the Sommerfeld integration path are introduced in order to obtain the layered media Green's functions for all kinds of material parameters and thickness values of layers. Computationally demanding numerical examples are also included, in order to demonstrate the efficiency of the technique together with discussions on important aspects.

Several unique updates are also introduced in the definition of layered media Green's functions in order to perform new types of analyses or to further decrease the complexity of the problems. One of these updates is the modified 2D layered media Green's functions with a nonzero out-of-plane wave vector component, used in the MMP eigenvalue analysis of 2D photonic waveguides in layered geometries (in commercial software literature this is often called mode

analysis). By this new technique it is possible to obtain all the physical eigenvalues (modes) of a waveguide in the range of interest, which is a demanding task for all of the well known numerical methods. The second unique update is the so called complex origin layered media Green's functions that changes the propagation pattern of fields generated by infinitesimal sources in layered geometries. This update uses the concept of complex origin multipole expansions in free space that produce beams. By using the complex origin layered expansions in MMP, it is possible to decrease the total number of expansions and the solution time for the simulations, especially for long structures compared to the wavelength. Finally, all the numerical tools needed and results of the derivations are documented as an appendix for writing a general computer code from scratch, that calculates the layered geometry Green's functions, including the updates mentioned above in 2D and 3D settings.

MMP, that is used extensively in the thesis, is described including a detailed analysis of the structure of the corresponding matrix equations. The details of the MMP scattering and eigenvalue analyses for the nano structures built in layered geometries are introduced and important aspects are addressed. Various numerical examples including the comparison of results with commercial software, scattering cross section calculations, implementation of complex origin layered expansions in MMP problems, eigenvalue analysis of plasmonic waveguides and optimization of nano structures are also presented to demonstrate the efficiency of the new method in the different analyses of nano structures in layered geometries. As a result of this work, a robust, reliable and efficient numerical tool for the analysis of nano structures in layered media is presented.

Zusammenfassung

Geschichtete Strukturen spielen seit langem eine grosse Rolle in der elektromagnetischen Feldtheorie. Deren spezielle Eigenschaften (geführte und Oberflächenwellen, Energielokalisation, Transmissions- und Reflexionscharakteristik, usw.) wurden über Jahrzehnte in unzähligen Anwendungen im Mikrowellen- und Radiofrequenzbereich ausgenutzt. Dank Fortschritten in der Herstellung von geschichteten Strukturen mit Dimensionen im Bereich der Wellenlänge des sichtbaren Lichts, haben sie auch weit verbreitet Anwendung gefunden in der Nanophotonik. Folglich entstand ein grosses Bedürfnis, Nanostrukturen in geschichteten Geometrien auch numerisch analysieren zu können. MMP (multiple multipoles), eine semi-analytische Grenzflächendiskretisierungsmethode, ist eine geeignete Methode für solche Berechnungen.

Die Komplexität von klassischen MMP Lösungen erhöht sich dramatisch mit der Zahl der Schichten. Zudem müssen die im Prinzip unendlich langen Grenzflächen in geeigneter Weise begrenzt werden, was viel Erfahrung des Benutzers erfordert. Um dem Abhilfe zu schaffen und die Vorteile von MMP ohne zusätzliche Komplexität ausnützen zu können, werden adaptierte Green's Funktionen für geschichtete 2D und 3D Strukturen als Neuerung in MMP eingeführt. Um die elektromagnetischen Felder in einer gewünschten Struktur mit MMP berechnen zu können, werden analytische Lösungen der Maxwell Gleichungen (genannt Entwicklungsfunktionen) gebraucht. Damit die Green's Funktionen für geschichtete 2D und 3D Strukturen als neues Set von Entwicklungsfunktionen für MMP verwendet werden können müssen sie mit hoher Genauigkeit berechnet werden können (dies erfordert die numerische Berechnung von oszilierenden und singulären Integralen, auch Sommfeld Integrale genannt). In der vorliegenden Dissertation werden numerische Methoden eingeführt, um diese Berechnungen mit sehr hoher Genauigkeit ausführen zu können. Ausserdem wird der Einfluss des Integrationspfades auf die Berechnungseffizienz des Sommerfeld Integrals im Detail analysiert. Daraus werden verschiedene Regeln für die Form des Sommerfeld Integrationspfades abgeleitet um die Green's Funktionen für verschiendenste Schichtdicken und Materialien effizient berechnen zu können. Die Leistungsfähigkeit und wichtige Aspekte der Technik werden anhand von rechenintensiven Beispielen demonstriert.

Die Green's Funktionen für mehrschichtige Strukturen werden mit einigen besonderen Erweiterungen versehen um neuartige Auswertungen vornehmen zu können oder Um die Komplexität des Problems weiter verringern zu können. Eine dieser Erweiterungen ist eine modifizierte 2D Greens Funktion für geschichtete Strukturen, die einen von null verschiedenen Wellenvektor aus der Ebene

heraus erlaubt. Dies wird in MMP für die Eigenwertberechnung von 2D photonischen Wellenleitern in geschichteten Strukturen benötigt (in komerzieller Software wird dies oft als Moden Analyse bezeichnet). Mit dieser neuen Technik ist es möglich, alle physikalischen Eigenwerte (Moden) eines Wellenleiters zu finden; etwas, was für alle bekannten numerischen Methoden eine herausfordernde Aufgabe ist. Die zweite Erweiterung sind die sogenannten Greens Funktionen für geschichtete Strukturen mit komplexem Ursprung die das Ausbreitungsmuster von Feldern verändern, die von einer infinitesimalen Quelle angeregt werden. Dies erlaubt die Reduktion der Zahl der Entwicklungsfunktionen und damit der Rechenzeit, speziell für Strukturen die gross sind im Verhältnis zur Wellenlänge. Diese Neuerung ist inspiriert vom Konzept der Multipol Entwicklung komplexen Ursprungs für homogene Geometrien.

MMP wird in der vorliegenden Arbeit intensiv gebraucht und wird deshalb detailliert beschrieben inklusive einer Analyse der Struktur der zugehörigen Matrix Gleichungen. Ebenso werden die Details und wichtige Aspekte der Streuprozess- und Eigenwertanalyse in MMP für Nano Strukturen in geschichteten Geometrien eingeführt und diskutiert.

Verschiedenste numerische Beispiele wie der Vergleich mit komerziellen Softwarepaketen, die Streuquerschnittberechnung, die Eigenwertanalyse von plasmonischen Wellenleitern und die Optimierung von nano Strukturen demonstrieren die Leistungsfähigkeit der neuen Methode.

Schliesslich werden alle benötigten numerischen Methoden und Herleitungen im Anhang zusammengefasst. Dies erlaubt die Entwicklung von Software Code für die Berechnung der Green's Funktionen inklusive der oben erwähnten Erweiterungen von Grund auf.

Aus der vorliegenden Arbeit resultiert ein zuverlässiges, robustes und effizientes numerisches Tool für die Analyse von Nanostrukturen in geschichteten Geometrien.

Contents

1 Introduction **1**
1.1 Outline of the thesis 4

2 Green's functions in layered media **7**
2.1 Introduction 7
2.2 Green's function in homogenous free space in 2D and 3D 8
2.3 Layered Media Green's Functions in 2D and 3D 9
2.4 Numerical implementation and Sommerfeld integration path . . . 11
2.5 Complex origin layered Media Green's functions in 2D and 3D . 17
2.6 A remark on time convention change 21

3 Method of Multiple Multipoles (MMP) **23**
3.1 Introduction 23
3.2 The method and the MMP matrix structure 25
3.3 MMP analysis of layered media 26
3.4 MMP error: a measure of accuracy with respect to analytical solution 28
3.5 Example: 2D Scattering analysis by MMP - a triangular particle in a three layered medium with plane wave incidence 29
3.6 Eigenvalue analysis of plasmonic waveguides by MMP 32
3.7 Example: Eigenvalue analysis by MMP - a metallic wire waveguide in a three layered medium 35

4 Numerical Results **41**
4.1 2D Scattering analysis: comparison by the commercial FEM software COMSOL Multiphysics 42
4.2 Complex origin layered expansions: decreasing computational effort 49
4.3 3D Scattering analysis: scattering cross section of a plasmonic particle in layered media 52
4.4 Eigenvalue analysis of plasmonic waveguides 60
4.5 Optimization of plasmonic structures 68

5 Conclusion **77**

A Building up Green's functions in layered media **81**
A.1 Contribution of direct terms 81

A.2 Reflection and transmission in layered media 83
A.3 Spectral domain Green's functions 84
A.3.1 The source and observation points are in the same layer . 85
A.3.2 The source layer is above the observation layer 86
A.3.3 The source layer is below the observation layer 87
A.4 Spatial domain Green's functions 88

Bibliography **91**

List of Publications **101**

Curriculum Vitae **105**

List of Figures

2.1 Definitions of the infinitesimal sources and the radial distances in homogenous free space 9
2.2 Definition of the coordinate system for general layered media . . 10
2.3 Deformed Sommerfeld integration path 12
2.4 Test geometry for the accuracy analysis of Sommerfeld integrations 14
2.5 Field continuity error for different choices of SIP in 2D for the test geometry 15
2.6 Field continuity error for different choices of SIP in 3D for the test geometry 15
2.7 Instantaneous Poynting vector in 2D for the test geometry 16
2.8 Instantaneous Poynting vector in 3D for the test geometry 16
2.9 The fields generated by complex origin point sources in free space 18
2.10 Complex origin Green's functions in spectral domain defined at the points in Fig. 2.9(a) 19
2.11 SIP modification for the complex origin infinitesimal sources . . . 19
2.12 Time averaged Poynting vector in 2D for the test geometry (complex origin source) 20
2.13 Time averaged Poynting vector in 3D for the test geometry (complex origin source) 21

3.1 An illustration of MMP analysis 25
3.2 The MMP matrix structure 26
3.3 Scattering analysis example by MMP: definition of the geometry and incident field 29
3.4 The solution of the example in Fig. 3.3 30
3.5 Expansion and error distributions of the example in Fig. 3.3 . . . 31
3.6 Eigenvalue analysis example by MMP: definition of the geometry and the expansion distribution 35
3.7 The MMP search function and the loci of the eigenvalues of the example in Fig. 3.6 as a function of λ_0 36
3.8 Eigenfields of the example in Fig. 3.6 at $\lambda_0 = 350nm$ 37
3.9 Results of the FEM eigenvalue analysis performed by Comsol for the even mode of the example in Fig 3.6 38
3.10 Results of the FEM eigenvalue analysis performed by JCM Suite for the even mode of the example in Fig 3.6 39

4.1 Measured permittivity values of Ag Au from popular sources in literature . . . 41
4.2 Scattering analysis: geometry and MMP setting definitions . . . 42
4.3 Scattering analysis: MMP results . . . 43
4.4 Scattering analysis: comparison with the commercial software, FEM mesh by Comsol. . . . 44
4.5 Scattering analysis: Comparison of MMP and commercial software results on the scatterer . . . 45
4.6 Scattering analysis: Comparison of MMP and commercial software errors on the scatterer . . . 46
4.7 Scattering analysis: Comparison of MMP and commercial software results on the metallic layer . . . 47
4.8 Scattering analysis: Comparison of MMP and commercial software errors on the metallic layer . . . 48
4.9 Complex origin expansions example: geometry definition and the settings of different MMP solutions . . . 50
4.10 The result of the problem shown in Fig. 4.9 . . . 51
4.11 Field and error values on the boundary of the scatterer for the problem shown in Fig. 4.9 . . . 51
4.12 The geometry definition for the 3D scattering cross section analysis 52
4.13 The MMP schematic for the 3D scattering cross section analysis 53
4.14 Scattering cross section for Ag particle . . . 55
4.15 Scattering cross section for Au particle . . . 56
4.16 The field profile for the Ag particle in free space at resonance. . . 57
4.17 The field profile for the Ag particle placed on top of a dielectric substrate ($\varepsilon_{r,sub} = 9.0$) at resonance. . . . 58
4.18 The field profile for the Ag particle placed on top of a Ag film with $t = 50$nm over a dielectric substrate ($\varepsilon_{r,sub} = 9.0$) at resonance. . 59
4.19 The loci of the eigenvalues of the Ag wire waveguide in dielectric slab with $\varepsilon_r = 2$ . . . 61
4.20 Eigenfields of the Ag wire waveguide analyzed in Fig. 4.19, evaluated at $\lambda_0 = 410$nm . . . 61
4.21 The loci of the eigenvalues of the Au wire waveguide in Ag backed dielectric slab with $\varepsilon_r = 2$ . . . 62
4.22 Eigenfields of the Au wire waveguide analyzed in Fig. 4.21, evaluated at $\lambda_0 = 550$nm . . . 63
4.23 The loci of the eigenvalues of the double Au wire waveguide in Ag backed dielectric slab with $\varepsilon_r = 2$ . . . 64
4.24 Eigenfields of the double Au wire waveguide analyzed in Fig. 4.23, evaluated at $\lambda_0 = 460$nm . . . 65
4.25 The loci of the eigenvalues of the single Au wire waveguide placed on a Ag backed dielectric slab with $\varepsilon_r = 2.25$ . . . 66

4.26 Eigenfields of the Au wire waveguide analyzed in Fig. 4.25, evaluated at $\lambda_0 = 510$nm 67
4.27 The geometrical setting of the optimization problem 68
4.28 The field generated by the monopole source without the cylindrical structures to be optimized 69
4.29 Distribution of the parameters obtained in the maximization problem 70
4.30 Distribution of the parameters obtained in the minimization problem 71
4.31 Field patterns of the optimized structures for the maximization problem 73
4.32 Field patterns of the optimized structures for the minimization problem 74
4.33 The effect of the distance between the two cylinders on the fitness value defined for the optimized structures for the maximization problem 75

5.1 Two different solutions obtained by different methods 78

List of Acronyms and Abbreviations

1D ..... one dimensional

2D ..... two dimensional

3D ..... three dimensional

ABC ..... absorbing boundary condition

BEM ..... boundary-element method

EM ..... electromagnetic

FEM ..... finite-element method

MMP ..... method of multiple multipoles

PEC ..... perfect electric conductor

PMC ..... perfect magnetic conductor

PML ..... perfectly matched layer

SIP ..... Sommerfeld integration path

SPP ..... surface plasmon polariton

SWP ..... surface wave pole

TE ..... transverse electric

TM ..... transverse magnetic

List of Symbols

f	frequency
ω	radial frequency
c_0	velocity of light in free space
$\mathbf{E}$	electric field strength vector
$\mathbf{H}$	magnetic field strength vector
$\mathbf{D}$	electric displacement vector
$\mathbf{B}$	magnetic induction vector
ε_i	dielectric permittivity of medium i
μ_i	magnetic permeability of medium i
ε_{ri}	relative dielectric permittivity of medium i
μ_{ri}	relative magnetic permeability of medium i
$\mathbf{A}$	vector potential
$\mathbf{J}$	current density vector
k_i	wave number of medium i
k_{Ki}	wave number of medium i in K-direction

1 Introduction

Through history, interaction of light with matter always attracted people's attention. Even without knowing the electromagnetic (EM) wave nature of light, innovative people were able to build optical structures to magnify objects or to focus or scatter light by using primitive lenses and mirrors in a trial and error fashion for centuries [1, 2]. Most of the ancient optical devices were built, analyzed and even upgraded by ray optics, which basically dictates that light propagates on straight lines originating from the source, which is easy to understand and observed vastly in nature. In addition to these devices (e.g. magnifying glass, microscope, gas lamps with curved mirrors, telescope, etc.), several devices were built based on pure empirical research, where the underlying scientific explanation was not understood. As an example, one of such empirically built (i.e. can not be described by ray optics) innovations of middle ages involving light was the tainted glass. By mixing tiny sparkles of gold (for reddish color) or silver (for yellowish color) with conventional glass, it was possible to fabricate tainted glasses [3, 4]. This phenomenon was not understood and attracted the interest of scientists for many years. In 1856, Michael Faraday came up with a description by analyzing the interaction between light and metallic particles from the perspective of an experimentalist [5]. Following Faraday's description, Gustav Mie came up with the analytical solution of Maxwell's equations for spherical particles [6] and made it possible to calculate the scattering and absorbtion cross section data of such structures in presence of electromagnetic (EM) radiation. By the Mie series solution, it became possible to analyze and understand the effects of the near field interactions of light with matter in nano scale, including the color change in tainted glass or the colorful nature of pigment-free butterfly wings that inspired numerous nano science researchers in designing devices using similar effects. As a result of the analyses and the theory he introduced, Mie is seen as one of the pioneers of numerical nanophotonics. Even today, the Mie series analysis of nano particles is very popular and several generalizations of the technique are used to analyze arbitrarily shaped nano structures in presence of EM radiation in an efficient and accurate way, e.g. the method of auxiliary sources [7] and the method of multiple multipoles (MMP) [8].

In addition to the improvements in the theoretical analysis of nano particles in the last century, there has been a vast interest and massive research conducted in the microwave and radio frequency spectra. In the late 19th - early 20th century, several experiments were done by numerous scientist including

Heinrich Hertz [9], Jagadish Chunder Bose [10], Karl Ferdinand Braun [11] and Guglielmo Marconi [12, 13]. In these experiments, it was shown that electromagnetic fields can propagate very large distances on earth and as a result, the new era of wireless communication was introduced to the scientific society [14]. Following the experiments, the theoretical analysis of electromagnetic radiation of EM waves over a lossy medium became a very popular topic in order to better design the first versions of today's widely used wireless communication systems. Theoreticians including Jonathan Zenneck [15] Arnold Sommerfeld [16] and Hermann Weyl [17] showed that the fields propagating over a lossy surface can be decomposed into different wave types, giving rise to efficient mathematical tools for the calculation of fields generated by a dipolar (infinitesimal) source in layered geometries, i.e. the layered media Green's functions. Using the linearity of Maxwell's equations in linear media, several numerical methods were introduced for the analysis of arbitrarily shaped objects in layered media, by using the corresponding Green's functions as the impulse response[1] of the layered medium [19, 20, 21, 22, 23, 24].

In the last two decades, the interest on the efficient and robust analysis of nano structures increased gradually. The main reason for this interest originates from the improvements in the fabrication process of structures with sizes comparable with the wavelength of the visible spectrum. In the literature, numerous applications were analyzed and built by tailoring the shape and material properties of the resonant structures including photonic crystals [25, 26, 27], solar cells [28, 29], high resolution microscopy systems [30, 31], chemical and bio sensors [32, 33, 34], and so on [35, 36]. In the numerical analysis of such devices, the general concept of electromagnetic field enhancement at optical frequencies through the use of nanostructures with dimensions smaller than a wavelength up to a few wavelengths can be described through the generic name of "nano antennas", in reference to their counterparts at radio frequency. Although Maxwell theory provides the main equations for the analysis of both optical and radio frequency antennas, the analysis and design of optical nano antennas is much more demanding mainly because of the highly dispersive[2], lossy[3] and plasmonic[4]

[1] The principle in signals and systems theory is applied here: if one knows the impulse response of a time invariant linear system (in EM, Green's functions), any signal in time (in EM interaction of EM waves with arbitrarily shaped objects in space) can be represented by a superposition of the corresponding impulse response [18].

[2] Permittivity of metals changes abruptly as a function of frequency in optics regime, as opposed to metals in radio frequencies where they are treated as perfect electric conductors (PEC) usually.

[3] The imaginary part of the permittivity is way higher compared to metals in radio frequency.

[4] The real part of the permittivity of metals can be negative, giving rise to surface waves called surface plasmon polaritons (SPP), generated by the oscillations of the electron gas on a metal-dielectric interface, that decay in both of the materials and can not be observed in radio frequency regime.

nature of metals at optical frequencies [37, 38, 39]. As a result of these facts, one should be always careful when solving problems in the optical regime by the tools developed for microwave applications. As an example, the well known resonance condition of the half wave dipole antenna length $L = \lambda_0/2$[5] should be updated for nano antennas, due to the characteristics of metals observed only at optical frequencies[6] [40]. Similarly, the well tested powerful simulation tools used in the microwave and radio frequencies (e.g. method of moments, finite element method (FEM), finite difference time domain method, etc.), should be updated or combined with other methods in order to capture the effect of SPPs in the analysis of nano structures in an efficient and accurate way, which is also the goal of this thesis.

As in the case of devices operating at microwave and radio frequency spectra, most of the nano devices are fabricated on a substrate or, in the more general case, in a multilayered medium. In the literature, the substrate is often ignored or replaced by a homogenous medium (e.g. [41]) for reasons of simplicity. Even if this technique works fine for specific layered geometry settings, it may also lead to substantial inaccuracies and it may even suppress strong effects such as field singularities in the triple points on the substrate. Furthermore, the layered geometry may support surface waves (e.g. SPP on metal layers, guided wave modes in dielectric layers) that are highly important and affect the results in an unpredictable way. Therefore, it is not safe to ignore the layered medium or replace it by a homogenous medium for the general analysis of photonic structures in layered media. In other words, in order to understand the related physical phenomena and to improve the efficiency of the devices, it is of most importance to analyze the layered media and include their interaction with the nano structures in the numerical analysis tools. In this thesis, a numerical method for the efficient analysis of nano structures in layered media is introduced by combining layered media Green's functions (used and tested for decades in microwave and radio frequency research) with MMP (used for the efficient semi-analytical EM analysis of nano structures) in order to combine the advantages of both methods. A similar work was presented by Lukas Novotny [42] for the scattering analysis of 3D structures in 1996 and in the present work, several updates are introduced in order to make the method more user friendly and applicable to the 2D scattering and eigenvalue analyses of photonic structures in layered media, as well.

[5] In the microwave and radio frequencies, waves with λ_0 are used to transmit and receive signals.

[6] For optical antennas the the half wave resonance condition should be updated as $L = \lambda_{eff}/2 < \lambda_0/2$ where λ_{eff} is the effective wavelength defined by the SPP resonances on the surface of the antenna as a function of the geometrical and material properties. The nano antenna with the length $L = \lambda_{eff}/2$ still receives and transmits waves with λ_0.

1.1 Outline of the thesis

In chapter 2, the layered Green's functions are derived both in spectral (spectrum: similar to frequency response in signals and systems) and spatial domains (space: similar to impulse response in signals and systems). Starting with the derivation of Green's functions in free space, the technique to obtain fields generated by infinitesimal sources in general 2D or 3D layered media is presented. In addition, the concept of complex origin Green's functions for layered media is introduced in section 2.5. In the end, all the numerical tools, techniques and results of derivations needed for the efficient calculation of spatial domain Green's functions in layered media is presented in appendix A. It should be noted that the fundamental EM derivations that can be found in any EM book (e.g. in [43, 44]) or in a previous work of the author [45] are not included here in this thesis again, in order to introduce a work that points out the important and tricky aspects of the method in a compact way.

In chapter 3, the fundamental aspects of MMP updated by the layered media Green's functions (in the MMP jargon called layered expansions) are discussed. Starting with the scattering analysis, a step by step description is carried out, including a detailed analysis of the entries of the underlying matrix equation. In section 3.6, the eigenvalue analysis of photonic waveguides in layered geometries, performed by MMP together with the modified 2D layered geometry Green's functions, is introduced. As in the discussions on the layered geometry Green's functions in chapter 2, only the important aspects needed to write an MMP routine from scratch are included in chapter 3, whereas detailed information on the method is left to interested readers to follow in the works of Christian Hafner [46, 8]. In this chapter, two numerical examples are also included to describe the MMP analysis steps for photonic structures in layered geometries.

In chapter 4, several numerical examples are analyzed by the method introduced. In section 4.1, an accuracy analysis of one of the most popular commercial FEM software COMSOL Multiphysics is introduced by using the reference solutions obtained by MMP with layered expansions. In the following section, the concept of complex origin layered expansions is tested and it is shown that when used properly, complex origin expansions can decrease the computational costs of MMP solutions. In section 4.3, a 3D scattering cross section analysis [47] is presented for different plasmonic particles in layered geometries with variable thickness and material property values. In the next section, an eigenvalue analysis is introduced for plasmonic waveguides with different material and geometrical features. Finally, an optimization problem in a 2D plasmonic structure is analyzed, by using layered MMP with a evolutionary strategy optimizer routine.

In this thesis, all the results and field plots are obtained by the open source simulation package OpenMaX (ver 2013A [48]) that includes the latest version

of MMP and the layered expansions. In addition, the numerical tools already available in OpenMaX (e.g. numerical integrators and optimization routines) are used during the analyses, if not stated otherwise.

2 Green's functions in layered media

2.1 Introduction

Green's functions in electromagnetics (EMs) are the fields and potentials generated by an infinitesimal time harmonic source in the corresponding numerical medium. Depending on the dimension of the medium, the infinitesimal source becomes a plane in 1D (generating plane waves), a line in 2D (generating cylindrical waves) and a point in 3D (generating spherical waves). For homogenous isotropic media, the Green's functions for the fields and potentials have closed form representations making it easy and efficient to use them in numerical methods [8]. In presence of a layered medium, only 1D Green's functions (propagation of plane waves in multilayered media) can be obtained analytically. The layered media Green's functions in 2D and 3D can only be obtained by using 1D Green's functions. Realization of this technique dates back to 1909 when A. Sommerfeld showed that the fields generated by a vertical dipole over a lossy substrate can be approximated by the superposition of spherical and surface waves [16, 49]. Then in 1919, H. Weyl introduced the mathematical link between the 1D and 3D Green's functions which shows that the spherical waves are the superposition of plane waves that propagate in all directions (Weyl identity) [17]. After these works, it was possible to obtain the fields and potentials generated by the infinitesimal sources in general layered media, by introducing the reflection and transmission data of distinct plane waves propagating inside the corresponding layers.

Since the spectrum of a single infinitesimal source in 2D and 3D are continuous (including evanescent waves), the summation operation of plane waves becomes an oscillatory and slowly decaying integration with infinite bounds, called the Sommerfeld integral or the Hankel transform. In general, the direct computation of such integrals is numerically demanding. Faster and yet efficient calculations of these integrals became very popular and several techniques were proposed, including but not limited to: 1) changing the integration path so that the integrands decay faster making the integration quicker [42, 50, 51], 2)integration and summation technique which predicts the behavior of the integrands for large integration parameters by integrating a finite part of it [52], or 3) approximating the integral by the fields (or potentials) generated by a finite set of infinitesimal sources in free space [53, 54, 55, 56, 57].

This chapter starts with an analysis of Green's functions in free-space in order to get a physical insight to the wave types generated by infinitesimal

sources. Then, the Green's functions for layered media are analyzed in 2D and 3D [58, 59, 45]. All the needed numerical tools are provided in appendix A, in order to perform a full field analysis in all the layers. The effect of the Sommerfeld integration parameters on the accuracy of results and the concept of complex origin layered media Green's functions are also provided in this chapter. It should be noted that the results obtained here are not limited to MMP (as demonstrated in chapters 3 and 4) but can also be used in other numerical methods including method of moments (MoM) [60, 61], boundary element method (BEM) or BEM-finite element method (FEM) coupling [62, 63].

2.2 Green's function in homogenous free space in 2D and 3D

In a linear homogenous and isotropic medium i the electric and magnetic field components can be obtained in terms of vector and scalar potentials defined in the same medium i by taking the spatial derivatives according to the well know relations [58, 59, 45]:

$$\mathbf{E}(\mathbf{r}) = -j\omega\mathbf{A}(\mathbf{r}) - \nabla\phi(\mathbf{r}) \tag{2.1}$$

$$\mu_i\mathbf{H}(\mathbf{r}) = \nabla \times \mathbf{A}(\mathbf{r}) \tag{2.2}$$

where $\phi(\mathbf{r})$ and $\mathbf{A}(\mathbf{r})$ are the scalar and vector potentials, respectively. They are related to each other by the Lorentz gauge as

$$\nabla \cdot \mathbf{A}(\mathbf{r}) = -j\omega\varepsilon_i\mu_i\phi(\mathbf{r}) \tag{2.3}$$

It should be noted that the time dependency $e^{j\omega t}$ is used for the derivation in this chapter and dropped from the formulae (e.g. $\mathbf{A}(\mathbf{r},t) = \mathbf{A}(\mathbf{r})e^{j\omega t}$ holds for all the fields and potentials). Combining (2.1), (2.2) and (2.3) the governing equation for the vector potential is obtained as:

$$\nabla^2\mathbf{A} + k_i^2\mathbf{A} = -\mu_i\mathbf{J} \tag{2.4}$$

where $k_i = \omega\sqrt{\varepsilon_i\mu_i}$ is the wave number in medium i and $\mathbf{J}$ is the current source. Depending on the dimension of the geometry, the right hand side of (2.4) takes the different values as shown in Fig. 2.1 with the following solutions:

$$\mathbf{A}(\rho) = \hat{\mathbf{y}}\mu_i\frac{jH_0^{(2)}(k_i\rho)}{4} \quad \text{in 2D} \tag{2.5}$$

$$\mathbf{A}(r) = \hat{\alpha}\mu_i\frac{e^{-jk_ir}}{4\pi r} \quad \text{in 3D} \tag{2.6}$$

fulfilling the out going wave conditions and α is the arbitrary direction of the current element. Once the potential information is calculated, the field components can be obtained by (2.1) and (2.2), which are provided in Section A.1. It

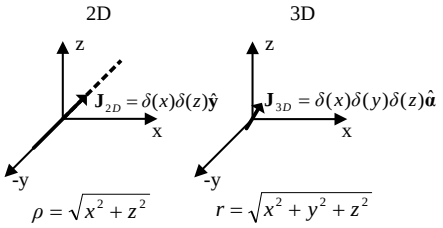

Figure 2.1: Definitions of the infinitesimal sources and the radial distances in homogenous free space

should be noted that the field components obtained here are used to obtain the Green's functions in a layered geometry, when the source and the observation points are in the same layer.

2.3 Layered Media Green's Functions in 2D and 3D

As mentioned earlier, it is not possible to obtain the layered media Green's functions in closed form, as opposed to the results obtained in Section 2.2. In this section, the technique to obtain the layered media Green's functions in the spectral (spectrum) and spatial (space) domains is provided, according to the coordinate system in Fig. 2.2.

The Green's functions generated by an infinitesimal source in homogenous space (suppose all the layers are the same in Fig. 2.2) can be related to the superposition of plane waves propagating in all the directions by the Weyl identity (compare with (2.6)):

$$\frac{e^{-jk_i r}}{r} = \frac{1}{\pi}\int_{-\infty}^{\infty}\int_{-\infty}^{\infty} dk_x dk_y e^{-jk_x x - jk_y y}\frac{e^{-jk_{zi}|z|}}{j2k_{zi}} \text{in 3D} \tag{2.7}$$

where $k_{K(i)}$ is the wave vector component in K-direction (in layer i) and fulfill the condition $k_i^2 = k_x^2 + k_y^2 + k_{zi}^2$. The Weyl identity can also be used for 2D Green's functions by setting the out-of-paper wave vector component to a complex constant, i.e. $k_y = k_\gamma$ in (2.7) according to Fig. 2.2, which results in the following (compare with (2.5)):

$$\frac{H_0^{(2)}\left(k_\kappa\sqrt{x^2+z^2}\right)e^{-jk_\gamma y}}{2j} = \frac{1}{\pi}\int_{-\infty}^{\infty} dk_x e^{-jk_x x}e^{-jk_\gamma y}\frac{e^{-jk_{zi}|z|}}{j2k_{zi}} \tag{2.8}$$

where $k_i^2 = k_\kappa^2 + k_\gamma^2$. In (2.8), the in-plane cylindrical wave ($H_0^{(2)}$) is modulated by the plane wave that propagates in y direction ($e^{-jk_\gamma y}$). The plane wave

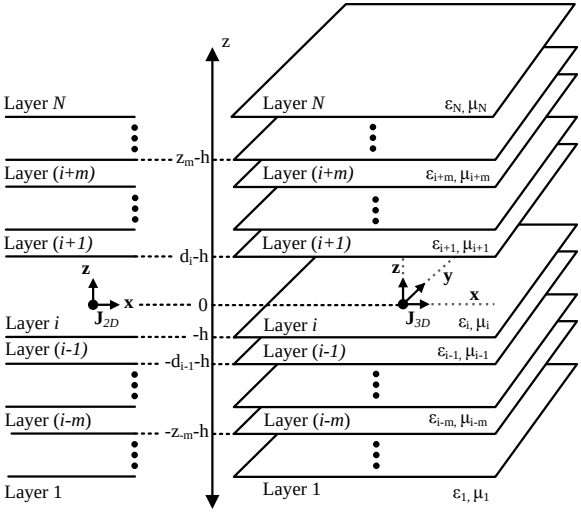

Figure 2.2: Definition of the coordinate system for general layered media

in y direction can be treated exactly in the same way as the time convention exponential $e^{j\omega t}$ (i.e. $d/dt = j\omega$ and $d/dy = -jk_\gamma$)[8]. In addition, without loss of generality, y variable can be set to 0, since if one knows the field pattern at $y = 0$, the field pattern at all y values can be obtained, by the multiplication of the plane wave $e^{-jk_\gamma y}$. In the case $k_\gamma = 0$, the field propagates only on the XZ plane, which can be used for the in-plane wave scattering analysis of 2D structures. When $k_\gamma \neq 0$, the field generated by the line source will propagate in all directions. By using these fields, the full wave scattering analysis of 2D structures and the eigenvalue analysis of wave guides can be performed as discussed in chapter 3.

An equivalent form of (2.7) is the Sommerfeld identity by which the Green's functions are obtained by the superposition of cylindrical waves in the lateral direction ($\rho = \sqrt{x^2 + y^2}$ and $k_\rho^2 = k_x^2 + k_y^2$) and the corresponding plane waves in the perpendicular direction as:

$$\frac{e^{-jk_i r}}{r} = \int_{-\infty}^{\infty} dk_\rho k_\rho H_0^{(2)}(k_\rho \rho) \frac{e^{-jk_{zi}|z|}}{j2k_{zi}} \tag{2.9}$$

Analyzing the layered geometry in Fig. 2.2 reveals that the Sommerfeld identity can be used to obtain the layered media Green's functions as well, since there is no material property discontinuity in the lateral direction. As a result, a

discrete value of k_ρ in (2.9) (or k_x in (2.8)) will be the same in all the layers and only k_z will change in different media. As a result, the magnitudes of the plane waves will be different for each angle of incidence (i.e. depending on k_z) related by the reflection/transmission coefficients. In order to plug in the effect of the layered media, the propagation profile of the plane wave in all the layers should be provided (a plane wave propagation tool written in MATLAB® can be obtained from [45]). Once this information is obtained, the identities (2.8) and (2.9) get the following forms:

$$G_{2D} = e^{-jk_\gamma y}\frac{1}{2\pi}\int_{-\infty}^{\infty} dk_x e^{-jkx}\tilde{G}(k_x)$$
$$G_{3D} = \frac{1}{4\pi}\int_{-\infty}^{\infty} dk_\rho k_\rho H_0^{(2)}(k_\rho\rho)\tilde{G}(k_\rho) \tag{2.10}$$

which are called the inverse Fourier and Hankel transforms, respectively. Comparing these integrals with (2.8) and (2.9) reveals that the plane wave propagating in z direction inside a homogenous medium is changed by the spectral domain Green's function $\tilde{G}$. The effect of the layered media in presence of the plane waves propagating in z direction is contained in the spectral domain Green's function and has exactly the same formulation for the 2D and 3D geometries. In a given layer j, the spectral domain Green's function is obtained by the superposition of two waves: 1) a plane wave propagating upwards ($e^{-jk_{zj}z}$) and 2)a plane wave propagating downwards ($e^{jk_{zj}z}$). Depending on the type of the spatial domain Green's function, the magnitudes of these waves are determined by the properly defined boundary and phase matching conditions. In addition, when the source and the observation points are in the same layer, the homogenous medium Green's functions, the so called direct terms, should be added in the spatial domain. The detailed derivation of the Green's functions for layered media is not included here, since it was done in a previous work of the author [45]. Instead, all the needed tools for the calculation of layered media Green's functions for fields in 2D and 3D are provided in appendix A, including the definitions of the reflection, transmission and amplitude transfer functions, integration rules and the spectral domain Green's functions for all the layers.

2.4 Numerical implementation and Sommerfeld integration path

The Sommerfeld integrals in (2.10) are defined to be evaluated along the real axis of the complex k_ρ (k_x in 2D) plane [58]. The spectral domain Green's functions can be singular on the real axis (e.g. when all the materials in the layered media are lossless, the surface wave poles (SWPs) and the branch points are purely real [45, 64]), which makes the Sommerfeld integral undefined. In order to overcome this problem there are two methods: 1) subtract the singularities

from the integrands by Cauchy integration formula, perform the integration and add the contributions in spatial domain or 2) deform the Sommerfeld integration path (SIP) so that it does not cross any of the singularities. The first solution needs the exact locations of the singularities which can be a numerically expensive task, depending on the geometrical and material property specifications of the layered medium [65]. The second method of calculating the integrals is more robust, especially when the fields are calculated to be used in a general numerical method. An example of such a SIP can be seen in Fig.2.3 with the definitions of the parameters S_1 and S_2 to control the shape, where k_{max} is the maximum wave number of the layered geometry.

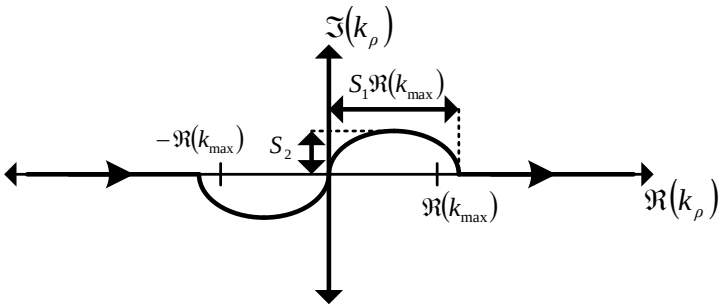

Figure 2.3: Deformed Sommerfeld integration path

In the numerical implementation, an adaptive 3^{th} order Gauss-Kronrod quadrature routine that simultaneously integrates the spectral domain Green's functions is used as follows: 1)Integrate the similar integrands simultaneously along the deformed path directly (i.e. along $k_\rho + jS_2 \sin((\pi k_\rho)/S_1\Re(k_{max}))$ with $-S1\Re(k_{max}) < k_\rho < S1\Re(k_{max})$) 2) Use integration-and-summation technique by the weighed averages [52] or change the remaining part of the path so that it goes in parallel with the $\Im(k_\rho)$ axis [42, 50] for the remaining part of the simultaneous integration. At this point, analyzing the spectral domain Green's functions as provided in appendix A.3 reveals that there are three different types of integrands: 1)transverse electric (TE) type (e.g. $\tilde{G}_1$), 2)transverse magnetic (TM) type (e.g. $\tilde{G}_6$) and 3)TE-TM type (e.g. $\tilde{G}_2$). By using this fact in the numerical implementation, the common quantities such as the reflection/transmission coefficients and amplitude transfer functions are evaluated only once for the similar type of integrands. As a result, by using a simultaneous integration routine, the computational cost for obtaining all the field components is reduced significantly ($\sim 1/3$ in 2D and $\sim 1/8$ in 3D), compared to separate integrations.

Deforming the integration path is mathematically allowed by the Cauchy theorem [58]. However, the numerical implementation of such integrals can introduce errors once the SIP is deflected too much (i.e. the integration becomes inaccurate in capturing the effects of singularities, if they are very far away from the SIP) or not enough (i.e. integration becomes numerically ill-defined when the SIP passes very close to the singularities) from the real k_ρ axis. This can be troublesome especially when high accuracy results are needed, as in the case of MMP which is introduced in chapter 3.

In order to demonstrate the effect of the integration parameters on the accuracy of the Sommerfeld integrations, the Green's functions of the three layered geometry in Fig. 2.4 are calculated for 2D and 3D infinitesimal sources, with different combinations of the parameters S_1 and S_2 (in this example integration-and-summation technique is used [52] with the relative accuracy of 10^{-9} for the integration routine). Physically, the structure in Fig. 2.4 is a silver backed dielectric slab analyzed at $\lambda_0 = 633$nm. In order to make the problem numerically difficult and to see the limits of the Sommerfeld integration, the imaginary part of the dielectric constant ($\varepsilon_{r,Ag} = -18.10 - j0.48$ [66]) of silver is removed. As a result, all the SWPs ($k_{TE,1} = 1.21k_0, k_{TE,2} = 1.68k_0, k_{TE,3} = 1.92k_0, k_{TM,1} = 1.43k_0, k_{TM,2} = 1.86k_0$) including the surface plasmon polariton (SPP) pole (wave number) ($k_{TM,spp} = 2.27k_0$), lie on the real k_ρ axis giving rise to a worst case scenario for the Sommerfeld integrations.

As discussed earlier, the direct wave terms are obtained analytically by the Weyl or Sommerfeld identities, and added in the spatial domain, when the observation point is in the source layer. The spatial domain Green's functions resulting from the reflections and transmissions in the source and the neighboring 2 layers are obtained by using the SIP in Fig. 2.3. Therefore the accuracy of the Sommerfeld integrations can be monitored by an analysis of the the continuity equations of the fields (which are built by the combination of analytical and numerical results) defined at the boundaries of the source layer as follows:

$$\begin{aligned} \mathbf{E}_{i,t}(N_k) &= \mathbf{E}_{j,t}(N_k) \\ \mathbf{H}_{i,t}(N_k) &= \mathbf{H}_{j,t}(N_k) \\ \varepsilon_{ri}\mathbf{E}_{i,n}(N_k) &= \varepsilon_{rj}\mathbf{E}_{j,n}(N_k) \\ \mu_{ri}\mathbf{H}_{i,n}(N_k) &= \mu_{rj}\mathbf{H}_{j,n}(N_k) \end{aligned} \tag{2.11}$$

where N_k is a given boundary condition check point, i (= 2) and j (= 1 or 3) are the indices of the source and observation points, respectively, as shown in Fig.2.4, together with the location of the infinitesimal sources. The subscripts t and n denote the tangential and normal components of the vector fields, respectively. In 2D, two line sources carrying electric and magnetic currents in z direction, with $k_\gamma = 0$, are used. Likewise in 3D, two point sources carrying

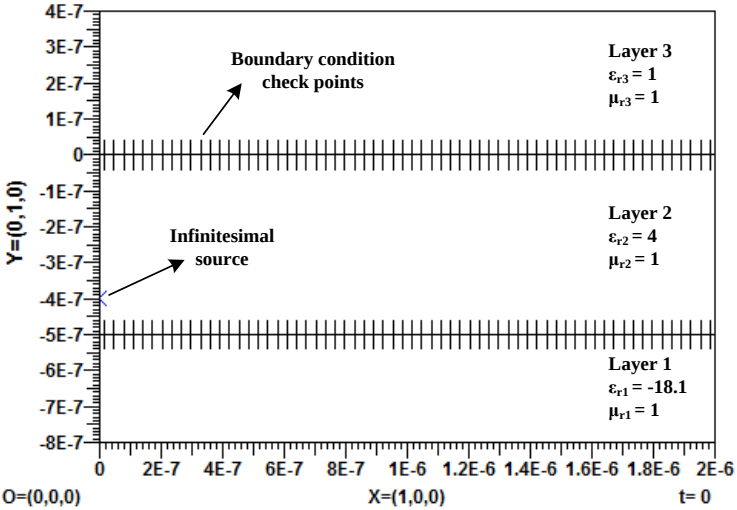

Figure 2.4: Test geometry for the accuracy analysis of Sommerfeld integrations: A silver backed dielectric slab in free space to be analyzed at $\lambda_0 = 633$nm. The imaginary part of silver (layer 1) is not included in the calculations, in order to make the test problem numerically demanding.

magnetic and electric currents in the direction of the vector $(1, 1, 1)$ are used[1]. Below, the average full field continuity error introduced by the Sommerfeld integration path for the 2D and 3D infinitesimal sources are plotted in Fig. 2.5 and 2.6,respectively. The error measure is defined in the normalized square sense for all the three field components, as classically done in the MMP analysis described in chapter 3 (refer to (3.3)).

One can see that, with the correct choice of the parameters, very accurate results ($>$ 7 significant digits in 2D and $>$ 6 significant digits for 3D) can be obtained, even for the numerically challenging example given here. The parameter S_1 should be selected carefully so that the integration path does not cross the singularities due to the SPP resonances observed on the boundary between metals and dielectrics [65]. The effect of bad choices of S_1 can be observed when $S_1 < \Re(k_{TM,spp})/\Re(k_{max}) \approx 1.14$ as plotted in Fig. 2.6 and the H-monopole case of Fig. 2.5. Such an effect is not observed in the E-monopole case, since the corresponding integrands are built only by TE mode components

[1] $\mathbf{z} \rightarrow \mathbf{y}$,$\mathbf{y} \rightarrow -\mathbf{z}$ and $\mathbf{x} \rightarrow \mathbf{x}$ is used to transform the geometry shown in Fig. 2.2 to the one used here. This mapping will be used in the upcoming numerical results throughout the thesis, without loss of generality.

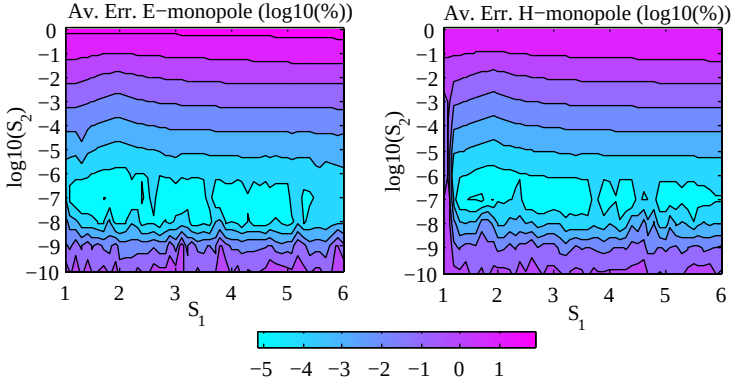

Figure 2.5: Field discontinuity error percentage in logarithmic scale for 2D line sources (monopoles) evaluated at 64 boundary condition check points for each boundary (as exactly seen in Fig. 2.4).

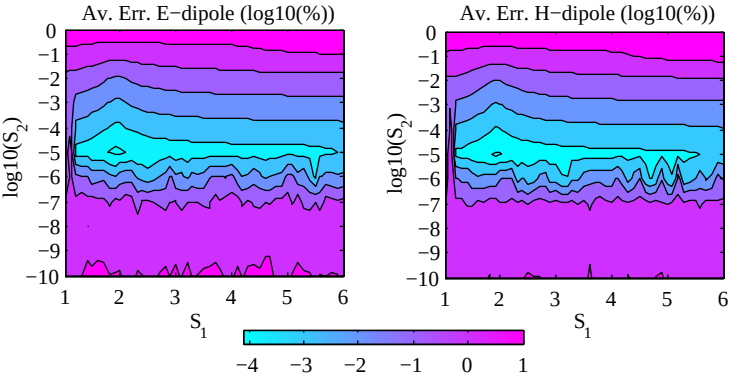

Figure 2.6: Field discontinuity error percentage in logarithmic scale for 3D point sources (dipoles) evaluated at 314 boundary condition check points for each boundary (instead of 64 points as seen in Fig. 2.4, 10 points are used and rotated 2π around y axis $(10)^2\pi \approx 314$).

when $k_\gamma = 0$ (refer to (A.18)). In order to be sure that there is no inaccuracy originating from the SIP when using the Green's functions in numerical methods, one should perform an analysis similar to the one described here and choose the parameters according to the accuracy needed. Two examples of the Green's functions obtained by the integration technique described here can be seen in Fig. 2.7 and 2.8.

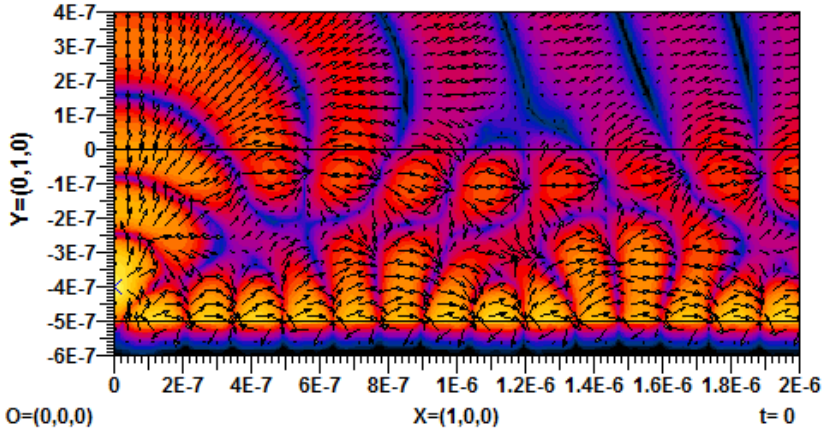

Figure 2.7: Surface: the instantaneous Poynting vector magnitude generated by a 2D magnetic line source (z-directed) with $\lambda_0 = 633$nm, located at $(0, -400)$nm in logarithmic scale with $k_\gamma = 0$. Arrows: Direction of power flow. The parameters $S_1 = 1.7$ and $S_2 = 10^{-7}$ are used to get the results with the average relative error of $\%6.25 \times 10^{-6}$.

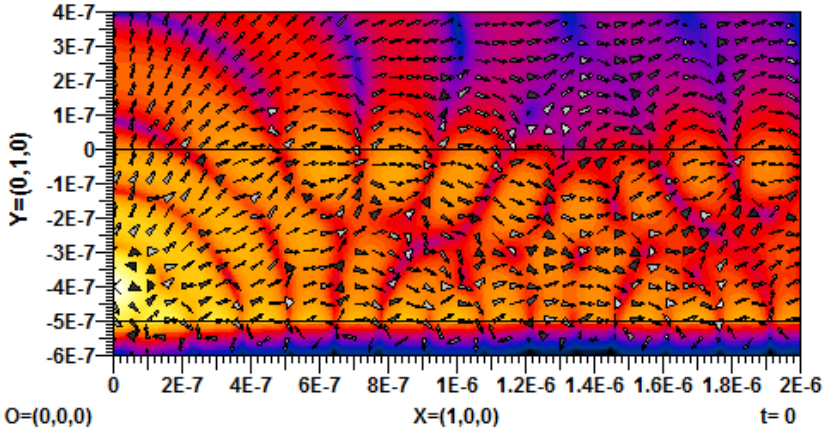

Figure 2.8: Surface: the instantaneous Poynting vector magnitude generated by a 3D electric point source (in the direction of the vector $(1, 1, 1)$) with $\lambda_0 = 633$nm located at $(0, -400, 0)$nm in logarithmic scale on $z = 0$ plane. Arrows: direction of power flow. The parameters $S_1 = 1.9$ and $S_2 = 10^{-5}$ are used to get the results with the average relative error of $\%5.67 \times 10^{-5}$.

2.5 Complex origin layered Media Green's functions in 2D and 3D

In this section, an update for the layered media Green's functions is introduced by the concept of complex origin for infinitesimal sources. This technique is used in the computational EM community mainly to reduce the numerical effort and complexity of simulations [51, 54, 56, 67]. Physically, shifting the location of the infinitesimal sources into complex space results in beams, controlled by the imaginary parts of the origin, instead of cylindrical and spherical waves in real origin 2D and 3D geometries, respectively. The beam generated by the complex origin sources can mimic the superposition of the fields generated by multiple real origin sources, resulting in faster and simpler simulations by MMP especially when modeling axisymmetric and long objects.

Before starting with the implementation of the idea in layered media, it is important to analyze the complex origin infinitesimal sources in free space, in order to understand the physical meaning of the imaginary part of the origin. In free space, the fields generated by a point source are given by the Hankel functions in 2D (cylindrical waves) and complex exponentials divided by the radial distance in 3D (spherical wave) [59, 68], in real space. If the origin of the infinitesimal source is taken as a complex number, then the field generated can be concentrated in any direction by tuning the imaginary parts of the origin. Also the field does not fan out from a point but from a line in 2D and a circular disk in 3D. A visual explanation of the effect of the imaginary part in the origin can be seen in Fig. 2.9. As shown in the plots, the beam generated by the point sources is concentrated in the direction given by the vector $\overrightarrow{d} = -(\Im(x_o), \Im(y_o), \Im(z_o))$ with the initial point located at $(\Re(x_o), \Re(y_o), \Re(z_o))$, where (x_o, y_o, z_o) is the location of the origin[2]. Another observation is that the field fans out from the intersection of the plane that is normal to the vector $\overrightarrow{d}$ at $(\Re(x_o), \Re(y_o), \Re(z_o))$, and the cylinder (in 2D) or sphere (in 3D) centered at $(\Re(x_o), \Re(y_o), \Re(z_o))$ with the radius given by $r = \sqrt{\Im(x_o)^2 + \Im(y_o)^2 + \Im(z_o)^2}$ (for the discussion here, z_o is taken as 0 for the 2D case). These intersections generate a line and a circular disk in 2D and 3D, respectively, on which the field is discontinuous in the direction of $\overrightarrow{d}$, as shown in Fig.2.9. Another important observation is the singularity locations of the complex origin point sources in real space, since this is very important when using these expansions in numerical methods. For real origin point sources, the singularity is at the origin, i.e. at the location where the point source is located. The location of the singularity shifts when the origin is complex. In 2D, there are two singularities at the tips of the line from which the field is generated (i.e. at $s_1 = (\Im(y_o), -\Im(x_o))$ and $s_2 = (-\Im(y_o), \Im(x_o))$). In 3D, the singularity is on the circle through which

[2] When calculating the complex distance between the origin and the observation points $\Re\left(\sqrt{(x-x_o)^2 + (y-y_o)^2 + (z-z_o)^2}\right) > 0$ is used to decide on the branch.

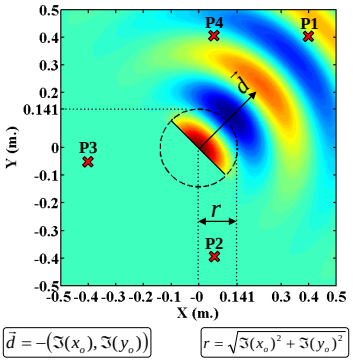

(a) 2D. Real part of the cylindrical wave at an instance of time. The origin of the point source is $O = (0 - j0.1, 0 - j0.1)$. The field fans out from a line that is normal to the vector d. The test points for the integrand behavior analysis (refer to Fig. 2.10) are marked with red crosses.

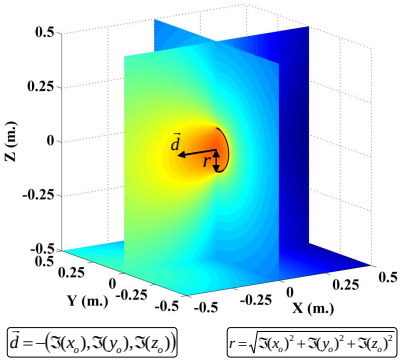

(b) 3D. Magnitude of spherical wave. The origin of the point source is $O = (0 + j0.1, 0, 0)$. The field fans out from a circular disk that is normal to the vector d.

Figure 2.9: The fields generated by complex origin point sources in free space, $\lambda_0 = 0.3m$.

the field is generated (i.e. intersection of the plane that is perpendicular to the vector $\vec{d}$ and the hollow sphere with radius r). That is simply because of the fact that the complex radial distance at these locations vanishes.

Above, the effect of imaginary values in the origin of infinitesimal sources is analyzed in spatial domain. In order to obtain the layered media Green's functions for complex origin sources, the spectral domain analysis should also be performed. For this purpose, the integrands defined at the test points in Fig. 2.9(a) (i.e. the integrands in (2.8)) are analyzed on the complex k_x plane. A comparison of the integrands on the complex k_x plane (the same comparison can be done in 3D on the complex k_ρ plane) reveals that the behavior of the integrands can be different in the different quadrants. This behavior is not seen in real origin case, since it is guaranteed by the correct choice of branch cuts that the integrands do not explode on the $\Re(k_x)$ axis or on the 3^{rd} and 4^{th} quadrants. On the other hand, a modification is needed in the definition of the SIP for complex origin infinitesimal sources, since the correct choice of branch cuts do not guarantee well behaving integrands on a given path, as shown in Fig. 2.10. Such a modification can be seen in Fig. 2.11 where 4 different path choices are introduced. Comparing the behavior of the integrands in Fig. 2.10

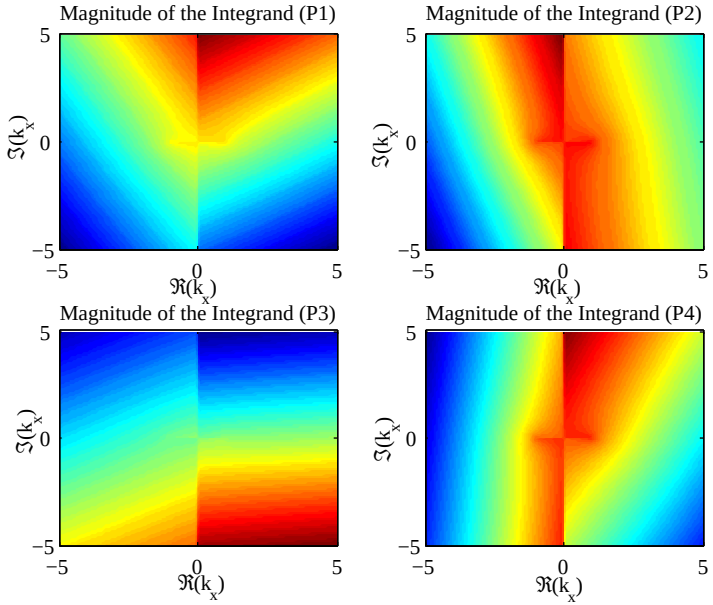

Figure 2.10: Surface: Free space spectral domain Green's function defined at the corresponding test points in Fig. 2.9(a), in logarithmic scale, arbitrary units.

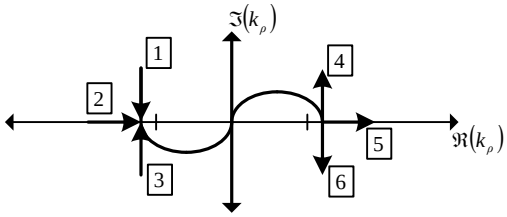

Figure 2.11: SIP modification for the complex origin infinitesimal sources and the possible choices for the tail integration paths.

on the different paths shown in Fig. 2.11 reveals that the field value at P1 should be calculated by paths 2 or 3 and 5 or 6, which are also the correct path choices for the real origin infinitesimal sources. Likewise for the field in P2, the paths 2 or 3 and 5 or 4, for the field in P3, the paths 1 or 2 and only 4 and finally for the field in P4, the paths 1 or 2 and 5 or 6 should be used. Comparing the

results of the analysis done here with the integrands in appendix $A.3$ reveals that the same technique should be applied to the different wave types that are used in the spectral domain layered media Green's functions, i.e. the up going ($e^{-jk_{zj}z}$ terms in appendix $A.3$) and down going waves ($e^{jk_{zj}z}$ terms in appendix $A.3$) separately. The reason for this separation is due to the fact that it is not guaranteed that the integrands of both up and down going waves will be numerically integrable on the same path. In other words, the integrand for the up going wave can decay fast enough on a given path, making it possible to integrate numerically, but on the same path the integrand for the down going wave can increase exponentially, which can dramatically increase the numerical cost for the integration if not make it impossible to obtain the results. Once such an analysis is performed by checking the behavior of the integrands and their derivatives along the given path, the numerical computation of the integrals can be performed in the same fashion as it is done for the real origin infinitesimal sources. As a result of the procedure described here, the time needed for the

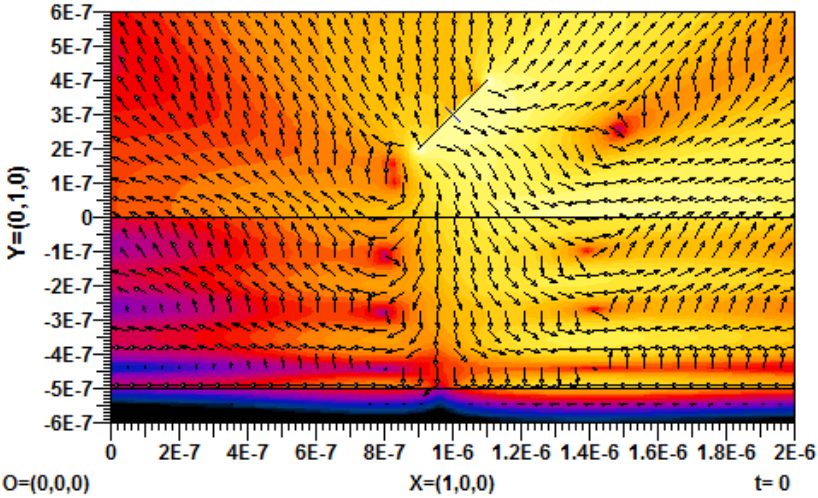

Figure 2.12: Surface: time averaged Poynting vector magnitude generated by a 2D magnetic line source (z-directed) located at $(1000 - j100, 300 + j100)$nm in logarithmic scale with $k_\gamma = 0$. Arrows: Direction of power flow. The field fans out from the black line similar to Fig. 2.9(a).

calculation of all the field components increase approximately by $\sim \times 1.5$ in 2D and $\sim \times 3$ in 3D. Despite this, complex origin expansions can reduce the total time for the simulation, provided that several real origin expansions can be

replaced by a single complex origin expansion, which is well suited especially for long structures compared to the wavelength as demonstrated in section 4.2 [51]. Two examples of the power generated by complex origin infinitesimal sources in the layered geometry in Fig. 2.4 can be seen in Fig. 2.12 and Fig. 2.13.

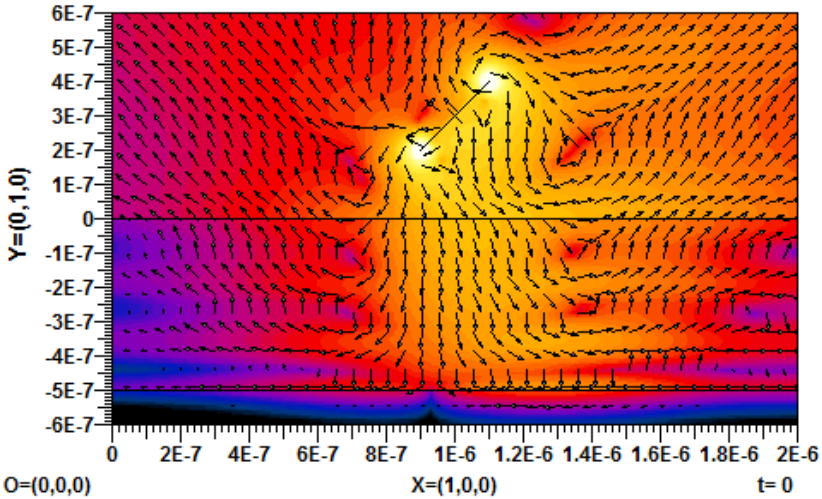

Figure 2.13: Surface: time averaged Poynting vector magnitude generated by a 3D electric point source (x-directed) located at $(1000-j100, 300+j100, 0)$nm in logarithmic scale on $z = 0$ plane. Arrows: direction of power flow. The cross section of the circle through which the field fans out on $z = 0$ plane is shown as the black line similar to Fig. 2.9(b).

2.6 A remark on time convention change

As noted previously, for the derivations in this chapter $e^{j\omega t}$ time convention is used. In the numerical results chapter however, $e^{-i\omega t}$ time convention is used. This difference is frequently seen in the numerical EM community (engineers use $e^{j\omega t}$ whereas mathematicians and physicists use $e^{-i\omega t}$ more often) and needs some attention in order to obtain the same results with both of the conventions. In a nutshell, the time convention change introduces a complex conjugation operator into the set of equations. Therefore one needs to take the complex conjugate of all the complex valued variables related to the calculation to change the time convention from one to the other. As an example, the positive x going solution of the wave equation in 1D free space is given by the plane wave e^{-jkx}

with $e^{j\omega t}$ time convention. The complex conjugate of the formula, i.e. e^{ikx} defines the same wave nature in $e^{-i\omega t}$ time convention. The same can be seen in the out going solutions of the wave equation in 2D and 3D, i.e. $H_0^{(2)}(k\rho)$ with $e^{j\omega t}$ vs. $H_0^{(1)}(k\rho)$ with $e^{-i\omega t}$ and $\frac{e^{-jkr}}{r}$ with $e^{j\omega t}$ vs. $\frac{e^{ikr}}{r}$ with $e^{-i\omega t}$. As stated above, in order to perform the time convention change, all the complex valued variables should be complex conjugated, including the constitutive parameters and the definitions of the branches of the wave vector components together with the SIP and the singularities. As an example, the permittivity value of silver at $\lambda_0 = 633nm$ is $\varepsilon_{r,Ag} = -18.10 - j0.48$ with $e^{j\omega t}$ and $\varepsilon_{r,Ag} = -18.10 + 0.48i$ with $e^{-i\omega t}$. Another important effect of the time convention change is observed in complex origin Green's functions. Following the same logic above, if the origin value is not complex conjugated when changing the time conventions, the beam direction changes, i.e. if $\overrightarrow{d}$ is the direction of the beam generated with $e^{j\omega t}$ as shown in Fig. 2.9, the direction of the beam generated by the infinitesimal source at the exact same location will point $-\overrightarrow{d}$ direction with $e^{-i\omega t}$. As a result, the Green's functions in of the time conventions can be used in the other time convention by simply taking the complex conjugates of the field data (and the origin point in the case of complex origin Green's functions).

A more detailed analysis of the time convention change can be performed by comparing the derivations of Chew [58] (with $e^{-i\omega t}$) and Aksun [59] (with $e^{j\omega t}$).

3 Method of Multiple Multipoles (MMP)

3.1 Introduction

The method of multiple multipoles (MMP) is a boundary discretization method developed by Ch. Hafner in 1980 [69] for the solution of Maxwell's equations in shielded or open numerical domains. The method can be seen as the extension of the Mie theory [6] applied to arbitrarily shaped structures combined with the general point matching technique [8, 70]. Up to date, several upgrades for MMP were introduced that made it possible to perform 2D and 3D electrostatic, magnetostatic and electrodynamic analyses [42, 51, 71, 72, 73, 74, 75, 76, 77, 78]. In 1990, a book-software package for MMP, later called MAX-1, was published [79] and updated frequently in the following years [80, 46]. In 2009, MAX-1 was replaced by the open-source simulation package OpenMaX that includes the latest version of MMP and other numerical methods and tools for electromagnetics [48]. In this thesis, OpenMaX[1] is updated by including layered media Green's functions in the MMP module. All the computations and results in this thesis are obtained by the updated version of OpenMaX, if not stated otherwise.

In the MMP analysis, fields are expanded as follows:

$$F_i = \sum_{n=1}^{N_i} A_n^i E_n^i + \mathbf{error} \tag{3.1}$$

where E_n^i are the fields generated by the expansions responsible for domain(s) i and A_n^i are the corresponding amplitudes to be determined in such a way that the error is minimized on the boundary between corresponding domains. The so called expansion fields, E_n^i in (3.1), can be any solution of the Maxwell's equations for the given single or multiple numerical domains, e.g. plane waves, cylindrical waves, spherical waves, higher order multipole fields, layered media Green's functions, superposition of the multiple expansions, etc [8][2].

As one can see, a major advantage of MMP is the freedom of choice in the expansions types, by which one can select a suited set of expansions depending on the geometrical specifications of the structures (especially for relatively simple geometries, e.g. spheroids, rods, axi-symmetrical structures, etc), resulting

[1] In OpenMaX $e^{-i\omega t}$ is used, as opposed to the derivations in chapter 2. The effect of time convention change is provided in section 2.6

[2] In the case of an expansion responsible for the fields in multiple domains, the field continuity relations should be fulfilled on the interfaces in the corresponding multiple domains, e.g as discussed in section 2.4.

in highly efficient results obtained by minimal computational effort. Another advantage of MMP is the ability of monitoring the error as in (3.1), by comparing the field values generated by the expansions and the analytical field values induced by the incident field at the so called matching points defined on the boundaries. Since this error measure is localized, the user can decide where to perform a refinement around the boundaries of the corresponding structures by placing more expansions and/or matching points. Because of these advantages, MMP is one of the most efficient numerical methods in EM. Several works use the results obtained by MMP as reference solution when comparing the accuracy of other numerical methods e.g. in [81, 82, 83, 84, 85, 86].

However, there are some difficulties in the implementation of MMP, especially for structures with complicated geometrical features. The first difficulty is choosing the correct type of expansions and placing them at the efficient locations in order to solve the problem. Automatic expansion distribution routines in OpenMaX (e.g. [8, 75, 76, 87]) usually work fine but in the case of structures with complicated geometries, the user experience on the type and the location of the expansions is desired [8, 46]. Another difficulty in the MMP analysis is the dense and ill-conditioned MMP matrices which has a big influence in the accuracy of the results. Since general point matching technique is used in MMP, the user can decide on the size of the matrix (the MMP matrix is not square but overdetermined in general, controlled by the number of expansions and matching points) and try to obtain a well behaving matrix, which needs experience on the expansion types and their effect in the condition number of the MMP matrix [8] as well. In addition, modeling layered geometries by the classical MMP approach (using only single domain expansions) is a difficult task, since the boundary conditions in the layered geometry should be fulfilled simultaneously with the boundary conditions in the structures placed in the layered geometry (e.g. as depicted in Fig. 3.1). As a result, in order to obtain accurate solutions, the number of the expansions and the matching points would be increased dramatically, giving rise to complicated MMP problems that are not easy to solve, if not impossible [76]. One of the goals of this thesis is to eliminate the difficulty of analyzing structures in layered geometries by introducing layered media Green's functions as an expansion set to MMP. Since the boundary conditions in the layered medium is analytically fulfilled by the definition of layered media Green's functions, the complexity of such problems are decreased dramatically [42, 51, 77] [3].

In this chapter, the basic features of MMP will be discussed for the scattering

[3] In [42], L. Novotny introduced the technique of using layered media Green's functions in the MMP analysis of 3D geometries. Here, this idea is used as a starting point and several updates are introduced in the layered media Green's functions (2D, modified 2D, 3D, complex origin layered media Green's functions as introduced in chapter 2) in order to perform the eigenvalue and scattering analyses of nano structures in a robust and efficient way.

and eigenvalue analyses of plasmonic structures. Since it is not possible to discuss all the aspects of MMP in this chapter, the interested readers can refer to [8], in which a detailed analysis of MMP is carried out together with the properties of the expansions that can be used.

3.2 The method and the MMP matrix structure

As described above, MMP is a boundary discretization method, i.e. only the boundaries of homogenous domains are discretized using a finite set of matching points. The boundary conditions (refer to (2.11)) in the matching points are used to obtain the amplitudes of the expansions in such a way that the mismatch error integral along the boundary is minimized. Then the fields in a given domain is obtained by the superposition of the fields generated by the corresponding expansions, as in (3.1). An illustration of the MMP analysis can be seen in Fig. 3.1.

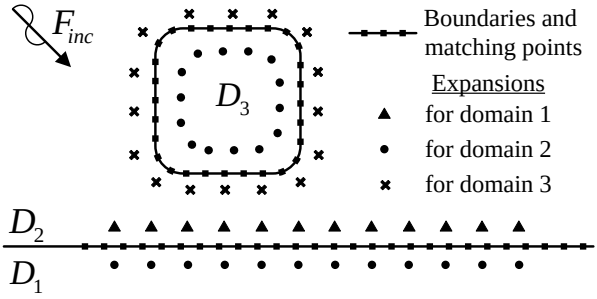

Figure 3.1: Illustration of the classical 2D MMP analysis of a scatterer placed in a 2 layered geometry. The different sets of 2D expansions are responsible for the fields in the different domains as shown. The exact same approach can be used in the 3D analysis by distributing 3D expansions along the boundaries.

Mathematically, fulfilling the boundary continuity conditions in the matching points requires the solution of a matrix equation of the kind:

$$\mathbf{M}\overrightarrow{p} = \overrightarrow{f} + \overrightarrow{\eta} \tag{3.2}$$

where the RHS vector $\overrightarrow{f}$ contains the normalized[4] field values at the matching points, obtained analytically by fulfilling the boundary conditions in presence of

[4] All the field components are normalized so that they are comparable in magnitude. The normalization is defined in the error measure (3.3) for each field component.

the incident field. The vector $\overrightarrow{p}$ contains the unknown complex amplitudes, the so called parameters of the expansions, to be determined by the MMP analysis. $\overrightarrow{\eta}$ is the error vector containing the normalized field mismatch errors defined at the matching points. The structure of the MMP matrix **M** is illustrated in Fig. 3.2.

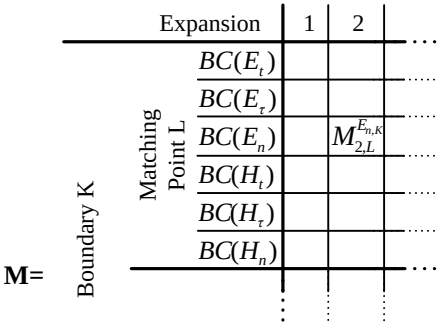

Figure 3.2: The MMP matrix structure. The subscripts τ and t are the two tangential components and n is the normal normal component of the corresponding field type. The rows contain the normalized[4] boundary conditions in the corresponding matching points and the columns contain the fields generated by the corresponding expansion sampled at the matching points. As an example, the matrix entry $M_{2,L}^{E_n,K}$ is the normalized[4] E field value, normal component with respect to boundary K, defined at matching point L, generated by expansion 2.

3.3 MMP analysis of layered media

As discussed above, the expansions used in the MMP analysis should be selected according to the geometrical and material specifications of the structures, and they should be solutions of Maxwell's equations in the corresponding domains. As an example, in the solution of plane wave propagation in a two layered geometry (same setting as in Fig. 3.1 without the scatterer D_3) two plane wave expansions with the propagation directions obtained by Snell's law are enough: one to model the reflected field in D_2 (e.g. only one of the •s in D_1 taken as plane wave expansion) and one to model the field transmitted to D_1 (e.g. only one of the ▲s in D_2 taken as plane wave expansion). In the presence of the scatterer for the same setting, it is clear that the plane wave expansions are not sufficient to model the fields in all the domains. Therefore monopole (and higher

order multipole) expansions distributed along the boundaries may be used as sketched in Fig. 3.1.

In the analysis of general layered media, the MMP analysis complexity increases significantly, since the number of expansions increases with the number of layers. In addition, a lateral truncation in the layered media is needed for the classical MMP approach, since infinitely many expansions are needed to fulfill the boundary conditions everywhere in the layered medium, which is obviously not possible. This problem corresponds to popular domain truncation techniques such as perfectly matched layers (PML) or absorbing boundary conditions (ABC) in domain discretization methods. A similar truncation technique can be used in MMP by introducing a fictitious boundary, on which the boundary conditions are fulfilled by two different sets of expansions responsible for the fields in the near and far field regions[5]. But as discussed in the beginning of the chapter, in order to use this technique in MMP, user experience is highly demanded and the complexity of the problem is increased dramatically with the number of layers which makes it harder to analyze. Another difficulty is observed when the layered media support guided waves, which makes the MMP analysis extremely difficult, if not impossible, since a discrete set of point sources may not be enough to capture the guided wave contributions for a general layered medium.[6]

In order to eliminate the problems listed above, the layered media Green's functions are introduced as a new expansion set (called layered expansions in the MMP analysis). For instance, in order to analyze the structure shown in Fig. 3.1, the •s in D_3 should be taken as layered expansions for a general analysis. As a result, the ▲s and the •s along $\partial D_{1,2}$ are removed, since the boundary conditions on $\partial D_{1,2}$ are automatically fulfilled by the definition of layered expansions. For such a setting, the incident field is obtained by the set of plane waves, without the scatterer, as described above in the solution of the plane wave propagation example. This is due to the fact that the plane wave propagation inside all the layers can not be approximated by a set of layered expansions localized inside a finite sized scatterer. As discussed here briefly, the correct choice of expansions plays a very important role on the performance of the MMP, which is analyzed in detail in [8].

[5] In [76], E. Moreno introduced a technique to analyze structures in layered media by MMP by dividing the whole problem into subproblems responsible for the near and far field regions by using single domain expansions. In such MMP problems, user experience is highly demanded in order to choose the correct type of single domain expansions and place them in the correct locations.

[6] The same effect is observed in the approximation of spectral domain Green's functions by a set of discrete complex images (DCIM) [54]. It is prone to inefficiencies and often impossible to approximate the singularities in the spectral domain Green's functions (corresponds to guided wave contributions in spatial domain) by a set of complex exponentials (correspond to fields generated by homogenous medium point sources in spatial domain) [56, 64].

3.4 MMP error: a measure of accuracy with respect to analytical solution

As mentioned at the beginning of the chapter, the main aim of MMP is to minimize the total boundary condition error in the matching points (approximating the integral of the boundary condition errors on the corresponding boundary) by the superposition of the fields generated by the given set of expansions. In order to do this, an error measure at a given matching point P on the boundary $\partial D_{i,j}$ for all the field components (subscripts n, t, τ denote the normal and the 2 tangential components of the corresponding field, with respect to the boundary $\partial D_{i,j}$ that are orthogonal to each other) is defined as follows [8]:

$$\eta_{ij}^2 = a_P \Bigg(w_{E_t}^2 (E_{ti} - E_{tj})^2 + w_{E_\tau}^2 (E_{\tau i} - E_{\tau j})^2 + w_{E_n}^2 \left(\frac{\varepsilon_i}{\varepsilon_{ij}} E_{ni} - \frac{\varepsilon_j}{\varepsilon_{ij}} E_{nj} \right)^2 \cdots$$
$$Z_{ij}^2 \left[w_{H_t}^2 (H_{ti} - H_{tj})^2 + w_{H_\tau}^2 (H_{\tau i} - H_{\tau j})^2 + w_{H_n}^2 \left(\frac{\mu_i}{\mu_{ij}} H_{ni} - \frac{\mu_j}{\mu_{ij}} H_{nj} \right)^2 \right] \Bigg) \tag{3.3}$$

where the constants used to normalize the field components (in order to include the mismatch errors of different field components equivalently in the error definition) are given as:

$$\begin{aligned} \varepsilon_{ij} &= \sqrt{\varepsilon_i \varepsilon_j} \\ \mu_{ij} &= \sqrt{\mu_i \mu_j} \\ Z_{ij} &= \sqrt{\mu_{ij} / \varepsilon_{ij}} \end{aligned} \tag{3.4}$$

The weights w_{F_χ} in (3.3) defined for the χ component of the F kind of field, are used to balance the error contributions and in general set to 1 for all the field types and components in the general scattering analysis. Additionally, the a_Ps are geometric weights defined for the matching point P. In the 3D analysis, the boundary is divided into patches with the area of a_P and the corresponding matching point P is placed at the center of the patch. In the 2D analysis a_P becomes the average distance of the matching point P from its two neighbors.

After introducing the definition of the error measure to be minimized, the normalization procedure for the different field components is clear. As an example, using the definition in (3.3), the entry in Fig. 3.2 is given by:

$$M_{2,L}^{E_{n,K}} = w_{E_n} \sqrt{a_L} (\varepsilon_i / \varepsilon_{ij}) E_{ni}^0(P) \tag{3.5}$$

where subscripts i and j denote the neighboring boundaries to the matching point L. Obviously, the same normalization should also be applied to the corresponding entries of the RHS vector $\overrightarrow{f}$ in (3.2). In this example (i.e. the MMP

matrix in Fig. 3.2), the fields generated by expansion 2 are used to build up the fields in D_i and $E^0_{ni}(P)$ denotes the normal component of the E field at the matching point P generated by expansion 2 (e.g. obtained by (A.3) or (A.2)). Once the matrix $\mathbf{M}$ and the RHS vector $\overrightarrow{f}$ are obtained, the equation (3.2) is solved in the least square sense, since the linear system is overdetermined in the general MMP analysis (typically about twice or three times as many equations as unknowns are used). After solving the linear system, the mismatch error can be monitored in all the matching points contained in the error vector $\overrightarrow{\eta}$ in (3.1) with the entries in (3.3). In the MMP analysis, several error measures derived from the vector $\overrightarrow{\eta}$ are used to check the accuracy of results, including the maximum and average field errors in the relative and absolute scales.

In the following, a step by step MMP scattering analysis of a plasmonic structure placed in a layered geometry is introduced.

3.5 Example: 2D Scattering analysis by MMP - a triangular particle in a three layered medium with plane wave incidence

An scattering analysis example by MMP is shown in Fig. 3.3, where the definition of the incident field and the geometry specifications are provided. As

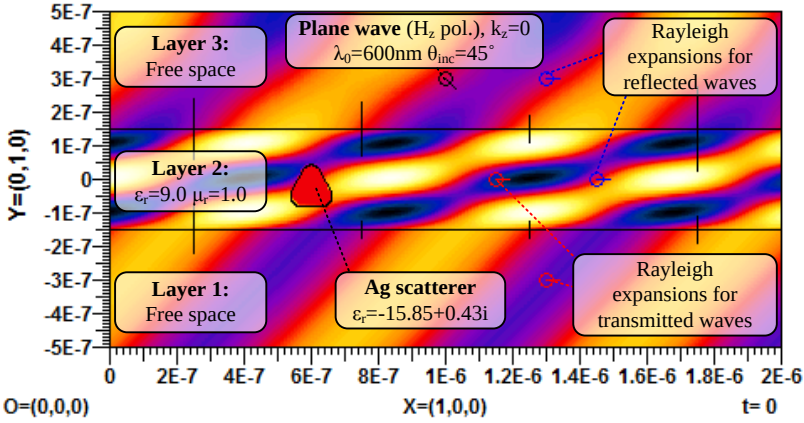

Figure 3.3: Scattering analysis: Step 1) Propagation of a H_z polarized plane wave in the layered geometry. Surface: H-field z-component at an instance of time. This field data is used as the incident field for the whole scattering problem with the solution shown in Fig. 3.4. The normal lines on the boundaries of the layers correspond to relative errors at the matching points (max. rel. err. $=1.11 \times 10^{-13}$%).

discussed at the beginning of this chapter, when the incident field is a plane wave, first, the propagation profile of the plane wave in all the layers without the Ag [66] scatterer should be obtained in order to be used as the incident

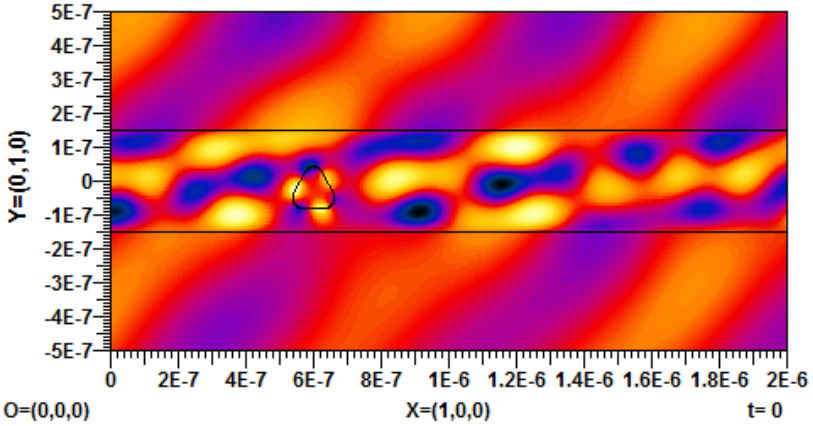

Figure 3.4: Scattering analysis: Step 2) The solution of the whole scattering problem, with the incident field definition in Fig. 3.3. Surface: H-field z-component of the total field at an instance of time. The expansions used in this solution can be seen in Fig. 3.5.

field for the whole scattering problem[7]. For this purpose, 1 H_z[8] polarized plane wave expansion and 4 0^{th} order Rayleigh expansions with the same polarization responsible for different wave types are distributed as shown in Fig. 3.3. The Rayleigh expansions are very similar to plane wave expansions. They use the continuity of the parallel wave vector component in the layered medium and determine the propagation direction for the corresponding plane waves automatically. As a result, the necessity of calculating the directions manually by Snell's law is eliminated. In Fig. 3.3, the black expansion is the incident field for this subproblem generating a plane wave at $\lambda_0 = 600nm$ with H_z polarization in layer 3, propagating in the direction of the vector $(1, -1)$, i.e. with 45° angle of incidence. The remaining expansions are responsible for the reflected (blue expansions) and transmitted (red expansions) plane waves in the domains in which they are placed. It should be noted that, since there are no singularities in a plane wave definition (e.g. $e^{\pm iky}$), the expansions can be placed inside their

[7] This can be done analytically or with a simplified MMP model that provides highly accurate results with small MMP matrices (for this problem, there are only 4 unknowns) as described here.

[8] H_z polarization corresponds to TM polarization in the Green's function discussion in this thesis, e.g. in appendix A

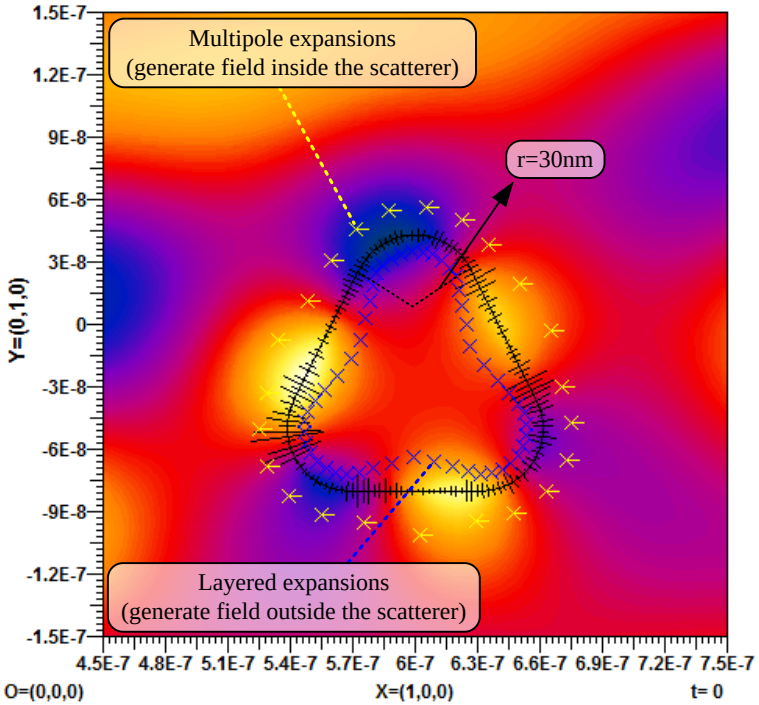

Figure 3.5: Scattering analysis: The whole problem is solved by the expansions distributed near the boundary of the scatterer. The normal lines on the boundary corresponds to relative errors at the matching points (max. rel. err. $=3.48 \times 10^{-1}\%$).

responsible domains, which is not possible for singular expansions (as shown in Fig. 3.5). Once the expansions are distributed, the problem is solved by using the field continuity relations defined in 4 matching points for each boundary. The boundary of the Ag scatterer is not discretized, since it has no effect on the plane wave propagation for this sub problem. The perpendicular lines on the boundaries between different layers show the relative error at the corresponding matching point, the longest corresponding to the maximum relative error of $1.11 \times 10^{-13}\%$ with the average error of $5.59 \times 10^{-14}\%$, therefore accuracy of the solution is limited by the numerical precision (double) used by OpenMaX.

In the second part of the problem, the solution obtained in the first part (Fig. 3.3) is used as the incident field for the problem including the Ag scatterer

by a *connection*[9], that is responsible for transferring the solution from the first part to the second. The solution and the expansions used for this final part can be seen Figs. 3.4 and 3.5, respectively. As can be seen in Fig. 3.5, a discretization performed only on the boundary of the scatterer is enough for the solution (150 matching points are used). For the fields outside and inside the scatterer, 53 layered expansions and 24 multipoles with the highest order 4 are used, respectively. The infinite boundaries between the layers must not be discretized at all, because the *connection* and the layered expansions fulfill the boundary conditions on those boundaries. For this example, only H_z polarized expansions are used since the incident field is H_z polarized. For an arbitrarily polarized incident wave ($k_z \neq 0$), both the E_z and H_z polarized expansions should be used with the same k_z value of the incident field. As before, the perpendicular lines on the boundary of the scatterer show the relative error at the corresponding matching point, the longest corresponding to $3.48 \times 10^{-1}\%$ with the average error of $7.01 \times 10^{-2}\%$. In general, the results with these error measures can be used in the scattering analysis, since $\sim 3-4$ significant digits in the field values are enough to obtain a useful result, since the mismatch error usually decays away from the boundaries. In addition, the measured material parameters for metals usually differ strongly in literature and effect the results dramatically (e.g. [66] vs. [88]). Yet, if a better accuracy is needed, the number of expansions and matching points should be increased by the local error data $\overrightarrow{\eta}$. It should be also noted that the same analysis can be done in 3D exactly the same way demonstrated here. The only difference is the expansion types and locations, which should be updated for a 3D setting. Such an example is presented in chapter 4, where the scattering cross section of a plamonic particle placed on a multilayered geometry is analyzed.

3.6 Eigenvalue analysis of plasmonic waveguides by MMP

Physically, the numerical eigenvalue analysis of waveguides[10] is the method for obtaining the complex propagation constant in the longitudinal direction, at which the power flux along the waveguide is maximized[11] for a given frequency [8, 89]. With this engineering approach, the imaginary part of the eigenvalue corresponds to material losses (when the signal propagates along the waveguide, it will decay with the rate defined by the imaginary part of

[9] Connections are fixed superposition of fields generated by given sets of expansions. They can be also used as an expansion set in the MMP solution.

[10] The waveguides analyzed in this thesis are assumed to be uniform in the propagation (longitudinal) direction and have an arbitrary cross section in the transverse plane, which makes it possible to use the 2D expansions with nonzero k_γ values given by (A.2) and (A.18).

[11] In the discussion here, k_γ denotes the propagation constant in longitudinal direction and $k_{\gamma,e}$ denotes an eigenvalue of the structure analyzed.

the eigenvalue: $e^{ik_{\gamma,e}z} = e^{i\Re(k_{\gamma,e})z}e^{-\Im(k_{\gamma,e})z}$ with $\Im(k_{\gamma,e}) > 0$ and $e^{-i\omega t}$ for passive materials). Another type of eigenvalue analysis, used frequently by the physicists, could be performed by determining a complex eigenfrequency for a given k_γ value. In that case the imaginary part of the complex eigenvalue becomes responsible for the material losses (as time passes, the signal will decay with the rate defined by the imaginary part of the eigenfrequency: $e^{-i\omega_{\gamma,e}t} = e^{-i\Re(\omega_{\gamma,e})t}e^{\Im(\omega_{\gamma,e})t}$ with $\Im(\omega_{\gamma,e}) < 0$ for passive materials). This is not discussed in this thesis, but the technique described in this section could also be used to perform such an analysis, simply by interchanging the input and output variables, k_γ and the frequency ω_γ.

The eigenvalue analysis of arbitrary waveguides with dispersive and lossy materials (e.g. metals at optical spectrum) is one of the most demanding and difficult subjects in computational EM. The difficulty originates from the necessity of having a sufficiently good initial guess for the calculation of the exact location of the propagation constant $k_{\gamma,e}$. In general, the eigenvalue can be any point in the first quadrant of the complex k_γ plane for passive waveguides with $e^{-i\omega t}$ time convention (fourth quadrant with $e^{j\omega t}$). In the eigenvalue analysis by MMP, the possible locations of the eigenvalues on a given complex k_γ plane are calculated in an intermediate step, which provides a very useful information when finding the exact locations of eigenvalues, not only by MMP but also by other numerical methods.

In the classical eigenvalue analysis, the homogenous Maxwell's equations are solved analytically (by nonzero solutions) for the boundary conditions given by the geometry analyzed. Performing this mathematically requires the solution of the following homogenous matrix equation:

$$\mathbf{M}(k_{\gamma,e})\overrightarrow{X}(k_{\gamma,e}) = 0 \tag{3.6}$$

where $\mathbf{M}$ is the square system matrix of the geometry analyzed and $\overrightarrow{X}$ is the eigenvector, both evaluated at the eigenvalue $k_{\gamma,e}$. In order to find the eigenvalues of $\mathbf{M}$, the following well known condition is used[12]:

$$\det[\mathbf{M}(k_{\gamma,e})] = 0 \tag{3.7}$$

In general, finding the eigenvalues of the system matrix $\mathbf{M}$ require the solution of the transcendental equation of (3.7) using iterative root finding routines, e.g. bisection, regula-falsi, etc [8, 90]. However, in practice, this method is not used due to the difficulties in the numerical solution of the corresponding transcendental equations, especially for waveguides with complicated geometrical

[12] In the case of a non-square system matrix $\mathbf{M}$ (as in overdetermined MMP matrices), the same approach described here can be applied to the symmetric square matrix $\mathbf{M}^*\mathbf{M}$, where $\mathbf{M}^*$ is the adjoint of $\mathbf{M}$. In practice this is not recommended, because multiplying $\mathbf{M}$ by $\mathbf{M}^*$ squares the condition number,that introduces noise especially around the zeroes of $\det[\mathbf{M}(k_\gamma)^*\mathbf{M}(k_\gamma)]$ [83]

features. Instead, several numerical methods can be used to perform the eigenvalue analysis of arbitrarily shaped waveguides numerically, such as MMP [91], FEM [92], method of auxiliary sources (MAS) [7], finite difference time domain (FDTD) [93], etc.

As opposed to FEM, in the eigenvalue analysis by MMP, it is not possible to extract eigenvalues directly from the MMP matrix, since it is rectangular in general. Therefore, the zero determinant condition in (3.7) is not used in the MMP analysis. Instead, the homogenous Helmholtz equation for the given geometry is solved by a set of expansions for different k_γ values. Then the response of the structure is monitored and a search function is defined as follows:

$$f(k_\gamma) = \frac{Error(k_\gamma)}{Amplitude(k_\gamma)} \tag{3.8}$$

where $Error(k_\gamma)$ is the MMP mismatch error on the waveguide and $Amplitude(k_\gamma)$ is the response of the system. In (3.8), it is possible to introduce several definitions for $Error(k_\gamma)$ (e.g. absolute/relative errors integrated or the averaged/-maximum error on the waveguide) and $Amplitude(k_\gamma)$ (e.g. sum of field values at given points, integral of the average Poynting vector on an area where strong fields are expected, etc.). The different MMP search functions can be more useful for different problem types and they can be used to check the the efficiency of the results[13]. Once the search function data is obtained for a given geometry, the eigenvalues are seen as minima locations of the search function. As a result, the eigenvalue problem is solved both in a mathematical (the MMP error is minimized) and physical (the response of the system maximized) sense[14].

It should be noted that MMP can work both with and without a fictitious source. When there is no fictitious source defined, the last expansion's[15] amplitude is set to 1 and the homogenous Maxwell's equations (i.e. (3.2) with $\overrightarrow{f} = \mathbf{0}$) are solved numerically by MMP and the technique described above is applied. Once the search function data is obtained on a given k_γ plane, a fine search is applied around the minima locations of the search function in order to obtain the exact location of the eigenvalue. In the analysis, tracing algorithms

[13] A routine is available in OpenMaX [48] that checks various error definitions to validate the eigenvalue.

[14] MMP eigenvalue analysis can be seen as a generalization of MAS and FDTD analyses. In MAS and FDTD, a fictitious source that "should" excite all the modes is used to feed the structure and the response of the system (usually magnitude of a chosen field type) is obtained in a given sensor point as a function of k_γ. As a result, peaks of the response reveals the eigenvalues and the problem is solved in a physical sense (the search function in (3.8) with $Error(k_\gamma) = 1$ corresponds to the search function used by MAS and FDTD). In these methods there is always a chance of not exciting (by the fictitious source) or detecting (by the sensor point) all the modes, which effects the efficiency of the methods dramatically [83].

[15] The last expansion can be selective and may be used to analyze specific modes [8] seperately.

can be applied in order to obtain the behavior of the eigenvalues e.g. as a function of wavelength by estimating the approximate locations of the eigenvalues of the next wavelength by the locations already determined [48]. As one can see, the search function data is very useful, since it provides the crucial information about the approximate locations and the number of eigenvalues in the region defined by the given k_γ plane [78, 83, 90] which is the main difficulty of eigenvalue analysis in all the well known numerical methods. In the following, a step by step eigenvalue analysis of a single wire plasmonic waveguide in layered media, performed by MMP (OpenMaX [48] is used) is included.

3.7 Example: Eigenvalue analysis by MMP - a metallic wire waveguide in a three layered medium

As an example, a plasmonic waveguide structure as shown in Fig. 3.6 is analyzed [78]. In the analysis, a symmetry plane is used and the odd (by taking the symmetry plane as a perfect magnetic conductor (PMC)) and the even (by taking the symmetry plane as a perfect electrical conductor (PEC)) cases are

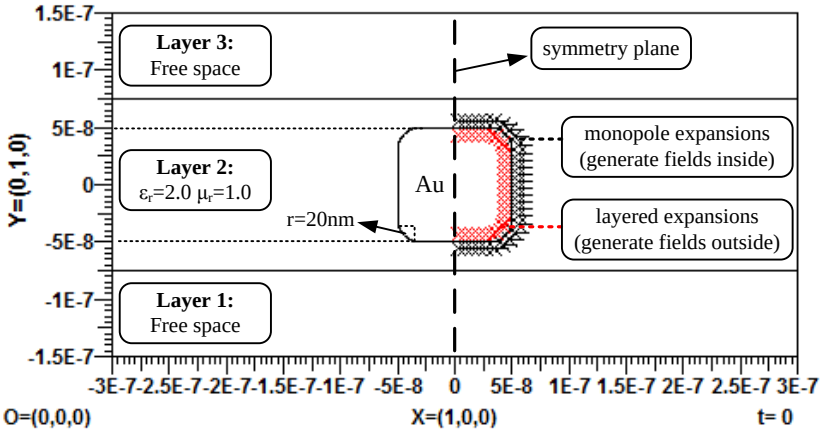

Figure 3.6: Eigenvalue analysis: Plasmonic waveguide geometry and the expansions used for the analysis. Symmetry plane is taken as PMC and PEC in order to analyze the so called odd and even cases, respectively.

analyzed separately. By using the symmetry plane, the numerical domain becomes smaller (only the right hand side of the symmetry plane in Fig. 3.6 is analyzed), therefore the results are obtained faster. In addition, the correspond-

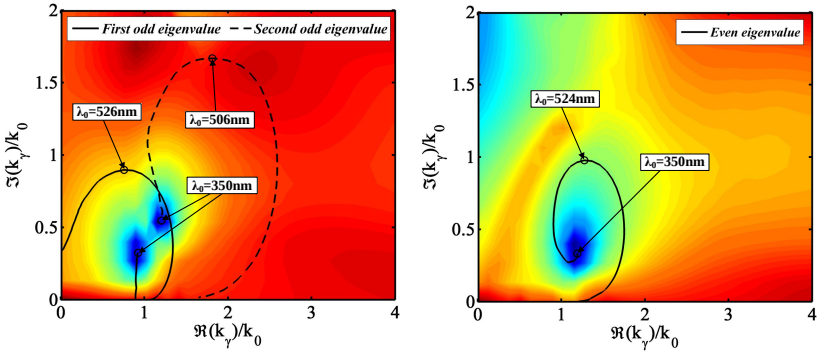

(a) Odd symmetric (symmetry plane in Fig. 3.6 is PMC) case.

(b) Even symmetric (symmetry plane in Fig. 3.6 is PEC) case.

Figure 3.7: Surface: The MMP search function (Av. Rel. Error / integral of Poynting vector in longitudinal direction around the wire) for the geometry shown in Fig. 3.6 on the given complex k_γ plane at $\lambda_0 = 350nm$. Dark blue regions are the minima of the search function, i.e. the locations of the eigenvalues. Lines: The loci of the eigenvalues as a function of free space wavelength. Circles on the lines show the locations of the eigenvalues at selected wavelengths.

ing eigenvalues are separated into two different problems, therefore finding the exact locations of the eigenvalues becomes easier, as demonstrated below. For the solution of this problem, 30 layered and 30 monopole expansions with both polarizations are used, for the fields outside and inside the Au [88] wire, respectively. The MMP search functions at $\lambda_0 = 350nm$ are plotted in Fig. 3.7. In the search function for this example the average relative error is used as $Error(k_\gamma)$ and the integral of the time averaged Poynting vector in longitudinal direction evaluated on a rectangular surface around the Au wire (shifted $20nm$ from the surface of the wire) is used as $Amplitude(k_\gamma)$. By performing a fine search around the locations of the minima (shown as dark blue locations in Fig. 3.7), the exact locations of the eigenvalues are found at $k_{\gamma,11} = (0.93 + 0.32i)k_0$ and $k_{\gamma,12} = (1.21 + 0.55i)k_0$ for the odd and $k_{\gamma,21} = (1.19 + 0.33i)k_0$ for the even symmetry at $\lambda_0 = 350$nm, with $k_0 = 2\pi/\lambda_0$. Once these values are obtained, the free space wavelength dependent behavior of the eigenvalues (lines in Fig. 3.7) are determined by the tracing algorithm included in OpenMaX, which uses a general parameter estimation technique [8, 48]. The eigenfields at $\lambda_0 = 350$nm are plotted in Fig. 3.8.

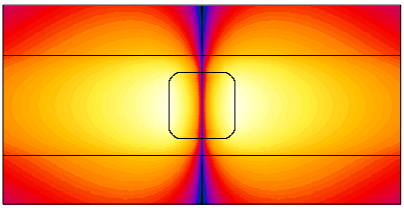

(a) First odd eigenfield at $k_{\gamma,11} = (0.93 + 0.32i)k_0$.

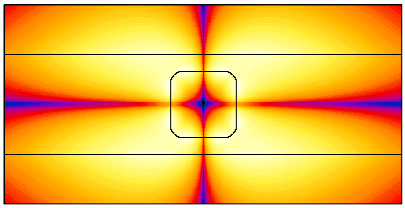

(b) Second odd eigenfield at $k_{\gamma,12} = (1.21 + 0.55i)k_0$.

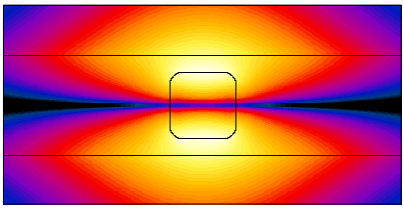

(c) Even eigenfield at $k_{\gamma,21} = (1.19 + 0.33i)k_0$.

Figure 3.8: Surface: The eigenfields of the example in Fig. 3.6 at the corresponding eigenvalues. Magnitude of H-field, z-component in the logarithmic scale, at $\lambda_0 = 350nm$, plotted on the same window as in Fig. 3.6.

As discussed at the beginning of this section, it is crucial to have a good initial guess for the eigenvalue search, not only for MMP but for all the well known numerical methods. Usually, it is not possible to make a guess about the locations of the eigenvalues, especially for lossy, dispersive and radiating waveguides (e.g. the example analyzed above). In addition to the relation between the material parameters and wavelength, the geometrical properties of the waveguides play a very important role on the eigenvalues, which makes it even harder to predict the locations of the eigenvalues. If "a not good enough" initial guess is given to a numerical method, it is highly possible to end up with arbitrary number of non-physical modes. As an example, the same geometry is analyzed with commercial FEM softwares Comsol Multiphysics 4.3a [94] and JCM Suite 2.6.3 [95] and the results are provided in Figs. 3.9 and 3.10, respectively. Experimentally, with the given settings of the softwares in the captions of the results, a good initial guess for $k_{\gamma,21}$ at $\lambda_0 = 350nm$ corresponds to a value that is inside a circle with the radius of $0.1 \sim 0.2k_0$ where $k_{\gamma,21}$ is located at the center. For low-loss modes (i.e. low radiation loss: $(\Re(k_{\gamma,e}) > k_{med})$ and low material loss:

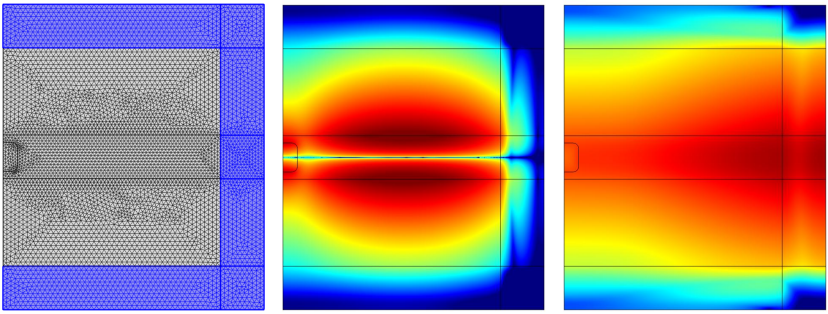

(a) Mesh generated by Comsol. Blue regions are PMLs with default settings.

(b) A wrong result (at $(1.23 - j0.01)k_0$) with initial guess of $1.44k_0$.

(c) A wrong result (at $(1.19 - j0.04)k_0$) with the initial guess of $(1.2 - j0.1)k_0$.

Figure 3.9: Comsol mesh used in all the calculations shown here (with the mesh size $\Delta h < \lambda_{med}/20$ and 3^{rd} order discretization) and the results[16] obtained for the given initial guess values in the captions. Magnitude of H-field, z-component in the logarithmic scale is plotted. The boundary on left is set to be PEC, corresponding to the even symmetry in OpenMaX. The correct value of $(1.19 - j0.33)k_0$ is obtained when the initial guess is set to be e.g. $(1.2 - j0.2)k_0$, which has the same eigenfield profile in Fig. 3.8(c).

(small $\Im(k_{\gamma,e})$, e.g $\leqslant 0.01k_{med}$)), a real initial guess slightly greater than the real part of the wave number of the ambient medium works fine. As a result of these observations, one can conclude that slight inefficiencies in the PML definitions give rise to inefficiencies in the eigenvalue analysis as well[17] and a "very good initial guess" is needed, even for this simple waveguide geometry. This general numerical difficulty can be solved by the MMP search function data, which is obtained in an intermediate step of the eigenvalue analysis by MMP as discussed and demonstrated above. By the search function, the approximate locations and the exact number of physical eigenvalues are obtained, which provides a very important guideline for the eigenvalue analysis, not only by MMP but also for other numerical methods. Several numerical examples are provided in chapter 4 in order to compare the loci of eigenvalues as a function of material and geometry properties.

[17] When $\Re(k_\gamma) < k_{med}$, the in-transverse-plane propagation of waves becomes stronger, and the performance of the PMLs becomes highly important. In the case of a bad initial guess, the method tries to resonate the whole numerical domain including the PML, which is of course non physical.

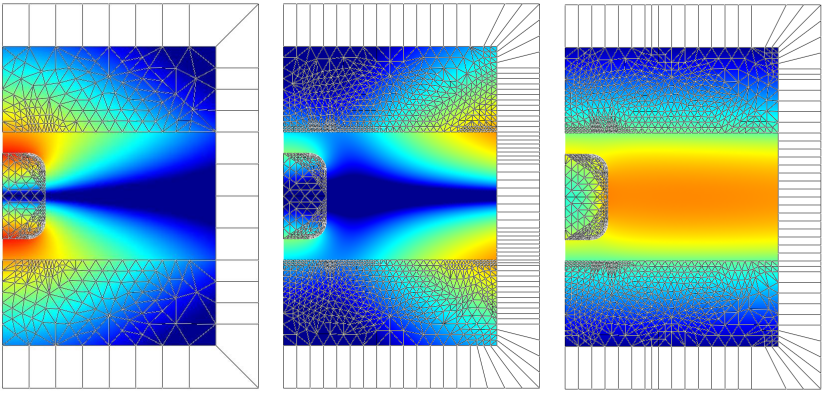

(a) The correct result (at $(1.19 + 0.33i)k_0$) with initial guess of $(1.2 + 0.2i)k_0$.

(b) A wrong result (at $(1.27 - 0.01i)k_0$) with initial guess of $1.44k_0$.

(c) A wrong result (at $(1.19 + 0.01i)k_0$) with the initial guess of $(1.2 + 0.1i)k_0$.

Figure 3.10: Results of the JCM Suite analysis of the example in Fig. 3.6 with the corresponding mesh settings (the mesh in dielectric slab is not included in the plot to see the field pattern clearer). Magnitude of H-field, z-component in the logarithmic scale is plotted. In this analysis, an adaptive mesh size refinement (h-refinement) is used (max. refinement iter. = 4 with tolerance = 10^{-4}) with 3^{rd} order discretization. A $50nm$ thick PML (white domains with quadrilateral elements) is used to truncate the domain and the boundary on left is set to be PEC, corresponding to the even symmetry in OpenMaX.

4 Numerical Results

In this chapter several numerical results and analyses are presented in order to demonstrate the robustness and efficiency of MMP updated by the layered media Green's functions. In the examples presented here, the metallic structures are taken to be Au and Ag, which are dispersive and lossy materials in the optics spectrum. The dispersive permittivity values of these materials can be obtained from a number of sources in the literature and here, the two mostly used measured permittivity values are used from Palik [88] (Au values for the eigenvalue analysis) and Johnson et.al [66] (Au values for the scattering cross section and Ag values for the scattering cross section and eigenvalue analyses). The real and imaginary parts of the permittivity values used in this work as a function of free space wavelength can be seen Fig. 4.1.

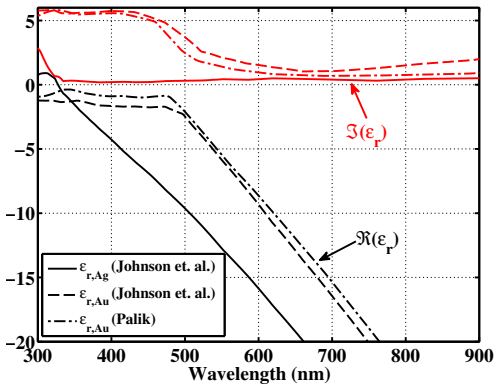

Figure 4.1: Measured permittivity values of Ag [66] and Au [66, 88] from popular sources used in literature and in this thesis.

As can be seen in Fig. 4.1, the permittivity values of Au have higher imaginary parts than the permittivity values of Ag. By this fact, one can conclude that the electrical material losses in Au is higher than Ag in optics regime. In the following examples, the effect of different material properties on the results is analyzed in numerous scattering and eigenvalue problems. All the materials used in the analyses here are nonmagnetic, i.e. $\mu_r = 1$ for all the materials.

4.1 2D Scattering analysis: comparison by the commercial FEM software COMSOL Multiphysics

For this example, a cylindrical Ag [66] scatterer placed in a five layered geometry is analyzed in presence of a plane wave illumination. The geometrical parameters and the definition of the incident plane wave are shown in Fig. 4.2. This problem is solved both by MMP (OpenMaX v.2013A [48]) and the commercial FEM software Comsol Multiphysics versions 4.2a and 4.3a [94] and the results are analyzed below.

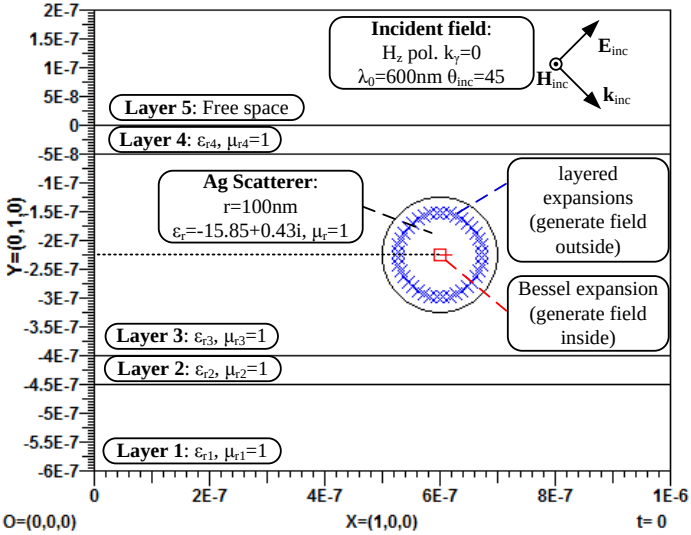

Figure 4.2: Geometry and H_z polarized incident plane wave for the scattering analysis. The expansion types and corresponding locations are plotted. 150 matching points (distributed linearly on the Ag scatterer) are used to solve the problem.

The reference MMP solutions are obtained by using 40 layered expansions (for the fields outside the scatterer, distributed linearly inside the scatterer) and 1 Bessel expansion[1] with the maximum order of 40 (for the field inside, placed at the center of the scatterer) as shown in Fig. 4.2. The analytical mismatch error at 150 matching points with the given number of expansions is less than 1×10^{-2}%, for all the different material parameters analyzed (the MMP

[1] The Bessel expansion is not singular (superposition of Bessel functions: $J_n(x)$), therefore it can be placed in its responsible domain.

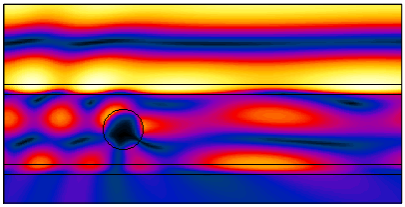

(a) $\varepsilon_{r1} = 1$, $\varepsilon_{r2} = 9.0$, $\varepsilon_{r3} = 2.25$, $\varepsilon_{r4} = 9.0$.

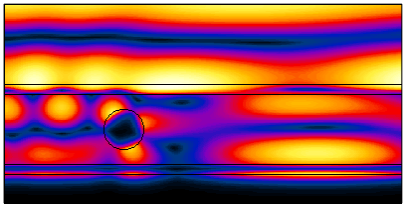

(b) $\varepsilon_{r1} = -15.85 + 0.43i$ (Ag), $\varepsilon_{r2} = 9.0$, $\varepsilon_{r3} = 2.25$, $\varepsilon_{r4} = 9.0$.

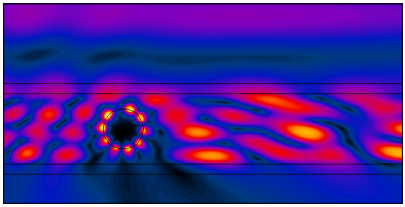

(c) $\varepsilon_{r1} = 1$, $\varepsilon_{r2} = 2.25$, $\varepsilon_{r3} = 9.0$, $\varepsilon_{r4} = 2.25$.

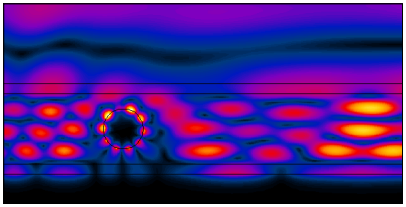

(d) $\varepsilon_{r1} = -15.85 + 0.43i$ (Ag), $\varepsilon_{r2} = 2.25$, $\varepsilon_{r3} = 9.0$, $\varepsilon_{r4} = 2.25$.

Figure 4.3: MMP results of the scattering problem shown in Fig. 4.2, with the material parameters provided in the captions. Surface: Total field. Magnitude of H-field, z-component, at $\lambda_0 = 600$nm, plotted on the window with $0 < x < 2\mu$m and -0.6μm$< y < 0.4\mu$m. with respect to Fig. 4.2.

error distributions on the scatterer are included in Figs. 4.6 and 4.8, where the error distributions of the solutions from different software are analyzed). The results are obtained by using the same technique discussed in example 3.5. The total field patterns can be seen in Fig. 4.3, where the corresponding material properties of the layers are provided in the captions.

As a comparison, the same scattering problems are solved by Comsol Multiphysics Ver.4.2*a* and Ver.4.3*a* [94] by using the discretization rule given in Fig. 4.4. In this analysis, the same technique used for the MMP solutions is applied for the solutions by FEM, i.e.: 1) the plane wave propagation problem in the layered media, without the scatterer, is solved by using periodic boundary conditions (fulfilling the continuity of the parallel wave vector component in all the layers, as in Rayleigh expansions of MMP) and 2) the whole scattering problem is then solved by using the solution of the first step as the incident field. It should be noted that the PMLs are used only in the second step of the analysis in order to truncate the layered medium.

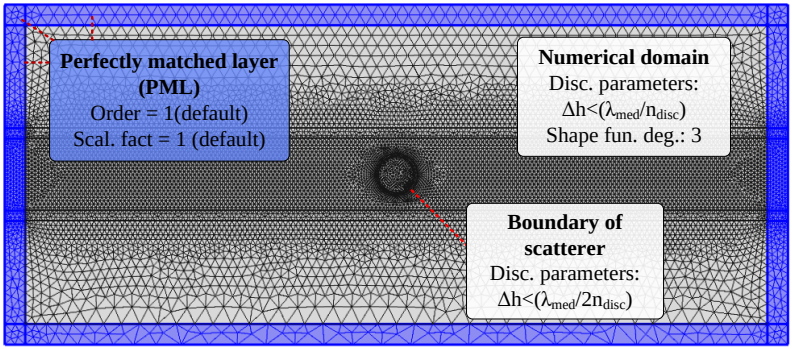

Figure 4.4: The mesh generated by Comsol Multiphysics for the geometry shown in Fig. 4.2 at $\lambda_0 = 600$nm with $n_{disc} = 10$. The maximum shape function degree of 3 and default values of PML settings are used. The mesh in this figure is the one created for the geometry with $\varepsilon_{r1} = -15.85 + 0.43i$ (Ag), $\varepsilon_{r2} = 2.25$, $\varepsilon_{r3} = 9.0$, $\varepsilon_{r4} = 2.25$.

The results obtained by OpenMaX 2013A and the two different versions of Comsol Multiphysics are compared at different locations of the numerical domain. In Fig. 4.5, the magnitude of the total magnetic field is compared on the Ag scatterer and in Fig. 4.7, the same comparison is done on the boundary between layers 1 and 2. Additionally, the errors in the solutions shown in the figures are compared in Figs. 4.6 and 4.8. The magenta lines in these plots are the relative MMP mismatch error evaluated at 150 points on the scatterer in Fig. 4.6 and at 500 points on the boundary between layers 1 and 2 in Fig. 4.8. All the other lines in the plots are the errors in the Comsol Multiphysics solutions[2].

Analyzing Figs. 4.5- 4.8 reveals that the results obtained by Comsol Multiphysics 4.3a are in good agreement with the MMP solutions. Additionally, the corresponding errors decrease when a finer mesh is used, as expected. However, the results obtained by Comsol Multiphysics 4.2a have significant errors that do not decrease with a finer mesh. As an example, in Fig. 4.7(b), the field shows an abrupt behavior on the boundary between dielectric and metallic materials, where an SPP resonance is observed. A similar result is also seen in Fig. 4.7(d) where the results from Comsol Multiphysics 4.2a are not in agreement with the

[2]For the Comsol Multiphysics calculations, the field is sampled on the scatterer by using the "extra fine" option in the result export settings which makes it possible to obtain results at sufficiently many sample points. The MMP results evaluated at the sample points are used to obtain the point-wise error plots as seen in Figs. 4.6 and 4.8.

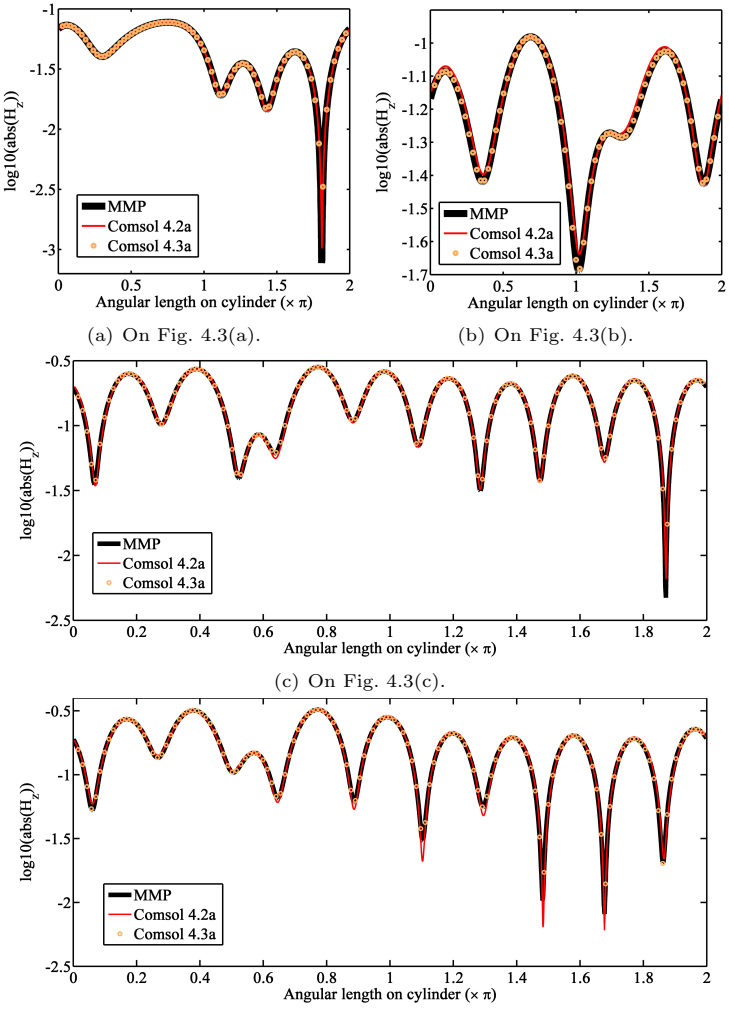

(a) On Fig. 4.3(a).

(b) On Fig. 4.3(b).

(c) On Fig. 4.3(c).

(d) On Fig. 4.3(d).

Figure 4.5: Comparison of MMP and Comsol results ($n_{disc} = 10$) on the cylindrical boundary, in logarithmic scale. The plotting parameter, "angular length" at 0 corresponds to $(700, -225)$nm in Fig. 4.2 and it increases in the anticlockwise direction.

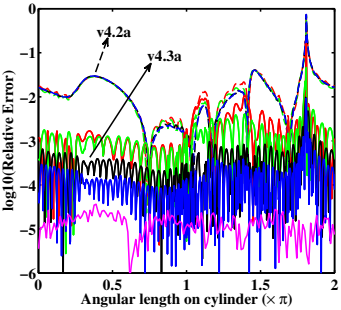

(a) Error in Fig. 4.5(a).

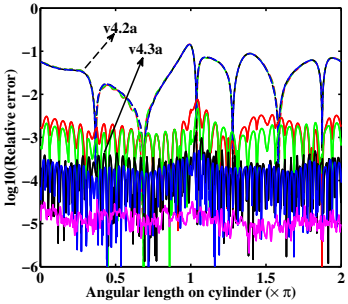

(b) Error in Fig. 4.5(b).

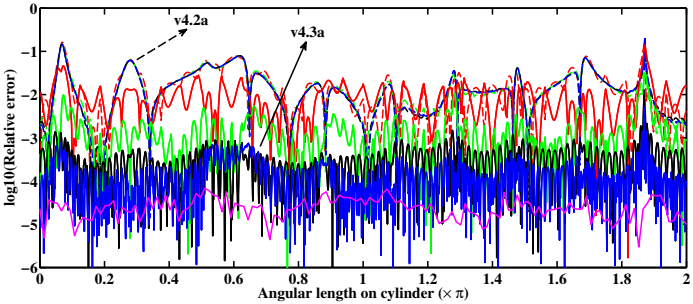

(c) Error in Fig. 4.5(c).

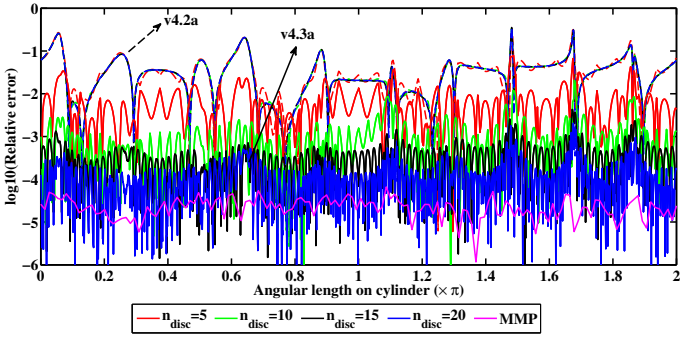

(d) Error in Fig. 4.5(d).

Figure 4.6: Comparison of relative MMP and Comsol errors (in H_z field) on the cylindrical scatterer boundary, in logarithmic scale. Dashed lines: Comsol 4.2a, Solid lines: Comsol 4.3a. Magenta solid line: MMP mismatch error.

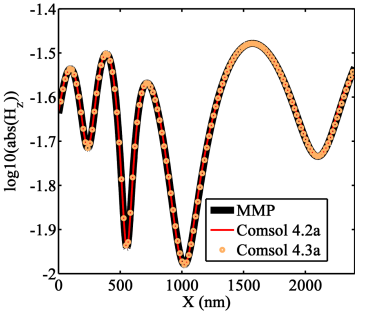

(a) On Fig. 4.3(a).

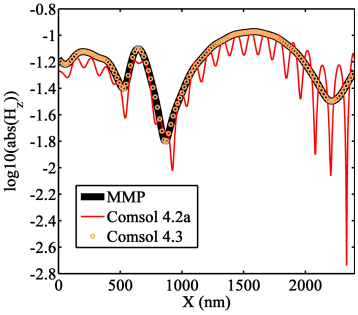

(b) On Fig. 4.3(b).

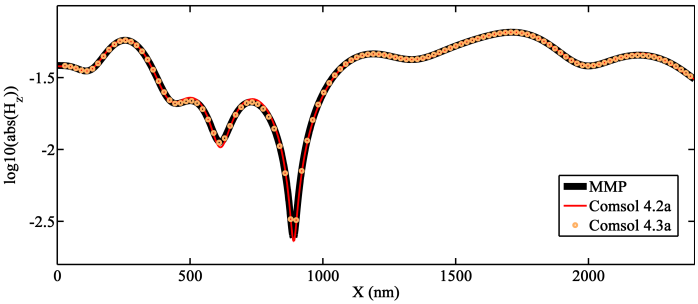

(c) On Fig. 4.3(c).

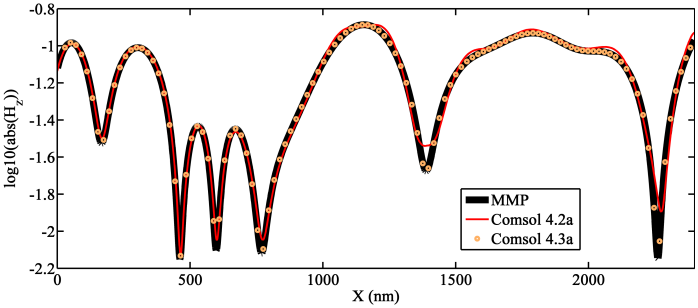

(d) On Fig. 4.3(d).

Figure 4.7: Comparison of MMP and Comsol results on the boundary between layers 1 and 2 in Fig. 4.3, in logarithmic scale.

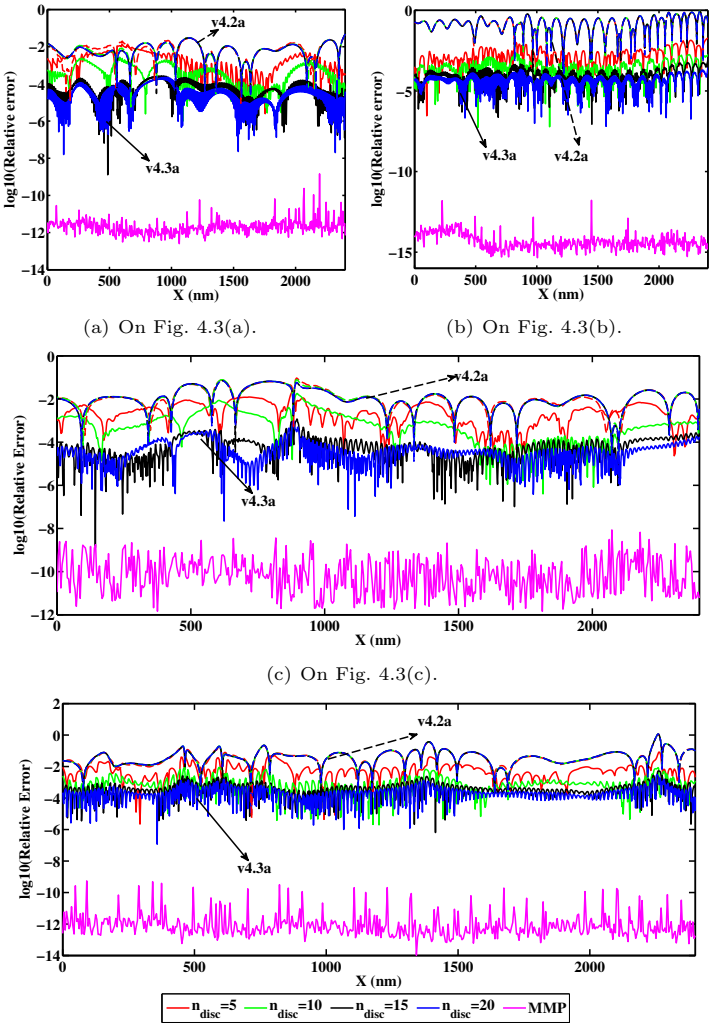

(a) On Fig. 4.3(a).

(b) On Fig. 4.3(b).

(c) On Fig. 4.3(c).

(d) On Fig. 4.3(d).

Figure 4.8: Comparison of relative MMP and Comsol errors (in H_z field) on the boundary between layers 1 and 2 in Fig. 4.3, in logarithmic scale. Dashed lines: Comsol 4.2a, Solid lines: Comsol 4.3a. Magenta solid line: MMP mismatch error.

other results. Following this observation, it turns out that the PML definition of Comsol Multiphysics 4.2a has errors and as a result, truncation of layers in the lateral direction does not work as it should. However, in Comsol Multiphysics 4.3a, this error is eliminated and the corresponding results are in good agreement with the MMP results. Even though the results obtained by Comsol Multiphysics 4.2a looks reasonable at a first glance, it turns out that they are not accurate. One should be always careful in such analyses by FEM, since there is no direct analytical error measure available to check the accuracy of the results, as in MMP.

4.2 Complex origin layered expansions: decreasing computational effort

As discussed in section 2.5, the radiation pattern of infinitesimal sources can be changed by shifting their origin location into complex space. The complex origin expansions generate beams that fan out from a line (in 2D) or a circle (in 3D) as opposed to the real origin expansions that generate cylindrical and spherical waves that fan out from a point, i.e. from the origin. The shape and the direction of the beams can be controlled by the imaginary parts of the origin of the corresponding infinitesimal source, as described in Fig. 2.9. By using these infinitesimal sources as an expansion set in the MMP, it is possible to decrease the total number of expansions and the solution time for the simulations, especially for long structures compared with the wavelength. In this section, such an example will be analyzed 1) by using only real origin expansions and 2) by using a combination of complex and real origin expansions.

In this example, an Ag scatterer ($\varepsilon_{r,Ag,600nm} = -15.85 + i0.43$) [66] is placed in a three layered geometry, where the layer on the bottom is Ag, the medium on top is air and the layer in between, in which the scatterer is placed, is a dielectric material with $\varepsilon_r = 4.0$ and $d = 300$nm [51]. The incident field is a H_z polarized plane wave impinging normally on the system from top with $\lambda_0 = 600$nm. The two different approaches used for the solution of this problem are shown in Fig. 4.9. In the first approach (Fig. 4.9(a)), only a set of real origin layered expansions are used to obtain the field outside the scatterer, whereas in the second one (Fig. 4.9(b)), both the real and complex origin layered expansions are used. A comparison of the total number of expansions reveals that 70 real origin layered expansions are replaced by 16 (in the figure there are two expansions at the same location of the complex origin expansions, shining field into two different directions) complex origin layered expansions. As a result of this replacement, the problem is solved in half the time required before. The solution of the problem can be seen in Fig. 4.10.

For both of the settings shown in Fig. 4.9, the solutions for the problem are

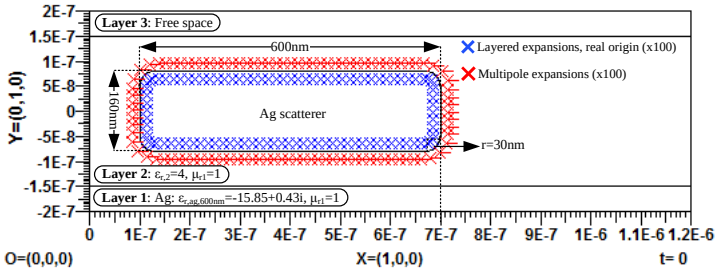

(a) MMP solution setting with real origin expansions.

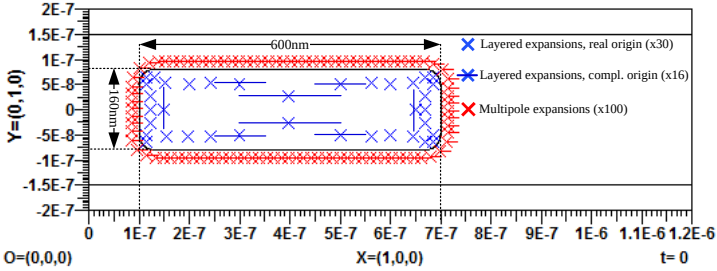

(b) MMP solution setting with complex origin expansions.

Figure 4.9: The geometry and the two different MMP settings for the solution. The incident field is a H_z polarized plane wave impinging normally on the geometry from top with $\lambda_0 = 600$nm.

obtained by using 250 matching points with the relative error criteria less than 0.5% and 0.09% for the complex and real origin cases, respectively. The fields and the error distributions on the scatterer are compared in Fig. 4.11. As a result of this analysis, it is shown that the complex origin expansions can be used to decrease the computational effort for a problem, provided that a set of real origin expansions can be interchanged by a single complex origin expansion.

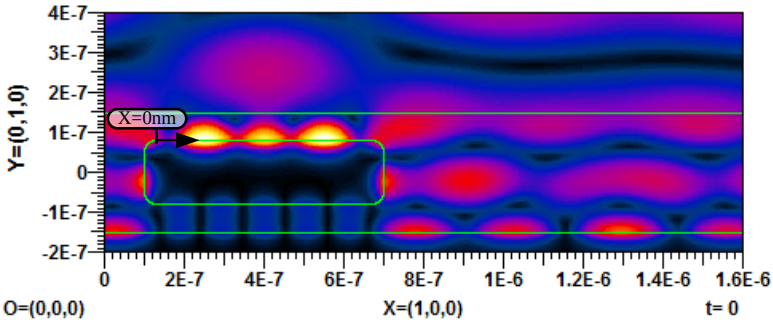

Figure 4.10: The result of the problem shown in Fig. 4.9. Surface: the magnitude of the total H field, z component. Both of the settings in Fig. 4.9 give the same field profile plotted here.

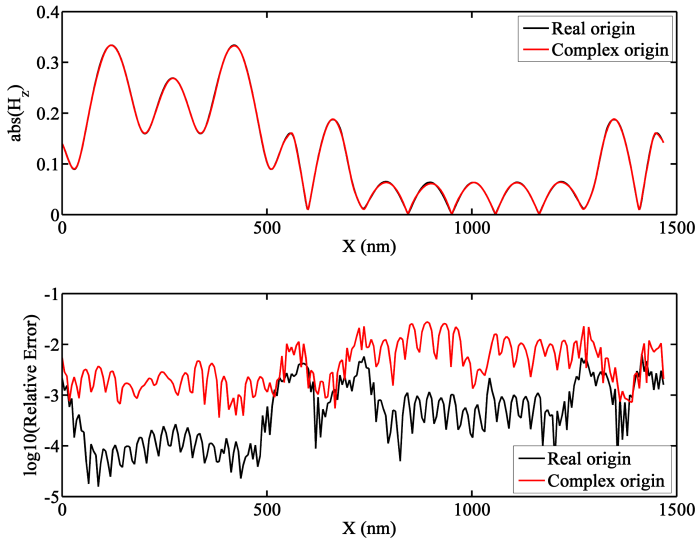

Figure 4.11: Magnitude of H-field, z-component (evaluated at 1000 points) and the relative MMP mismatch error (at 250 points) on the boundary of the scatterer for the problem shown in Fig. 4.9. $X = 0$ corresponds to the point $(130, 80)$nm and the field and error values are obtained in the clockwise direction, as shown by the arrow in Fig. 4.10.

4.3 3D Scattering analysis: scattering cross section of a plasmonic particle in layered media

As a last example for the scattering analysis, a spherical plasmonic particle is placed in a 3 layered geometry as shown in Fig. 4.12[3], where the second layer has the thickness value of t. The full 3D schematic of the problem can be seen

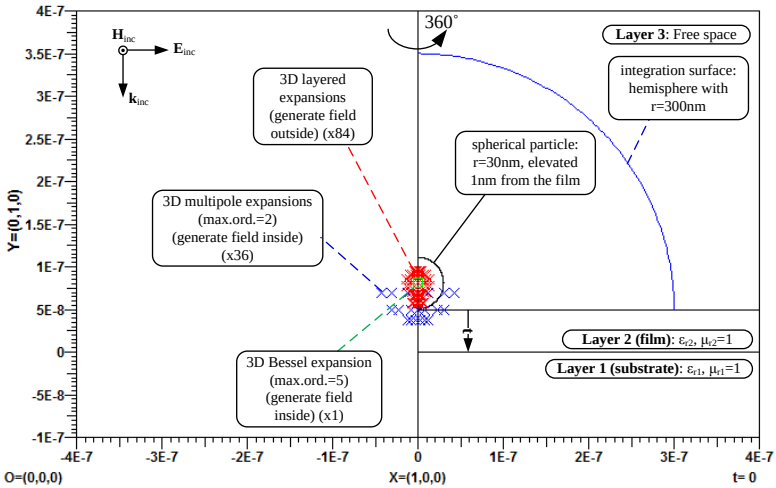

Figure 4.12: The geometry and incident field definition for the 3D scattering cross section analysis. A spherical particle with $r = 30$nm is placed in a 3 layered geometry, elevated 1nm from the film (layer 2) with the thickness value of t. The incident field is an H_z polarized plane wave impinging normally on the structure. The locations (projected on XY plane) and the specifications of the expansions used for the MMP analysis are also plotted.

in Fig. 4.13, where the matching points are placed at the centers of the patches. It should be reminded that, only the patches on the sphere are used in the MMP solution as in the 2D examples above in sections 4.1 and 4.2, since the boundary conditions in the layered geometry are fulfilled by the definition of the layered expansions. For all the results shown in this section, 84 layered expansions are used to model the field outside of the particle and 36 multipole expansions (with the maximum order and degree of 2) together with a Bessel

[3]This geometry was analyzed in [47], when the sphere and the film are taken to be Au [66] with a glass ($\varepsilon_r = 2.28$) substrate. In this example, the material properties of the sphere, film and the substrate are changed in order to analyze the effect of different materials in the scattering cross section data.

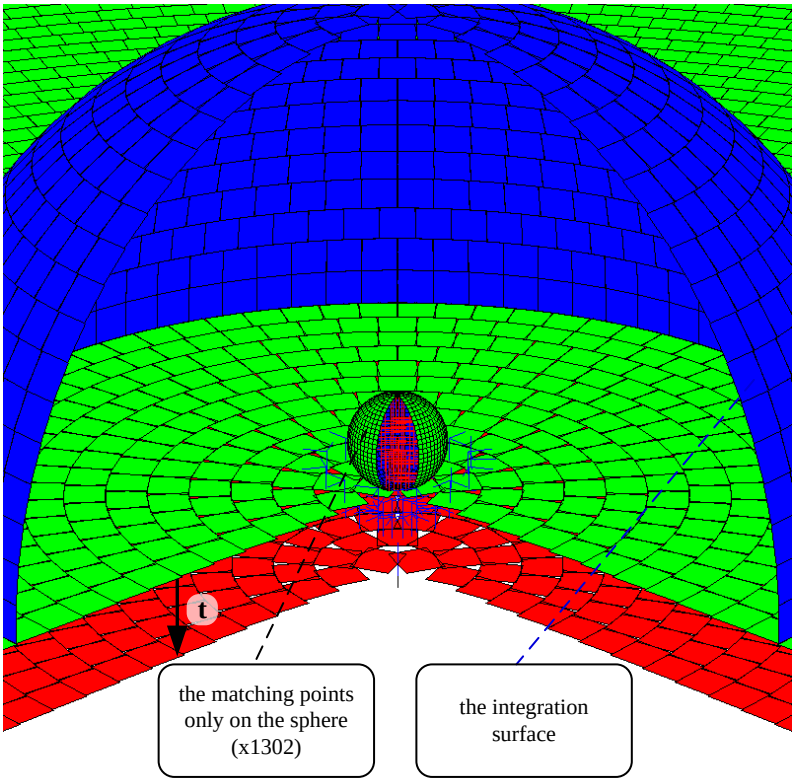

Figure 4.13: The 3D schematic of the scattering analysis: the MMP problem is solved by using the patches on the spherical particle as matching points. The normal component of the time averaged scattered Poynting vector is integrated on the blue hemisphere to obtain the back scattering cross section data.

expansion (with the maximum order and degree of 5) are used to model the field inside the particle. Since the particle is placed very closely to the film, the near field interactions between the particle and the film become the most important part of this problem where a high deviation in the magnitude and the phase of the fields are expected. Therefore, several multipoles are placed for modeling the fields inside the particle more accurately in addition to the

Bessel expansion[4]. Due to the same fact, several layered expansions are placed near the gap between the particle and the film inside the particle, as seen in Fig. 4.12. For the MMP solutions, a total of 1302 matching points distributed equidistantly on the particle are used and the results are obtained within the average error criteria less than 0.05%.

In this example, the back scattering cross section data are calculated on the hemisphere shown in Fig. 4.13[5]. The spherical particle and the film are taken to be Au or Ag [66], whereas the substrate is taken as glass (with the permittivity value of $\varepsilon_{r,gl} = 2.28$) [47] or a dielectric material with $\varepsilon_{r,sub} = 9.0$. Below, the back scattering cross section data are plotted for the Ag and Au particles in Figs. 4.14 and 4.15, respectively. In the results, one can see that the scattering cross section of the particle placed in the layered geometry (Fig. 4.13) show completely different characteristics for different material combinations.

For the Ag sphere case, several additional peaks are observed in the presence of the Ag film as seen in Fig. 4.14(a) and 4.14(b), as opposed to the Au film case, where a single peak is observed for all the thickness values as seen in Figs. 4.14(c) and 4.14(d). In the case of the glass substrate with no film in Fig. 4.14(a), the peak observed in free space at 371nm is shifted to 377nm. Placing the Ag film adds more peaks to the scattering cross section, mainly due to the field resonances in the gap between the Ag sphere and Ag spacer, especially when the thickness of the film is high, which limits the power flow into the substrate (i.e. t=18nm and t=50nm cases in Fig. 4.14(a)). In the case of a dielectric substrate with $\varepsilon_{r,sub} = 9.0$, the peak in free space splits into two peaks at 363nm and 387nm, again due to the resonances between the dielectric with $\varepsilon_{r,sub} = 9.0$ and the Ag particle. Since the dielectric is denser than glass electrically, it is possible to capture fields more strongly in the gap between the particle and the substrate, which introduces an additional peak at 363nm and shifts the free space one to 387nm. Once a film is placed on the substrate, several additional peaks are observed for all the thickness values due to the dense nature of the substrate. In the case of a Ag particle-Au film configuration (Figs. 4.14(c) and 4.14(d)), there are no additional peaks observed, due to the highly lossy nature of Au. It is not possible to concentrate fields in between the Ag particle and Au sphere since the majority of the energy is lost in the Au film. This can be justified in Fig. 4.14(d), where the additional relatively thin Au film (i.e. t=5nm or t=10nm cases in Fig. 4.14(d)) smooths out the two peaks observed in the particle-substrate interface case (i.e. t=0nm in Fig. 4.14(d)).

When the particle is taken as Au, the most important difference is observed

[4] In the 2D example in section 4.1, the cylindrical particle is relatively away from the boundaries of the layers and therefore a single higher order Bessel expansion is enough to model fields inside.

[5] The normal component of the time averaged Poynting vector of the scattered fields is integrated.

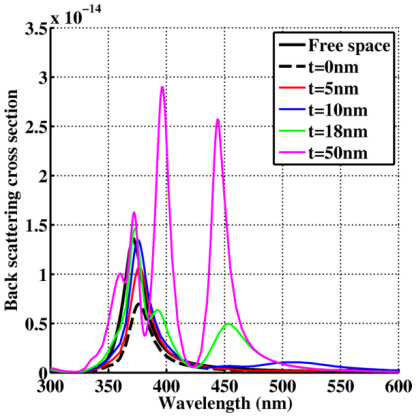

(a) Ag sphere, Ag film with glass substrate ($\varepsilon_{r,sub} = 2.28$).

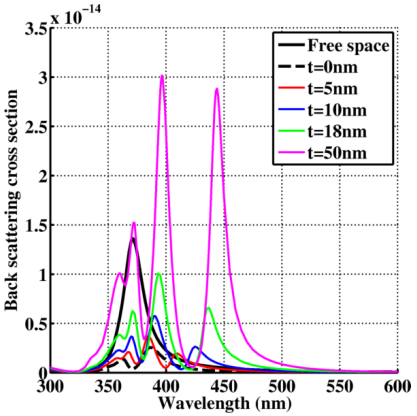

(b) Ag sphere, Ag film with dielectric substrate ($\varepsilon_{r,sub} = 9.0$).

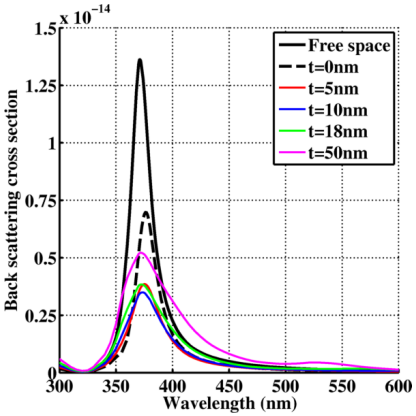

(c) Ag sphere, Au film with glass substrate ($\varepsilon_{r,sub} = 2.28$).

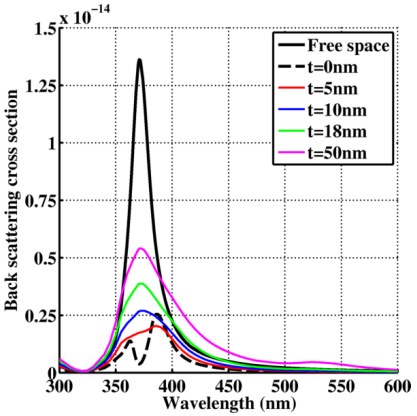

(d) Ag sphere, Au film with dielectric substrate ($\varepsilon_{r,sub} = 9.0$).

Figure 4.14: The back scattering cross section of a Ag spherical particle in a 3 layered geometry with different film thickness values. The material properties of the film and the substrate are given in the caption of each plot.

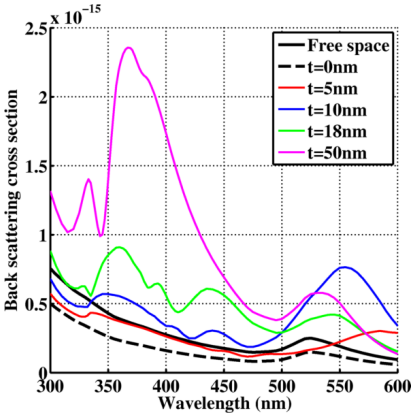

(a) Au sphere, Ag film with glass substrate ($\varepsilon_{r,sub} = 2.28$).

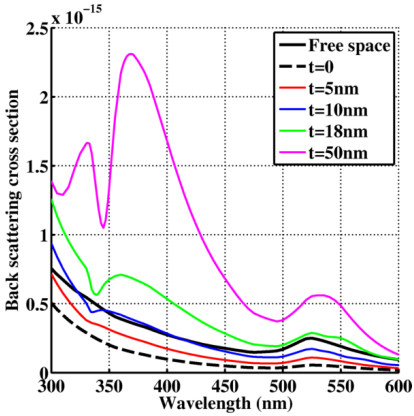

(b) Au sphere, Ag film with dielectric substrate ($\varepsilon_{r,sub} = 9.0$).

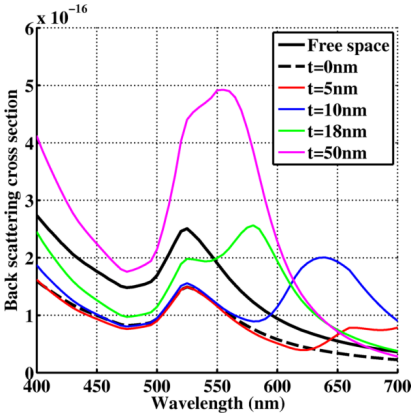

(c) Au sphere, Au film with glass substrate ($\varepsilon_{r,sub} = 2.28$).

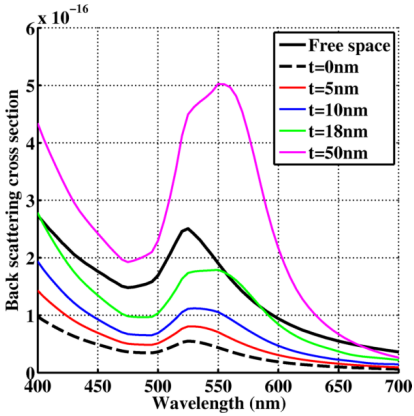

(d) Au sphere, Au film with dielectric substrate ($\varepsilon_{r,sub} = 9.0$).

Figure 4.15: The back scattering cross section of a Au spherical particle in a 3 layered geometry with different film thickness values. The material properties of the film and the substrate are given in the caption of each plot.

in the scattering strength, that can be seen in the y-axis scales of the scattering cross section plots when compared with the Ag particle (i.e. Fig. 4.14 vs. Fig. 4.15). Analyzing these plots reveals that the scattering from the Ag particle is $\sim \times 100$ stronger than the scattering from the Au particle. This difference is due to the highly lossy nature of Au compared to Ag, which also effects the peak shapes of the scattering cross section data as the peaks in the Au sphere case are smoother than the peaks of Ag particle case in general[6].

In order to understand the physical nature of the peaks in the scattering cross section data, the field profiles are plotted for the Ag particle and Ag film configuration with the dielectric substrate (Fig. 4.14(b)), since most of the changes in the scattering cross section are observed in this case. In Fig. 4.16, the magnitude of the H_z field at $\lambda = 371$nm is plotted for the free space case. The inset of the figure shows the same field on the XZ plane at $Y = 50$nm with the bounds of $-50\text{nm} < X < 50\text{nm}$ and $-50\text{nm} < Z < 50\text{nm}$.

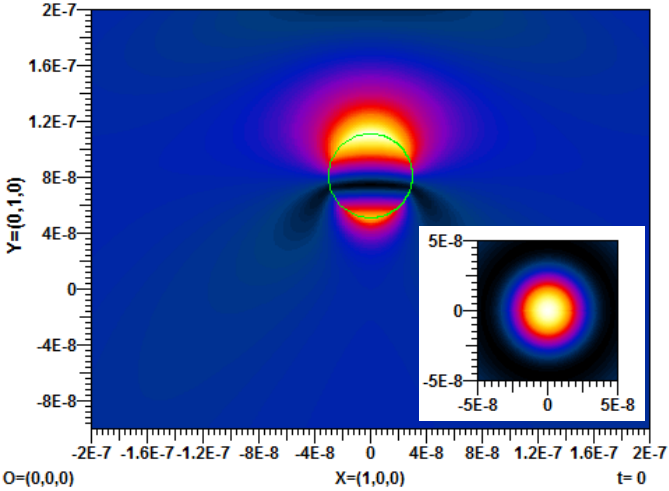

Figure 4.16: The Ag particle in free space at the resonance peak of $\lambda = 371$nm. Surface: Magnitude of H field, z-component. The inset shows the magnitude of the H field z-component as well (a different color map is used given by the corresponding min-max values) on the XZ plane at $Y = 50$nm.

[6]The structure with the Au particle and Au film with the glass substrate was analyzed in [47] and the peak locations are found to be the same with the work introduced here (Fig. 4.15(c)).

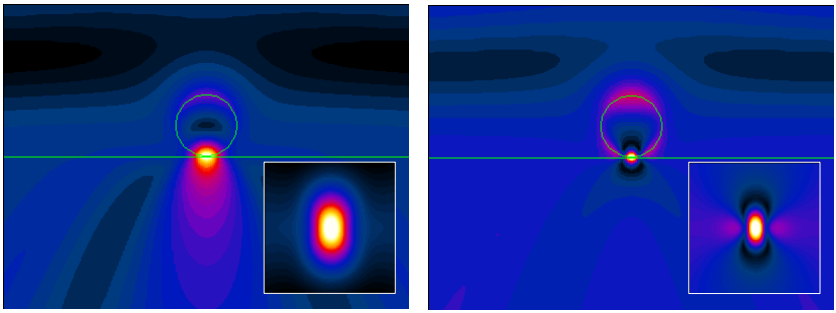

(a) $\lambda = 387$nm. (b) $\lambda = 363$nm.

Figure 4.17: The Ag particle at the resonance peaks of $\lambda = 387$nm and $\lambda = 363$nm when placed directly on a dielectric substrate ($\varepsilon_{r,sub} = 9.0$). Surface: Magnitude of H field, z-component. The same windows in Fig. 4.16 are used here, where the field below the particle on the boundary of the substrate is shown in the inset.

When the particle is placed on a dielectric substrate ($\varepsilon_{r,sub} = 9.0$) the resonance peak in free space splits into two new resonances at $\lambda = 387$nm and $\lambda = 363$nm as discussed above. In Fig. 4.17 the field patterns at the resonance wavelengths are plotted in the same windows as in Fig. 4.16. A comparison between Figs. 4.17(a) and 4.17(b) reveals that with smaller wavelengths it is possible to excite higher order resonances in the structure. This can be validated by the "foot prints" shown as inset in the figures where for higher order resonances the fields are focussed on smaller main hot spots on the substrate. This kind of additional resonances are not seen for the glass substrate since it is not possible to capture fields in the gap between the particle and glass substrate, which has a smaller dielectric constant.

In the presence of a Ag film placed on the dielectric substrate, four peaks are observed in the scattering cross section data at $\lambda = 444$nm, $\lambda = 396.5$nm, $\lambda = 372.5$nm and $\lambda = 360$nm. Since Ag is a better reflector than the dielectric substrate, it becomes possible to capture fields in the gap between the particle and the film at additional wavelengths compared to the only substrate case. The field profiles at the resonance wavelengths can be seen in Fig. 4.18. As in the particle over substrate case, higher order modes are observed for smaller wavelength values.

In the case of other materials (e.g. Fig. 4.15), the field profiles at the resonances are similar to the ones shown in Fig. 4.18, i.e. the peaks in the scattering

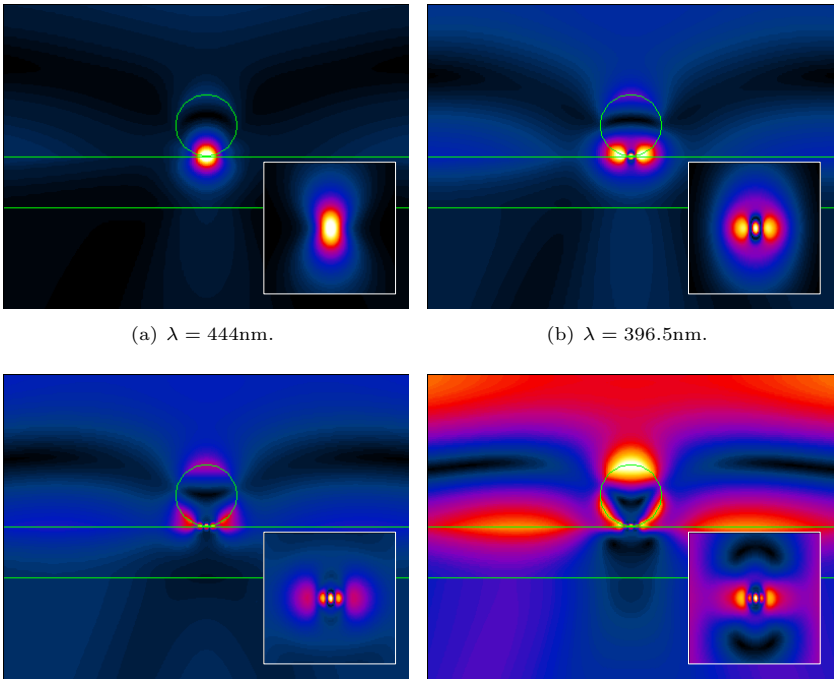

(a) $\lambda = 444$nm. (b) $\lambda = 396.5$nm.

(c) $\lambda = 372.5$nm. (d) $\lambda = 360$nm.

Figure 4.18: The Ag particle on a Ag film with $t = 50$nm over a dielectric substrate ($\varepsilon_{r,sub} = 9.0$) at the resonance peaks of $\lambda = 444$nm, $\lambda = 396.5$nm, $\lambda = 372.5$nm and $\lambda = 360$nm. Surface: Magnitude of H field, z-component. The same windows in Fig. 4.16 are used here, where the field below the particle on the boundary of the film is shown in the inset.

cross section data at higher wavelengths corresponds to lower order resonances. As discussed at the beginning of this section, when Au is used in the structure, the peaks become smoother due to the lossier nature of Au at the wavelength range analyzed in this example [66].

4.4 Eigenvalue analysis of plasmonic waveguides

In this section, several examples of the eigenvalue analysis of plasmonic waveguides are presented. In the examples, the metallic rectangular wire with the same number and location of expansions in section 3.7 are used with different geometry and material parameter combinations[7] in order to observe the effect of changing the material and the position of the wire. In the following, the loci of the eigenvalues on the complex k_γ plane and selected eigenfield profiles are presented. When plotting the loci, the sufficiently large complex k_γ plane with the bounds of $0 < \Re(k_\gamma) < 4k_0$ and $0 < \Im(k_\gamma) < 2k_0$ is used to observe the migration of eigenvalues as a function free space wavelength. The symmetry plane definition in section 3.7 (as shown in Fig. 3.6) is used here as well, for the odd (by taking the symmetry plane as PMC) and even (by taking the symmetry plane as PEC) symmetric cases. In the plots below, the eigenvalues are numbered according to their symmetry types as "Mode$i$ Noj" corresponding to i-symmetric j^{th} eigenvalue. As an example, Mode1 No1 and Mode2 No3 correspond to the first odd eigenvalue and the the third even eigenvalue of the corresponding waveguide structures, respectively. For all the examples shown here, the same technique as described in section 3.6 is used as follows: 1) the MMP search function data at a number of free space wavelength values are calculated in order to obtain the exact number and the approximate locations (observed as the minima locations of the search function) of the eigenvalues in the given complex k_γ plane and 2) a fine search is performed around the minima locations of the search functions to obtain the exact locations of the eigenvalues[8].

As the first example [78], the same single wire waveguide geometry in Fig. 3.6 is analyzed, but this time the wire is taken to be Ag [66]. As in the example in section 3.7, layers 1 and 3 are free space and layer 2 is a dielectric material with $\varepsilon_r = 2.0$. The loci of the eigenvalues as a function the free space wavelength can be seen Fig. 4.19 and the arrow shows the direction to which the eigenvalues migrate when the free space wavelength is increased.

A comparison of Fig. 4.19 with Fig. 3.7 reveals that the wavelength dependent loci of the eigenvalues on the given k_γ plane changes abruptly for different material properties of the wire. Firstly, the imaginary parts of the eigenvalues

[7] For the 2 wire waveguide example in this section, the number of expansions is doubled and the expansions are distributed along the whole wire, where the symmetry plane is placed in between the wires. As a result, the whole wire is analyzed as opposed to the half wire analysis that is performed for the single wire waveguides.

[8] The second step is co operated with the eigenvalue parameter estimation routine included in OpenMaX 2013A [48] to obtain the wavelength dependent behavior of the eigenvalues without calculating the MMP search function data for all the wavelength values. But one should be careful since additional eigenvalues may appear in the given k_γ plane for some wavelength values. Therefore calculating the search function *at a number of wavelength values* is needed in step 1 in order to eliminate such a problem.

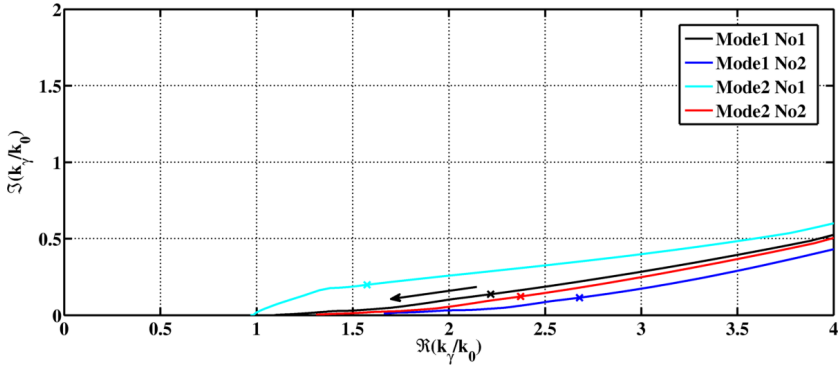

Figure 4.19: The loci of the eigenvalues of the waveguide with the dimensions shown in Fig. 3.6. For this analysis the wire is taken to be Ag, layers 1 and 3 are free space and layer 2 is a dielectric material with $\varepsilon_r = 2.0$. The arrow shows the migration direction of the eigenvalues when the free space wavelength is increased. The crosses show the location of the eigenvalues at $\lambda_0 = 410$nm and the corresponding eigenfields are plotted in Fig. 4.20.

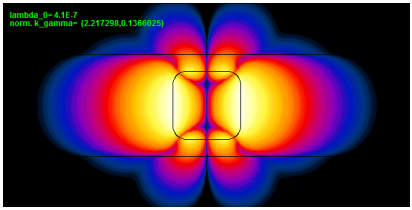

(a) Mode1 No1 @$(2.22+0.14\mathrm{i})k_0$

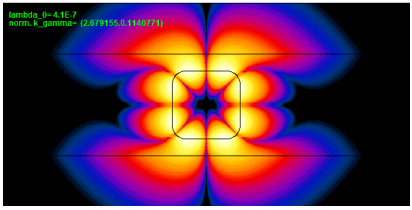

(b) Mode1 No2 @$(2.68+0.11\mathrm{i})k_0$

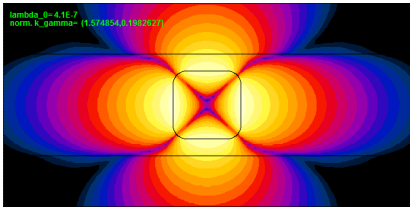

(c) Mode2 No1 @$(1.57+0.19\mathrm{i})k_0$

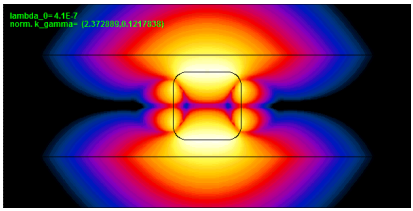

(d) Mode2 No2 @$(2.37+0.12\mathrm{i})k_0$

Figure 4.20: Eigenfields of the Ag waveguide analyzed in Fig. 4.19, evaluated at $\lambda_0 = 410$nm. The same window shown in Fig. 3.6 is used. Surface: H field z-component in the logarithmic scale. The corresponding eigenvalues are given in the captions of each eigenfield and shown as crosses in Fig. 4.19.

of the Ag wire have a smaller imaginary part than the Au wire case. This is due to the lossier nature of Au compared to Ag in the optics regime, as also observed in the back scattering calculations of a plasmonic particle in section 4.3. Secondly, the real part of the eigenvalues of the Au waveguide are bound to lower k_γ values compared Ag wire, which corresponds to higher radiation losses for Au wire waveguide [9]. In order to see the physical meaning of the eigenvalues, all the eigenfields observed at $\lambda_0 = 410$nm (shown as crosses in Fig. 4.19) on the given k_γ plane are plotted in Fig. 4.20. A comparison between the eigenfields of the Au (in Fig. 3.8) and Ag (in Fig. 4.20) wire waveguides reveals that the fields are mostly concentrated near the wire in the Ag wire case. Whereas in the Au wire, more fields are penetrated in the dielectric slab, since the real parts of the corresponding eigenvalues are lower than the Ag wire example. As a result, for the Ag wire case, FEM analysis give the exact same eigenvalues as shown here with an arbitrary real initial guess (greater than the wave number of the slab, i.e. > 1.41), due to the fact discussed in the example in section 3.7.

In the second example, the previous geometry is used with a Au wire placed in a Ag backed dielectric slab, i.e. in Fig. 3.6 layer 1 is Ag, layer 2 is dielectric with $\varepsilon_r = 2.0$, layer 3 is free space and the wire is Au, for this example. The loci of the eigenvalues as a function of free space wavelength is plotted in Fig. 4.21.

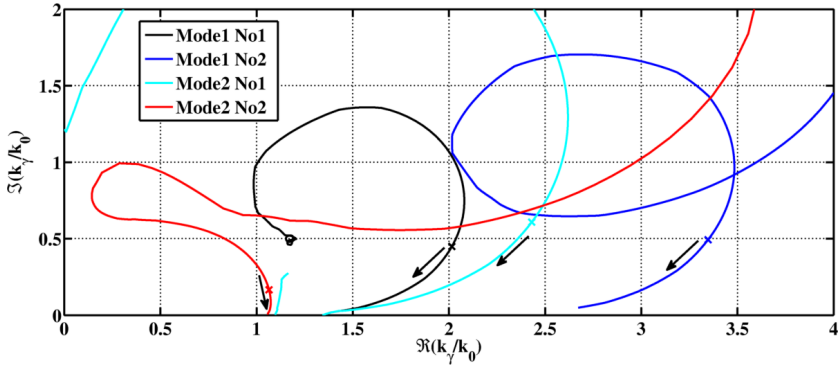

Figure 4.21: The loci of the eigenvalues of the waveguide with the dimensions shown in Fig. 3.6. For this analysis the wire is taken to be Au, layers 1 is Ag, layer 2 is a dielectric material with $\varepsilon_r = 2.0$ and layer 3 is free space. The arrows show the migration direction of the eigenvalues when the free space wavelength is increased. The crosses show the location of the eigenvalues at $\lambda_0 = 550$nm and the corresponding eigenfields are plotted in Fig. 4.20.

[9] In general, the rule: "smaller the real part of eigenvalue, higher the field propagation in XY plane (also seen in the 2D Green's functions definitions with non zero k_γ, e.g. as in A.2)" is used to draw this conclusion.

As one can see, changing the substrate to Ag results in abrupt changes in the behavior of the eigenvalues. Even though circular eigenvalue loci are observed in both of the Au waveguide examples (Fig. 3.7 vs. Fig. 4.21) the radii of the loci and their position on the given complex k_γ plane are different which is not easy to predict without the MMP search function data. The eigenfields of this structure at $\lambda_0 = 550$nm are plotted in Fig. 4.22. Similar to the previous

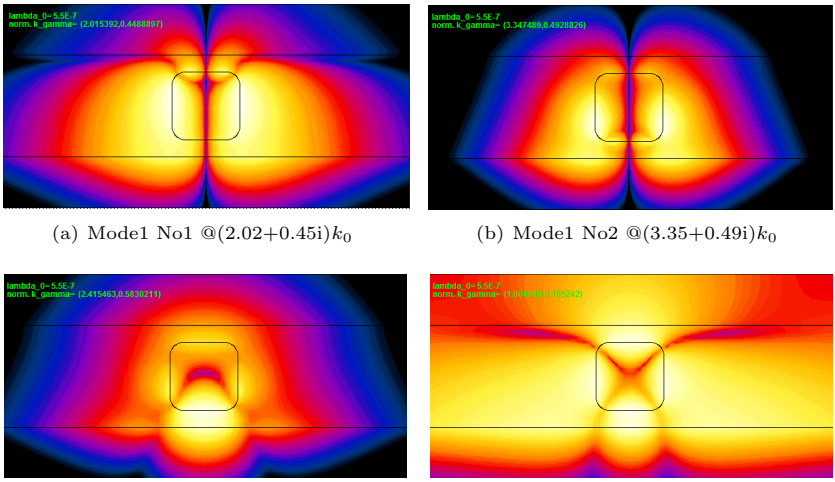

(a) Mode1 No1 @$(2.02+0.45\mathrm{i})k_0$ (b) Mode1 No2 @$(3.35+0.49\mathrm{i})k_0$

(c) Mode2 No1 @$(2.43+0.61\mathrm{i})k_0$ (d) Mode2 No2 @$(1.06+0.17\mathrm{i})k_0$

Figure 4.22: Eigenfields of the Au waveguide analyzed in Fig. 4.21, evaluated at $\lambda_0 = 550$nm. The same window shown in Fig. 3.6 is used. Surface: H field z-component in the logarithmic scale. The corresponding eigenvalues are given in the captions of each eigenfield and shown as crosses in Fig. 4.21.

example, in the mode with lower real part (Fig. 4.22(d)) the fields penetrate to the dielectric slab more whereas in the other modes the fields are mostly localized on the Au wire.

As the third example, a double Au wire waveguide structure is analyzed in the same layered geometry as in the previous example, i.e. layer 1 is Ag, layer 2 is dielectric with $\varepsilon_r = 2.0$, layer 3 is free space. The separation between the two wires is 50nm and they are placed in the middle of the second layer in y direction as in the previous examples. As discussed in the beginning of this section, the symmetry plane is set to be in between the wires and as a result, the whole wire structure is analyzed, as opposed to the half wire analysis for the single

wire examples given above. The loci of the eigenvalues as a function of free space wavelength is plotted in Fig. 4.23. As one would expect, the additional

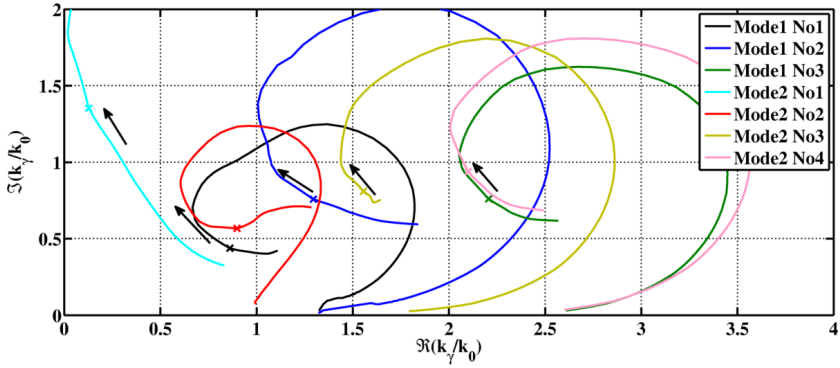

Figure 4.23: The loci of the eigenvalues of the double wire (separated by 50nm) waveguide. For this analysis the wire is taken to be Au, layers 1 is Ag, layer 2 is a dielectric material with $\varepsilon_r = 2.0$ and layer 3 is free space. The arrows show the migration direction of the eigenvalues when the free space wavelength is increased. The crosses show the location of the eigenvalues at $\lambda_0 = 460$nm and the corresponding eigenfields are plotted in Fig. 4.24.

wire introduces additional eigenvalues in the given k_γ plane, having circular shapes as in the previous Au wire examples. As one can see in Fig. 4.23, some of the eigenvalues are very close to each other in the double wire waveguide example presented here, i.e. the loci of Mode1 No3 - Mode2 No4, Mode1 No2 - Mode2 No3 and Mode1 No1 - Mode2 No2 pairs pass close to each other. If one does not use the symmetry planes in the analysis, this can present problems in numerical methods when determining the wavelength dependent behaviors of the corresponding eigenvalues. When tracing the eigenvalues on the given k_γ plane, it would be quite easy for the tracing routines to switch from one eigenvalue to the other, which is of course not desired. Therefore one can conclude that it is always advantageous to use the symmetry planes (in general, as many as possible) in order to sperate eigenvalues to different subproblems (e.g. here Mode1 and Mode2 are the two subproblems) and therefore to decrease the complexity and the computational cost of such eigenvalue problems. The eigenfields of this structure at $\lambda_0 = 460$nm are plotted in Fig. 4.24. A similar conclusion can be drawn for the double wire example as in the case of single wire cases, i.e. the real part of the eigenvalues are directly related to the radiation losses. For smaller values of the real part the radiation loss increases since a higher portion of the waves can propagate in the XY plane.

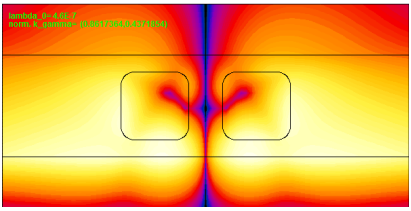

(a) Mode1 No1 @$(0.86+0.44\mathrm{i})k_0$

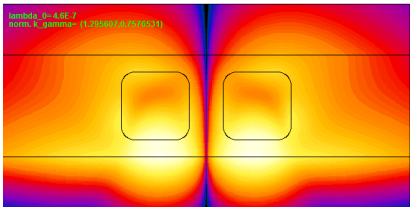

(b) Mode1 No2 @$(1.30+0.76\mathrm{i})k_0$

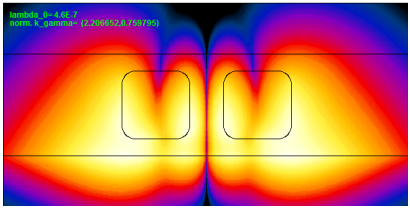

(c) Mode1 No3 @$(2.21+0.76\mathrm{i})k_0$

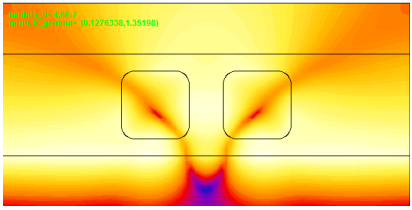

(d) Mode2 No1 @$(0.13+1.35\mathrm{i})k_0$

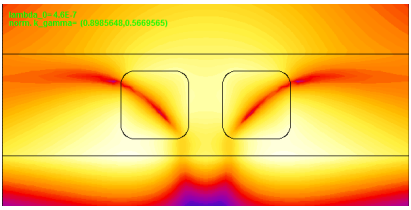

(e) Mode2 No2 @$(0.90+0.57\mathrm{i})k_0$

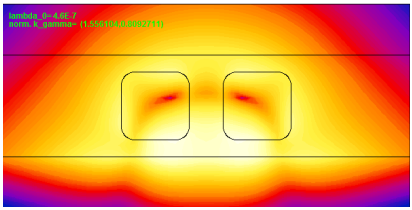

(f) Mode2 No3 @$(1.56+0.81\mathrm{i})k_0$

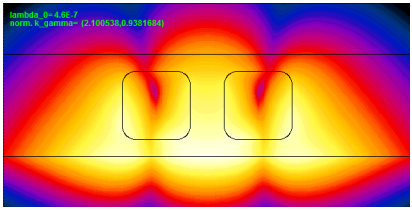

(g) Mode2 No4 @$(2.10+0.94\mathrm{i})k_0$

Figure 4.24: Eigenfields of the double Au waveguide analyzed in Fig. 4.23, evaluated at $\lambda_0 = 460$nm. The same window shown in Fig. 3.6 is used. Surface: H field z-component in the logarithmic scale. The corresponding eigenvalues are given in the captions of each eigenfield and shown as crosses in Fig. 4.23.

In the last eigenvalue example, a single Au wire is placed on top of a Ag backed (layer 1 is Ag) glass slab ($\varepsilon_r = 2.25$ for layer 2) with the thickness value of 150nm in a free space environment (layer 3 is free space). The same dimensions are used for the wire as in the previous cases. The loci of the eigenvalues as a function of free space wavelength is plotted in Fig. 4.25 and the eigenfields evaluated at $\lambda_0 = 510$nm are shown in Fig. 4.26.

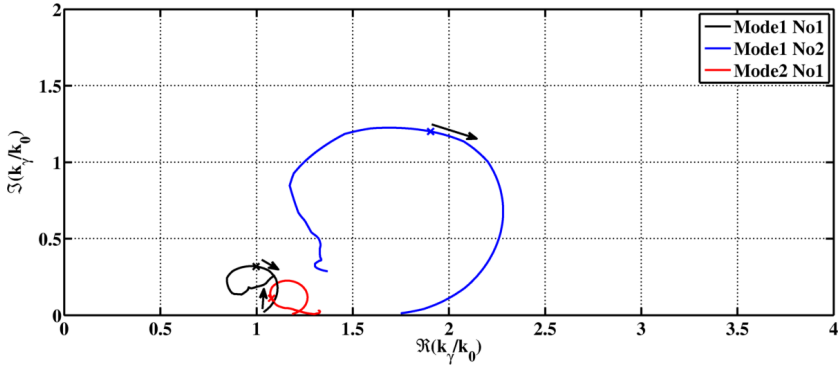

Figure 4.25: The loci of the eigenvalues of the single Au wire waveguide placed on a Ag backed dielectric slab with $\varepsilon_r = 2.25$. The arrows show the migration direction of the eigenvalues when the free space wavelength is increased. The crosses show the location of the eigenvalues at $\lambda_0 = 510$nm and the corresponding eigenfields are plotted in Fig. 4.26.

As demonstrated by the examples of different waveguides, the loci and the number of eigenvalues in a given k_γ plane can not be predicted when lossy and dispersive materials are used, even for waveguides with simple geometrical features. As discussed in section 3.7, the lack of a good initial guess for the eigenvalues causes problems and it is highly possible to end up with an arbitrary number of non physical eigenvalues. In order to tackle this problem, the MMP search function data, that is calculated in an intermediate step of the eigenvalue analysis performed by MMP, can be used to obtain an efficient initial guess and the number of eigenvalues in the given k_γ plane. In this section, it is also shown that the eigenvalue analysis by MMP described in section 3.6 can be used in a robust way for different waveguide geometries built in layered geometries. As in the case of the scattering analysis, using the layered media Green's functions as an expansion set in the eigenvalues analysis (2D layered expansions with non zero k_γ) decreases the complexity of the problems and can be co-operated with any other numerical method for obtaining meaningful initial guesses.

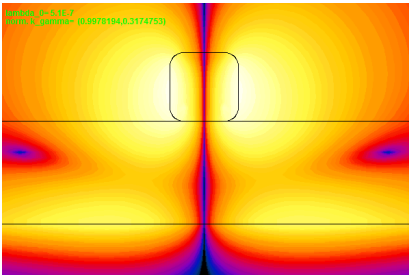

(a) Mode1 No1 @(1.00+0.32i)k_0

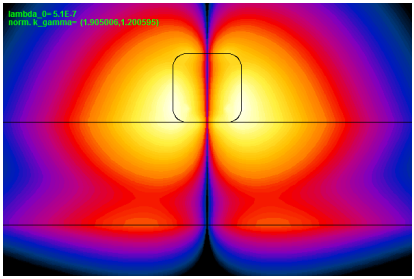

(b) Mode1 No2 @(1.91+1.20i)k_0

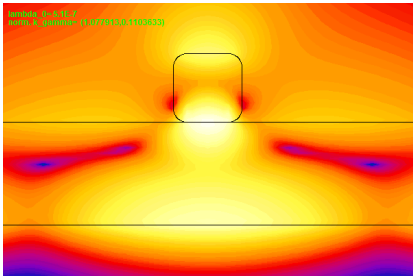

(c) Mode2 No1 @(1.08+0.11i)k_0

Figure 4.26: Eigenfields of the Au waveguide analyzed in Fig. 4.25, evaluated at $\lambda_0 = 510$nm. The same window shown in Fig. 3.6 is used. Surface: H field z-component in the logarithmic scale. The corresponding eigenvalues are given in the captions of each eigenfield and shown as crosses in Fig. 4.25.

4.5 Optimization of plasmonic structures

As the last example, an optimization problem defined for a 2D plasmonic structure built in a layered geometry is analyzed. In the problem, a monopole antenna (modeled by a 2D point source) generating H_z polarized fields with $\lambda_0 = 600$nm is placed at a fixed location over a Ag [66] backed glass slab (ε_{r2}=2.25, d=200nm). The two goals defined for the optimization problem is to 1) maximize or 2) minimize the total power flow inside the glass slab at a given region by determining the optimum geometrical parameters of 2 Ag cylindrical scatterers placed inside the glass slab. The geometrical parameter and the fitness value definitions of the problem can be seen in Fig. 4.27. By definition,

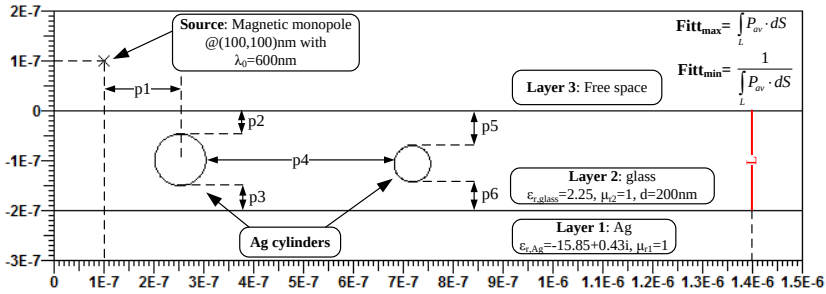

Figure 4.27: The geometrical setting of the optimization problem. There are two different goals defined: 1) maximize or 2) minimize the integral of the time averaged Poynting vector integral evaluated on the red line L, by determining the optimal values of the parameters p1 ... p6, as shown above. The two fitness definitions used for the problem are shown in the figure as $\mathbf{Fitt_{max}}$ and $\mathbf{Fitt_{min}}$, respectively. As the incident field generator, a magnetic monopole (generating H_z polarized waves) with $\lambda_0 = 600$nm is placed at (100,100)nm. The parameters used in the optimization have the bounds of $\langle 0, 400\rangle$nm for p1 and $\langle 20, 90\rangle$nm for p2, p3, p5, p6. Two different bounds are used for p4: 1)$\langle 20, 400\rangle$nm and 2)$\langle 20, 600\rangle$nm.

optimization methods are used to maximize the fitness values by determining the optimal values of the parameters used. For the first problem defined above (maximization), the fitness value is defined directly as the integral of the Poynting vector. In the case of the second problem (minimization), the fitness value is taken to be 1/ the integral value, as shown in Fig. 4.27. For the solution of the problem defined above, an evolutionary optimization strategy is used with MMP updated by layered expansions.

In general, optimization routines work in a simple input-output principle. For the specific example here, the user defines the bounds of the parameters to be optimized (as given in the caption of Fig. 4.27 for the specific problem here). The routine uses distinct values chosen from the set of parameters given by the user as the inputs to MMP and gets the resulting fitness values (integral values) as the output. Therefore the numerical model used to analyze the structure in MMP should be robust and give efficient results for all the parameter combinations. For this purpose, the automatic expansion distribution routine in OpenMaX 2013A [48] is used with the maximum distance of 15nm from the boundary and 7.5 nm from the neighboring expansions when placing the layered expansions, responsible for the fields outside the cylinders. For the fields inside, one Bessel expansion placed at the center of each cylinder is used with the maximum order of 20. The matching points are set to be 2 times the number of layered expansions used (or 32 when the number of layered expansions is less than 16 for a given cylinder). By these settings, the relative average error for all the trials analyzed is found to be less than 0.05% which is very accurate for this kind of optimization problems. It should be noted that the integral evaluated without the two cylindrical structures is found to be 91.82[10] and the corresponding field pattern can be seen in Fig. 4.28.

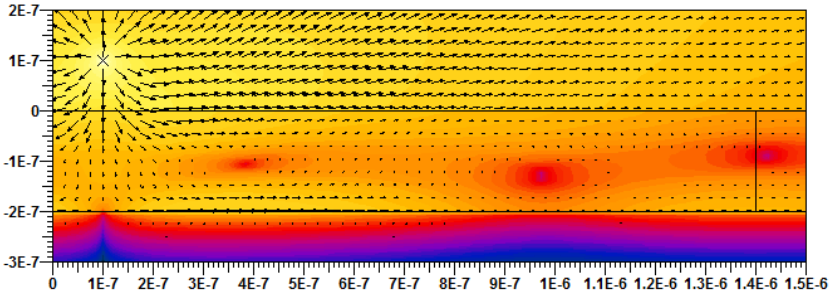

Figure 4.28: The field generated by the monopole antenna without the cylindrical structures to be optimized. Surface: Magnitude of the time averaged Poynting vector, logarithmic scale and Arrows: direction of time averaged power flow. For this case, the integral of the normal component of time averaged Poynting vector evaluated in line L (shown as the black line at x=1400nm passing through the glass slab) is 91.82.

[10] In the layered expansions used in OpenMaX, the magnitudes of the fields are normalized to a point source generating fields at 1Ghz. This normalization has no effect on the solutions, but one should be careful when comparing these results with other numerical methods.

As described above, the parallelized evolutionary strategy [96] optimizer module [8] of OpenMaX 2013A is used together with the MMP updated by layered expansions for this problem. In addition to MMP specifications described above, the optimization routine specifications should be provided for a full mathematical description of the problem. In this optimization problem, the initial population size and number of parents in a given generation is set to be 10 with the mutation strength of 0.2 in between generations. As the stopping criteria for the optimization routine, the total number of individuals created is limited to 1000. The fitness value calculated as a function of the normalized parameters of the optimization problem is shown in Fig. 4.29 and 4.30 for the maximization and minimization problems, respectively.

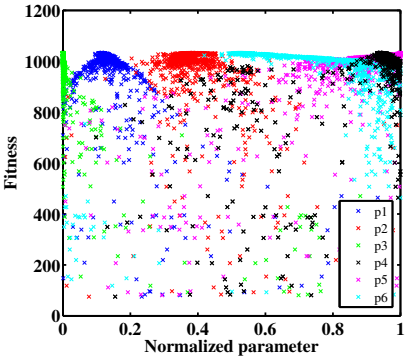

(a) p4$\in \langle 20, 400\rangle$nm. The maximum fitness value of 1032.38 is obtained by p=$\{45.30, 46.80, 20.00, 377.04, 89.99, 56.97\}$ nm.

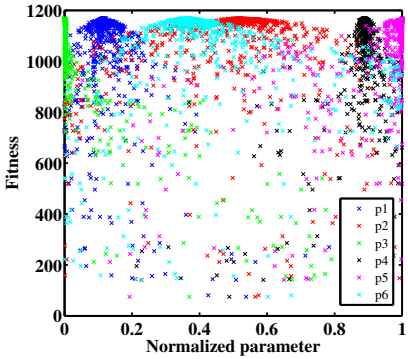

(b) p4$\in \langle 20, 600\rangle$nm. The maximum fitness value of 1168.57 is obtained by p=$\{49.67, 56.63, 20.00, 535.45, 89.96, 45.23\}$ nm.

Figure 4.29: Distribution of the parameters obtained in the maximization (the fitness value is set to be $\mathbf{Fitt_{max}}$ in Fig. 4.27) problem. Bounds of the parameters are provided in the caption of Fig. 4.27 whereas the bounds for p4 is shown in captions of the corresponding figures, together with the optimal parameters obtained.

As one can see, the plots in Fig. 4.29 and 4.30 provide the convergence data of the optimization routine as a function of all the parameters used. Using these plots, one can analyze the accuracy of the overall optimization results and set up additional analysis steps by setting new bounds to the parameters. Comparing Figs. 4.29(a) and 4.29(b) reveals that increasing the upper bound of p4 results in a better fitness value. In addition, some of the parameter values are

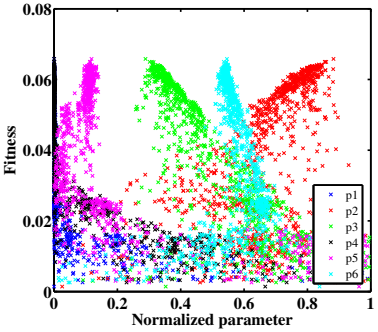

(a) p4$\in \langle 20, 400\rangle$nm. The maximum fitness value of 6.58×10^{-2} (corresponding to the minimal integration result of 15.19) is obtained by p=$\{0.05, 81.76, 40.21, 20.12, 28.28, 58.21\}$ nm.

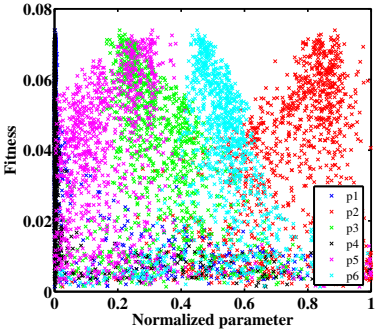

(b) p4$\in \langle 20, 600\rangle$nm. The maximum fitness value of 7.39×10^{-2} (corresponding to the minimal integration result of 13.53) is obtained by p=$\{0.81, 81.98, 34.41, 20.21, 41.46, 51.53\}$ nm.

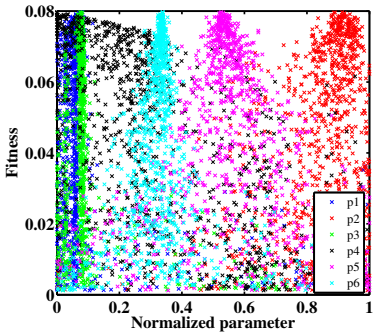

(c) p1$\in \langle 0, 10\rangle$nm and p4 $\in \langle 20, 40\rangle$nm. The maximum fitness value of 7.97×10^{-2} (corresponding to the minimal integration result of 12.54) is obtained by p=$\{0.81, 83.90, 25.23, 20.02, 56.83, 43.67\}$ nm.

Figure 4.30: Distribution of the parameters obtained in the maximization (the fitness value is set to be $\mathbf{Fitt_{min}}$ in Fig. 4.27) problem. Bounds of the parameters are provided in the caption of Fig. 4.27 whereas the bounds for p4 (and p1 in (c)) is shown in captions of the corresponding figures, together with the optimal parameters obtained.

concentrated on specific locations of the plots which means a good convergence is achieved when obtaining the optimal value of the corresponding parameter. In the case of the minimization problem (Fig. 4.30), the parameters are sparsely distributed especially in the case of Fig. 4.29(b). In addition, the two parameters p1 and p4 are concentrated around 0. From this observation, one can conclude that narrower bounds for these two parameters would increase the convergence rate of the whole problem, since the routine will not waste computational effort for searching the optimum value of the two parameters in a broad range. Instead, the computational effort will be used for determining the optimal values of the remanding parameters, supposedly with a better convergence rate. In order to analyze this claim, the same minimization problem is repeated with the two new bounds for p1$\in \langle 0, 10\rangle$nm and p4$\in \langle 20, 40\rangle$nm. The parameter distribution plot of the new optimization can be seen in Fig. 4.30(c), where a better convergence and fitness value is obtained. The field patterns in the optimized structures can be seen Fig 4.31 and 4.32, for the corresponding maximization and minimization problems, respectively.

As can be seen in the field profile plots in Fig. 4.31 as well, the additional two cylinders enhance the power transmitted to the integration line, by generating a hot spot near x=1400nm. Similar to transmission line theory in microwave regime, the power is mainly carried by the guided waves (in this case SPP resonance observed on the Ag substrate at $k_x = (1.58 + 0.01i)k_0$, which is the only guided wave mode supported by the layered medium). The two cylinders act like two lumped elements connected to a transmission line and their position periodically changes the power transmitted to the integration line. At specific distance values (p4 in Fig. 4.27), the two wires act like a resonator increasing (transmitting to right) or decreasing (reflecting back to left) the power delivered to the integration line, as in the case of Fabry Perot resonators or guided waves in layered media, where the phase and the direction of propagation of the waves play the crucial role [45, 97, 98]. Due to the standing wave nature of the fields in such resonators, the resonance length of the structure shows a periodic behavior with the periodicity of $\lambda/2$, where λ is the wavelength in the resonator. In the maximization problem here, using the same logic as in resonators, the response of the system (i.e. the result of the integral) should have a periodic nature with the periodicity given by the wavelength of the guided wave mode:

$$\frac{\lambda_{SPP}}{2} = \frac{\lambda_0}{2\Re(k_{SPP})} = \frac{600\text{nm}}{2\Re(1.58 + 0.01i)} \approx 190\text{nm} \tag{4.1}$$

In order to test this claim, the effect of the distance between the two cylinders on the integration values is analyzed by using the parameters (all the parameters are taken as they are, only the parameter for the distance between the 2 cylinders, p4, is varied in $\langle 200, 1000\rangle$nm) obtained for the optimized structures shown in Fig. 4.31. The resulting p4 vs. fitness plot can be seen in

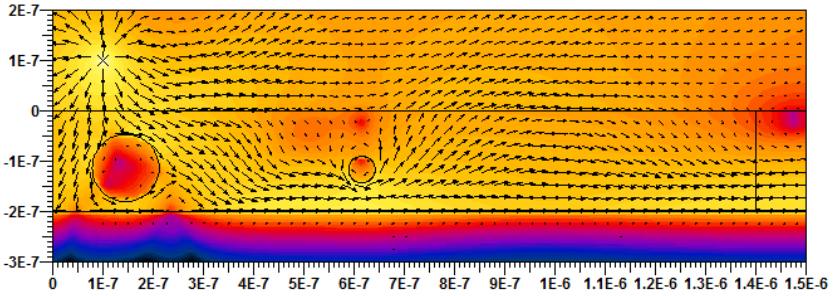

(a) Parameters obtained from Fig. 4.29(a) with the integration result of 1032.38.

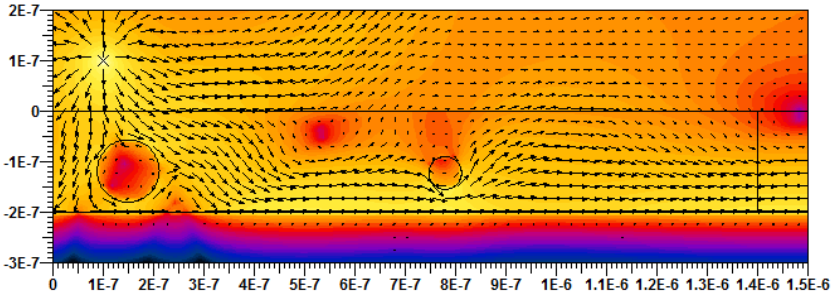

(b) Parameters obtained from Fig. 4.29(b) with the integration result of 1168.57.

Figure 4.31: Field patterns of the optimized structures for the maximization problem. Surface: Magnitude of the time averaged Poynting vector, logarithmic scale and Arrows: direction of time averaged power flow. An improvement of $\times 11.25$ and $\times 12.73$ is achieved in the integral value, compared to the structure without the cylinders in Fig. 4.28.

Fig. 4.33. As predicted by the technique used in the microwave regime described above, the distance between the two consecutive maxima (and minima) is $\lambda_{SPP}/2 \approx 190$nm. The distance between the two maxima deviates a little from the exact λ_{SPP} value, since other field natures in addition to the SPP wave (mainly propagating directly from the source to the cylinders) and the hot spot locations on the cylinders effect the field pattern in the structure. Using the microwave regime analogy above, these effects corresponds to changes in the impedances of the lumped elements, resulting in deviations in the periodicity of the response of the system.

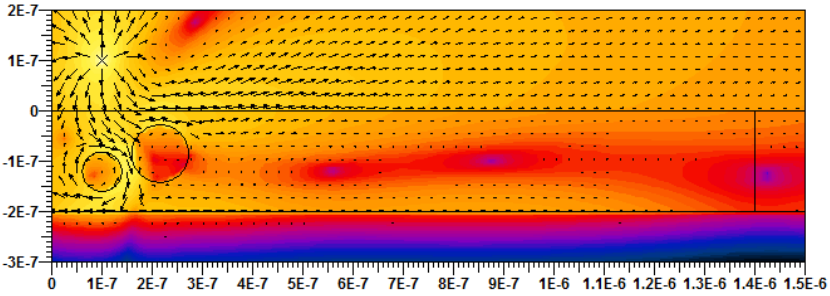

(a) Parameters obtained from Fig. 4.30(a) with the integration result of 15.19.

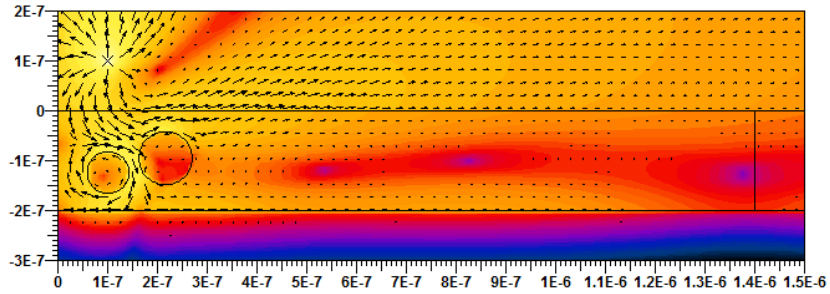

(b) Parameters obtained from Fig. 4.30(b) with the integration result of 13.53.

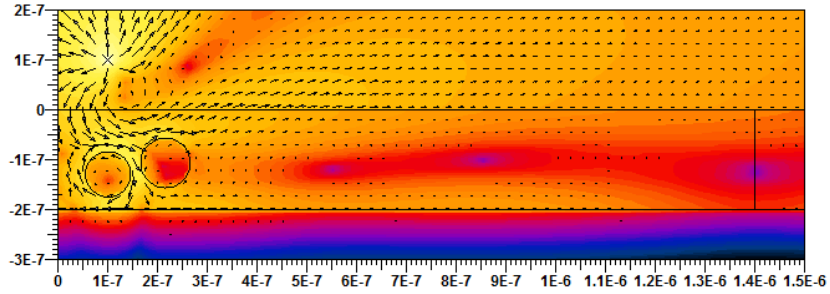

(c) Parameters obtained from Fig. 4.30(c) with the integration result of 12.54.

Figure 4.32: Field patterns of the optimized structures for the minimization problem. Surface: Magnitude of the time averaged Poynting vector, logarithmic scale and Arrows: direction of time averaged power flow. As a results of the optimization, the integral value drops down to 16.54%, 14.74% and 13.66% of the integration value calculated for the structure without the cylinders in Fig. 4.28.

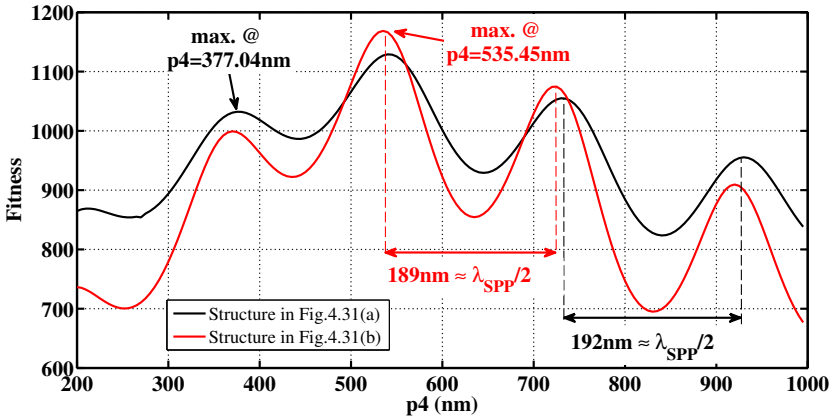

Figure 4.33: The effect of the distance between the two cylinders on the fitness value defined for the optimized structures in Fig. 4.31 (only p4 is varied for both of the cases). The two consecutive maxima (and minima) are separated by $\lambda_{SPP}/2$ as predicted. The maxima obtained for the structure in Fig. 4.32(a) is not global, since the bound for p4$\in \langle 20, 400 \rangle$nm do not cover the maxima at p4$\approx$ 540nm.

In the minimization problem, as shown in Fig. 4.32, the cylinders are used to block the Poynting vector from penetrating to the region on right. Even though the dimensions and the locations of the cylinders are comparable, it is not easy to calculate the optimized parameter values and narrower bounds for the optimization are always desired. Comparing the field profiles in Fig. 4.32 reveals that the minima point stays on the right and on the left of the integration line for the two structures obtained by large p4 bounds. In the case of narrower bounds for p1 and p4, the minima location is exactly at x=1400nm resulting in the minimum power flow, compared to the previous cases. As a result of the examples analyzed in this section, it is shown that the MMP with layered expansions can also be used in optimization problems, since it is possible to create efficient and robust models that can solve the corresponding problems in the given parameters ranges.

5 Conclusion

In this thesis, a numerical method for the analysis of nano structures built in layered media was introduced, by using layered media Green's functions as an expansion set in MMP. As a result, an efficient and robust numerical method is obtained, that can be used in the 2D and 3D scattering and eigenvalue analyses of nano structures in layered media.

The thesis starts with the description of the layered media Green's functions, i.e. the fields generated by an infinitesimal source in a given layered medium. In chapter 2, first, the Green's functions for free space was obtained in closed forms that can be easily obtained by a superposition of Hankel (for 2D) or complex exponential (for 1D and 3D) functions as listed in appendix A.1. Then it was shown that the closed form solutions for homogenous media can be also calculated by summing up all the plane wave contributions generated at the location of the source by using the Weyl identity. By using this technique, the layered media Green's functions were then obtained by the Sommerfeld integrals with infinite bounds (i.e. the plane waves with all possible wave vectors are summed up at the observation point, including the evanescent spectrum). All the integrand and integration rule definitions are provided in appendix A in order to provide all the mathematical tools needed to write a computer code for calculating layered media Green's functions. In section 2.4 the parameterized Sommerfeld integration path definitions were provided and tested in numerically demanding problems. As a final contribution of chapter 2, the complex origin Green's functions were introduced that can be used to decrease the number expansions needed for an MMP problem, and therefore decreasing the computational cost.

In chapter 3, a general discussion of MMP was carried out. The important aspects and pros and cons of the method, especially in the analysis of layered media, were discussed. The mathematical foundation of the method was also analyzed and the important aspects such as expansion/matching point distributions and the resulting MMP matrix equations for the scattering analysis in 2D and 3D were examined. In section 3.5, a 2D scattering problem example was solved by MMP where a step by step analysis was performed by using the open source simulation package OpenMaX 2013A. In section 3.6, the eigenvalue analysis of plasmonic waveguides built in layered media was introduced. In that analysis, the MMP search function was used to predict the approximate locations of the eigenvalues in a given complex plane, that can also be used with any other well known numerical method. The common difficulty of having a good initial guess (in the lack of MMP search function) for the eigenvalue

search was also addressed by comparing the results obtained by FEM (Comsol Multiphysics 4.3a and JCM Suite 2.6.3) and MMP. As a result of this analysis, it was shown that in the absence of a good initial guess, it is highly probable to end up with arbitrary number of non physical eigenvalues, especially in the plasmonic waveguide analysis in layered media.

In chapter 4, several numerical examples were analyzed to demonstrate the efficiency of the new method applied to different types of problems. In section 4.1, the results obtained by the two different versions of one of the most popular commercial software in market, COMSOL Multiphysics, were compared with the reference solutions obtained by MMP. As a result of the analysis it turns out that the previous version of COMSOL Multiphysics (ver. 4.2a) has critical inefficiencies in the PML implementation that is responsible for truncating the domain. Depending on the material properties of the structures, the errors around the PMLs are pronounced weaker or stronger that makes it even harder to predict if the solution is correct or not. As an example, in Fig. 5.1, it is clear from the field plot obtained from COMSOL Multiphysics ver. 4.2a that there is something wrong with the solution, mainly around the surface of the metallic substrate where strong field values are expected due to the SPP wave. But such an observation could not be made in all the different materials combinations for layers, as can also be observed in the comparison plots in Fig. 4.5 and 4.7, especially when all the layers were taken to be dielectric. Therefore, as the result of this analysis, one should be always careful when using domain truncation techniques like PML or ABC, since there is no direct analytical error measure available to check the accuracy of the results, as in MMP. In this chapter, another scattering analysis example followed where the complex origin layered expansions were used as an expansion set. By this example, it was shown that

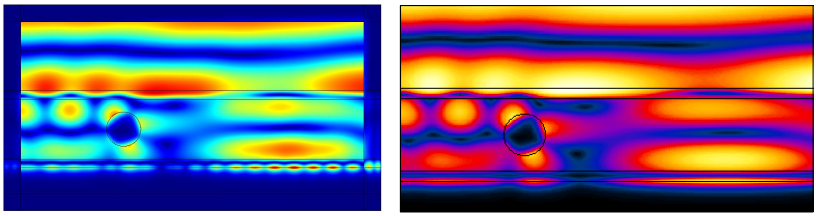

(a) Result obtained by COMSOL Multiphysics version 4.2a.

(b) Result obtained by OpenMaX 2013A.

Figure 5.1: Two different solutions obtained by different methods. The specifications of the geometry and the incident wave definitions are provided in Fig.4.2. In this example, the permittivity values of the layers and and scatterer are $\varepsilon_{scat} = \varepsilon_{r1} = -15.85 + 0.43i$ (Ag), $\varepsilon_{r2} = \varepsilon_{r4} = 9.0$, $\varepsilon_{r3} = 2.25$, $\varepsilon_{r5} = 1.00$ with $\lambda_0 = 600$nm.

the computational cost of problems can be reduced, given that a number of real origin expansions can be efficiently exchanged by a single complex origin expansion. In section 4.3 a scattering cross section calculation was carried out for a 3D particle in a layered medium. As a result of that analysis, it was shown that the material properties of the layers and the particle have a huge impact on the results, mainly due to the differences in the dispersive loss relations for different metals. In the next section, the eigenvalue analysis applied to several waveguide geometries built in layered geometries were introduced. It was shown that the MMP search function data provides a very important guideline for determining the exact locations of the eigenvalues, for different examples waveguide geometries. Finally in section 4.5 an optimization example was analyzed. In that example, it was shown that the new method can be used in cooperation with other numerical tools such as the evolutionary strategy optimizer module of OpenMaX 2013A. In addition, the resonance condition used in microwave devices such as transmission lines or Fabry Perot type resonators was validated in the nano structure analyzed in the last example.

As a continuation of the work presented here, an interesting research topic would be calculating the anisotropic layered media Green's functions and using them as an expansion set in MMP. The numerical tools provided in appendix A can be used with minor updates (mainly in the reflection/transmission coefficient data for different propagation directions of plane waves) in such an analysis as well. Another interesting subject that can be analyzed is the derivation of higher order layered expansions. As discussed in the thesis, it is possible to use higher order expansions in the MMP solution resulting in faster solutions. In the work presented here, only the monopole (in 2D) and dipole (in 3D) fields are derived and used in MMP and it would be interesting to analyze the effect of higher order expansions in the total MMP solution cost. Additionally, the eigenvalue analysis in 3D geometries would be a very interesting addition to the work presented in this thesis.

A Building up Green's functions in layered media

In this chapter, the layered media Green's functions and the integration rules for the field components are provided for the layered geometry shown in Fig. 2.2, excited by a time harmonic infinitesimal electric current[1] [58, 59, 45]. The fields generated by a magnetic current source can be obtained by simply applying the duality principle: $\varepsilon \to \mu$, $\mu \to \varepsilon$, $\mathbf{E} \to \mathbf{H}$, $\mathbf{H} \to -\mathbf{E}$, leading to the replacement of Il (electric current) $\to -j\omega\mu IA$, (magnetic current) where A is the area of the current loop modeling the magnetic dipole. Introducing these changes will change the polarization definitions of the waves generated, therefore in the discussion below the sub-super scripts TE and TM become TM and TE, respectively when calculating the Green's functions of magnetic infinitesimal sources.

As discussed in Chapter 2, the layered media Green's functions are obtained in two steps: 1) get the formula that describes the behavior of plane waves as they propagate in z direction, as a function of k_ρ (or equivalently $k_{zj} = \sqrt{k_j^2 - k_\rho^2}$) which are called the spectral domain Green's functions (A.3), and 2) multiply the spectral domain Green's functions by the accompanying plane (or cylindrical) waves that propagate in the lateral direction and perform the Sommerfeld Integration (A.4). Once this data is obtained the total Green's functions are given by:

$$G^{\mathbf{k},\mathbf{l}}_{X,YD,tot} = \delta_{i,j} G^{\mathbf{k},\mathbf{l}}_{X,YD,dir} + G^{\mathbf{k},\mathbf{l}}_{X,YD} \tag{A.1}$$

where $G^{\mathbf{k},\mathbf{l}}_{X,YD,tot}$ is the total, $\mathbf{k}$-component of the X-type spatial domain Green's function, generated by a l-directed infinitesimal source in Y dimensional layered media. The subscripts i and j are the source and observation layer numbers, and when they are the same, the direct wave contribution (App. A.1) should be summed up with the spatial domain Green's functions that gives the contribution of the up and down going waves in a given layer (App. A.4).

A.1 Contribution of the direct terms: Green's functions in homogenous unbounded media

In this section, the Green's functions for the fields in unbounded homogenous media are provided. Refer to 2.8 for the definitions of wave vector directions.

[1] $e^{j\omega t}$ time convention is used.

2D fields in homogenous medium

$$
\begin{aligned}
G^{\mathbf{x},\mathbf{y}}_{E,2D,dir}(x,z) &= -\frac{H_1^{(2)}(k_\kappa\rho)k_\gamma k_\kappa x}{4j\omega\rho\varepsilon_i} \\
G^{\mathbf{y},\mathbf{y}}_{E,2D,dir}(x,z) &= \frac{\omega H_0^{(2)}(k_\kappa\rho)}{4}\left(\mu_i - \frac{k_\gamma^2}{\omega^2\varepsilon_i}\right) \\
G^{\mathbf{z},\mathbf{y}}_{E,2D,dir}(x,z) &= -\frac{H_1^{(2)}(k_\kappa\rho)k_\gamma k_\kappa z}{4j\omega\rho\varepsilon_i} \\
G^{\mathbf{x},\mathbf{y}}_{H,2D,dir}(x,z) &= \frac{zk_\kappa}{4j\rho}H_1^{(2)}(k_\kappa\rho) \\
G^{\mathbf{y},\mathbf{y}}_{H,2D,dir}(x,z) &= 0 \\
G^{\mathbf{z},\mathbf{y}}_{H,2D,dir}(x,z) &= -\frac{xk_\kappa}{4j\rho}H_1^{(2)}(k_\kappa\rho)
\end{aligned}
\tag{A.2}
$$

3D fields in homogenous medium

$$
\begin{aligned}
G^{\mathbf{x},\mathbf{x}}_{E,3D,dir}(x,y,z) &= \frac{e^{-jk_ir}}{j\omega 4\pi\varepsilon_i r}\left(k_i^2 - \frac{jk_i}{r} - \frac{1+x^2k_i^2}{r^2} + \frac{3jk_ix^2}{r^3} + \frac{3x^2}{r^4}\right) \\
G^{\mathbf{y},\mathbf{x}}_{E,3D,dir}(x,y,z) &= \frac{xye^{-jk_ir}}{j\omega 4\pi\varepsilon_i r^3}\left(-k_i^2 + \frac{3jk_i}{r} + \frac{3}{r^2}\right) \\
G^{\mathbf{z},\mathbf{x}}_{E,3D,dir}(x,y,z) &= \frac{xze^{-jk_ir}}{j\omega 4\pi\varepsilon_i r^3}\left(-k_i^2 + \frac{3jk_i}{r} + \frac{3}{r^2}\right) \\
G^{\mathbf{x},\mathbf{z}}_{E,3D,dir}(x,y,z) &= G^{z,x}_{E,3D,dir} \\
G^{\mathbf{y},\mathbf{z}}_{E,3D,dir}(x,y,z) &= \frac{zye^{-jk_ir}}{j\omega 4\pi\varepsilon_i r^3}\left(-k_i^2 + \frac{3jk_i}{r} + \frac{3}{r^2}\right) \\
G^{\mathbf{z},\mathbf{z}}_{E,3D,dir}(x,y,z) &= \frac{e^{-jk_ir}}{j\omega 4\pi\varepsilon_i r}\left(k_i^2 - \frac{jk_i}{r} - \frac{1+z^2k_i^2}{r^2} + \frac{3jk_iz^2}{r^3} + \frac{3z^2}{r^4}\right) \\
G^{\mathbf{x},\mathbf{x}}_{H,3D,dir}(x,y,z) &= 0 \\
G^{\mathbf{y},\mathbf{x}}_{H,3D,dir}(x,y,z) &= -\frac{ze^{-jk_ir}}{4\pi r}\left(\frac{jk_i}{r} + \frac{1}{r^2}\right) \\
G^{\mathbf{z},\mathbf{x}}_{H,3D,dir}(x,y,z) &= \frac{ye^{-jk_ir}}{4\pi r}\left(\frac{jk_i}{r} + \frac{1}{r^2}\right) \\
G^{\mathbf{x},\mathbf{z}}_{H,3D,dir}(x,y,z) &= -\frac{ye^{-jk_ir}}{4\pi r}\left(\frac{jk_i}{r} + \frac{1}{r^2}\right) \\
G^{\mathbf{y},\mathbf{z}}_{H,3D,dir}(x,y,z) &= \frac{xe^{-jk_ir}}{4\pi r}\left(\frac{jk_i}{r} + \frac{1}{r^2}\right) \\
G^{\mathbf{z},\mathbf{z}}_{H,3D,dir}(x,y,z) &= 0
\end{aligned}
\tag{A.3}
$$

A.2 Reflection/Transmission coefficients and amplitude transfer function

In this section, the most important numerical tools for the calculation of spectral domain Green's functions, i.e. the generalized reflection/transmission coefficients and the amplitude transfer function definitions, are provided. Before starting with the discussion, the definitions of the wave vector components should be provided. In a given layer m, the following holds:

$$\begin{aligned} k_m = & \frac{\omega}{c_0\sqrt{\varepsilon_{rm}\mu_{rm}}} \\ = & \sqrt{k_x^2+k_y^2+k_{zm}^2} = \sqrt{k_\rho^2+k_{zm}^2} \quad \text{in 3D} \\ = & \sqrt{k_\gamma^2+k_\kappa^2} = \sqrt{k_\gamma^2+k_x^2+k_{zm}^2} \quad \text{in 2D} \end{aligned} \tag{A.4}$$

where $\Im(k_m) \leq 0$ due to the causality principle for lossy and lossless (non-active) materials [89]. When building up the spectral domain Green's functions, k_m, k_x, k_y, k_γ are fixed values, i.e. given as a constant by the user (k_γ) or used as the integration variable (k_x,k_y) or obtained by the material properties of the given layered geometry (k_m). Therefore, k_{zm} becomes the main variable of the spectral analysis, where the branch of the square roots are chosen in such a way so that:

$$\Im(k_{zm}) \leq 0 \tag{A.5}$$

to guarantee the correct Reimann sheet choice [58].

In a multilayered medium, the reflection coefficient is obtained in an iterative fashion, starting from the top or bottom interface. The reflection coefficient defined at the interface (from layer 2 to 1) of a two layered medium (also called the Fresnel reflection coefficient) is:

$$R_{TE}^{2,1} = \frac{\mu_1 k_{z2} - \mu_2 k_{z1}}{\mu_1 k_{z2} + \mu_2 k_{z1}} \tag{A.6}$$

In a three layered medium, the reflection coefficient defined at the interface between layers 3 and 2 (from layer 3 to 2) is obtained by carrying the Fresnel reflection coefficient to the interface between layers 3 and 2 and introducing effect of layer 3, which results in:

$$\tilde{R}_{TE}^{3,2} = \frac{R_{TE}^{3,2} + R_{TE}^{2,1} e^{-jk_{z2}2d_2}}{1 - R_{TE}^{2,3} R_{TE}^{2,1} e^{-jk_{z2}2d_2}} \tag{A.7}$$

Following the same technique, the generalized reflection coefficient in an N layered medium is obtained iteratively by:

$$\tilde{R}_{TE}^{m+1,m} = \frac{R_{TE}^{m+1,m} + \tilde{R}_{TE}^{m,m-1} e^{-jk_{zm}2d_m}}{1 - R_{TE}^{m,m+1} \tilde{R}_{TE}^{m,m-1} e^{-jk_{zm}2d_m}} \tag{A.8}$$

In (A.7) and (A.8), $\tilde{}$ is used to denote the generalized reflection coefficients, as opposed to Fresnel reflection coefficient in (A.6). It should be also noted that the reflection coefficients are defined only at a given boundary and do not include the information of the plane wave propagating from the source layer to the observation layer. In order to obtain this information, the amplitude transfer function for a given layer m is defined, again in an iterative fashion but this time starting from the source layer i, as follows:

$$\begin{aligned} A_m^{TE} &= 1 && \text{if } m = i \\ A_m^{TE} &= A_{m+1}^{TE} \frac{T_{TE}^{m+1,m} e^{-j(k_{z(m+1)} - k_{zm})(h + z_{i,m})}}{1 - R_{TE}^{m,m+1} \tilde{R}_{TE}^{m,m-1} e^{-jk_{zm} 2d_m}} && \text{if } m < i \\ A_m^{TE} &= A_{m-1}^{TE} \frac{T_{TE}^{m-1,m} e^{-j(k_{z(m-1)} - k_{zm})(z_{i,m} + d_i - h)}}{1 - R_{TE}^{m,m-1} \tilde{R}_{TE}^{m,m+1} e^{-jk_{zm} 2d_m}} && \text{if } m > i \end{aligned} \quad \text{(A.9)}$$

where the transmission coefficient is defined as:

$$T = 1 + R \tag{A.10}$$

The constant $z_{i,m}$ is the sum of the layer thickness values between the layers i and m defined as follows:

$$z_{i,m} = \left(\sum_{N=i}^{m} d_N \right) - d_i - d_m \tag{A.11}$$

A.3 Spectral domain Green's functions for layered media

Depending on the locations of the source $(0, 0, 0)$ and observation points (x, y, z), the spectral domain Green's functions $\tilde{G}$ take different forms when: 1) the source and observation points are in the same layer i, 2) the source layer i is above the observation layer j and 3) the source layer i is below the observation layer j. It should be reminded that the direct wave term is not included in the functions in section A.3.1, since their contribution can be obtained in closed form (i.e. the fields generated by a point source in homogenous space) as provided in section A.1.

A.3.1 The source and observation points are in the same layer

$$
\begin{aligned}
\tilde{G}_1(k_\rho, z) &= \mu_i \frac{A_{11}^{hor} e^{jk_{zi}z} + A_{13}^{hor} e^{-jk_{zi}z}}{2jk_{zi}} \\
\tilde{G}_2(k_\rho, z) &= \frac{\left(k_i^2 A_{11}^{hor} + k_{zi}^2 A_{12}^{hor}\right) e^{jk_{zi}z} + \left(k_i^2 A_{13}^{hor} - k_{zi}^2 A_{14}^{hor}\right) e^{-jk_{zi}z}}{2\varepsilon_i jk_{zi}k_\rho^2} \\
\tilde{G}_3(k_\rho, z) &= -\mu_i \frac{\left(A_{11}^{hor} + A_{12}^{hor}\right) e^{jk_{zi}z} + \left(A_{14}^{hor} - A_{13}^{hor}\right) e^{-jk_{zi}z}}{2k_\rho^2} \\
\tilde{G}_4(k_\rho, z) &= \frac{\left(k_i^2 A_{11}^{hor} + k_{zi}^2 A_{12}^{hor}\right) e^{jk_{zi}z} - \left(k_i^2 A_{13}^{hor} - k_{zi}^2 A_{14}^{hor}\right) e^{-jk_{zi}z}}{2\varepsilon_i k_\rho^2} \\
\tilde{G}_5(k_\rho, z) &= \mu_i \frac{A_{11}^{hor} e^{jk_{zi}z} - A_{13}^{hor} e^{-jk_{zi}z}}{2} \\
\tilde{G}_6(k_\rho, z) &= \frac{1}{2\varepsilon_i}\left(A_{11}^{ver} e^{jk_{zi}z} - A_{12}^{ver} e^{-jk_{zi}z}\right) \\
\tilde{G}_7(k_\rho, z) &= \mu_i \frac{A_{11}^{ver} e^{jk_{zi}z} + A_{12}^{ver} e^{-jk_{zi}z}}{2jk_{zi}} \\
\tilde{G}_8(k_\rho, z) &= \frac{1}{2\varepsilon_i} jk_{zi}\left(A_{11}^{ver} e^{jk_{zi}z} + A_{12}^{ver} e^{-jk_{zi}z}\right)
\end{aligned}
\tag{A.12}
$$

where

$$
\begin{aligned}
A_{11}^{hor} &= \tilde{R}_{TE}^{i,i+1} e^{-jk_{zi}(d_i-h)}\left(e^{-jk_{zi}(d_i-h)} + \tilde{R}_{TE}^{i,i-1} e^{-jk_{zi}(d_i+h)}\right) M_i^{TE} \\
A_{12}^{hor} &= \tilde{R}_{TM}^{i,i+1} e^{-jk_{zi}(d_i-h)}\left(e^{-jk_{zi}(d_i-h)} - \tilde{R}_{TM}^{i,i-1} e^{-jk_{zi}(d_i+h)}\right) M_i^{TM} \\
A_{13}^{hor} &= \tilde{R}_{TE}^{i,i-1} e^{-jk_{zi}h}\left(e^{-jk_{zi}h} + \tilde{R}_{TE}^{i,i+1} e^{-jk_{zi}(2d_i-h)}\right) M_i^{TE} \\
A_{14}^{hor} &= \tilde{R}_{TM}^{i,i-1} e^{-jk_{zi}h}\left(-e^{-jk_{zi}h} + \tilde{R}_{TM}^{i,i+1} e^{-jk_{zi}(2d_i-h)}\right) M_i^{TM} \\
A_{11}^{ver} &= \tilde{R}_{TM}^{i,i+1} e^{-jk_{zi}(d_i-h)}\left(e^{-jk_{zi}(d_i-h)} + \tilde{R}_{TM}^{i,i-1} e^{-jk_{zi}(d_i+h)}\right) M_i^{TM} \\
A_{12}^{ver} &= \tilde{R}_{TM}^{i,i-1} e^{-jk_{zi}h}\left(e^{-jk_{zi}h} + \tilde{R}_{TM}^{i,i+1} e^{-jk_{zi}(2d_i-h)}\right) M_i^{TM} \\
M_i^{TE} &= \frac{1}{1 - \tilde{R}_{TE}^{i,i-1}\tilde{R}_{TE}^{i,i+1} e^{-jk_{zi}2d_i}} \\
M_i^{TM} &= \frac{1}{1 - \tilde{R}_{TM}^{i,i-1}\tilde{R}_{TM}^{i,i+1} e^{-jk_{zi}2d_i}}
\end{aligned}
\tag{A.13}
$$

A.3.2 The source layer is above the observation layer

$$
\begin{aligned}
\tilde{G}_1(k_\rho,z) &= \mu_i \frac{A_j^{TE} A_{21}^{hor}\left(e^{jk_{zj}z} + \tilde{R}_{TE}^{j,j-1} P_2 e^{-jk_{zj}z}\right)}{2jk_{zi}} \\
\tilde{G}_2(k_\rho,z) &= -\frac{A_{23}^{hor} e^{jk_{zj}z} + A_{24}^{hor} e^{-jk_{zj}z}}{2\varepsilon_j jk_{zi}k_\rho^2} \\
\tilde{G}_3(k_\rho,z) &= \mu_j \frac{A_{25}^{hor} e^{jk_{zj}z} + A_{26}^{hor} e^{-jk_{zj}z}}{2jk_\rho^2} \\
\tilde{G}_4(k_\rho,z) &= -\frac{k_{zj}\left(A_{23}^{hor} e^{jk_{zj}z} - A_{24}^{hor} e^{-jk_{zj}z}\right)}{2\varepsilon_j k_{z_i} k_\rho^2} \\
\tilde{G}_5(k_\rho,z) &= \mu_i \frac{A_j^{TE} A_{21}^{hor} k_{zj}\left(e^{jk_{zj}z} - \tilde{R}_{TE}^{j,j-1} P_2 e^{-jk_{zj}z}\right)}{2k_{zi}} \\
\tilde{G}_6(k_\rho,z) &= \frac{-\left(A_{21}^{ver} + A_{22}^{ver}\right) e^{jk_{zj}h}\left(e^{jk_{zj}z} - \tilde{R}_{TM}^{j,j-1} P_2 e^{-jk_{zj}z}\right)}{2\varepsilon_j k_{zi}} \\
\tilde{G}_7(k_\rho,z) &= \mu_j \frac{A_j^{TM}\left(1 + A_{23}^{ver}\right)\left(e^{jk_{zj}z} + \tilde{R}_{TM}^{j,j-1} P_2 e^{-jk_{zj}z}\right)}{2jk_{zi}} \\
\tilde{G}_8(k_\rho,z) &= \frac{-\left(A_{21}^{ver} + A_{22}^{ver}\right) e^{jk_{zj}h} jk_{zj}\left(e^{jk_{zj}z} + \tilde{R}_{TM}^{j,j-1} P_2 e^{-jk_{zj}z}\right)}{2\varepsilon_j k_{zi}}
\end{aligned}
\tag{A.14}
$$

where

$$
\begin{aligned}
A_{21}^{hor} &= \left(1 + \tilde{R}_{TE}^{i,i+1} e^{-jk_{zi}2(d_i-h)}\right) M_i^{TE} \\
A_{22}^{hor} &= \left(-1 + \tilde{R}_{TM}^{i,i+1} e^{-jk_{zi}2(d_i-h)}\right) M_i^{TM} \\
A_{23}^{hor} &= -A_j^{TM} A_{22}^{hor} k_{zi} k_{zj} - (\mu_{ri}/\mu_{rj}) A_j^{TE} A_{21}^{hor} k_j^2 \\
A_{24}^{hor} &= \left(A_j^{TM} A_{22}^{hor} \tilde{R}_{TM}^{j,j-1} k_{zi} k_{zj} - (\mu_{ri}/\mu_{rj}) A_j^{TE} A_{21}^{hor} \tilde{R}_{TE}^{j,j-1} k_j^2\right) P_2 \\
A_{25}^{hor} &= -(\mu_{ri}/\mu_{rj}) A_j^{TE} A_{21}^{hor} k_{zj}/k_{zi} - A_j^{TM} A_{22}^{hor} \\
A_{26}^{hor} &= \left((\mu_{ri}/\mu_{rj}) A_j^{TE} A_{21}^{hor} \tilde{R}_{TE}^{j,j-1} k_{zj}/k_{zi} - A_j^{TM} A_{22}^{hor} \tilde{R}_{TM}^{j,j-1}\right) P_2 \\
A_{21}^{ver} &= -A_j^{TM}\left(1 + \tilde{R}_{TM}^{i,i-1} \tilde{R}_{TM}^{i,i+1} e^{-jk_{zi}2d_i} M_i^{TM}\right) k_{zj} e^{-jk_{zj}h} \\
A_{22}^{ver} &= -A_j^{TM} \tilde{R}_{TM}^{i,i+1} k_{zj} e^{jk_{zi}2(h-d_i)} e^{-jk_{zj}h} M_i^{TM} \\
A_{23}^{ver} &= \tilde{R}_{TM}^{i,i+1} e^{-jk_{zi}(d_i-h)}\left(e^{-jk_{zi}(d_i-h)} + \tilde{R}_{TM}^{i,i-1} e^{-jk_{zi}(d_i+h)}\right) M_i^{TM} \\
P_2 &= e^{-jk_{zj}2(z_m+h)}
\end{aligned}
\tag{A.15}
$$

A.3.3 The source layer is below the observation layer

$$
\begin{aligned}
\tilde{G}_1(k_\rho,z) &= \mu_i \frac{A_j^{TE}A_{31}^{hor}\left(e^{-jk_{zj}z}+\tilde{R}_{TE}^{j,j+1}P_3e^{jk_{zj}z}\right)}{2jk_{zi}}\\
\tilde{G}_2(k_\rho,z) &= -\frac{A_{33}^{hor}e^{-jk_{zj}z}+A_{34}^{hor}e^{jk_{zj}z}}{2\varepsilon_j jk_{zi}k_\rho^2}\\
\tilde{G}_3(k_\rho,z) &= \mu_j \frac{A_{35}^{hor}e^{-jk_{zj}z}+A_{36}^{hor}e^{jk_{zj}z}}{2k_\rho^2}\\
\tilde{G}_4(k_\rho,z) &= -\frac{k_{zj}\left(A_{33}^{hor}e^{-jk_{zj}z}-A_{34}^{hor}e^{jk_{zj}z}\right)}{2\varepsilon_j k_{zi}k_\rho^2}\\
\tilde{G}_5(k_\rho,z) &= \mu_i \frac{A_j^{TE}A_{31}^{hor}k_{zj}\left(-e^{-jk_{zj}z}+\tilde{R}_{TE}^{j,j+1}P_3e^{jk_{zj}z}\right)}{2k_{zi}}\\
\tilde{G}_6(k_\rho,z) &= \frac{-\left(A_{31}^{ver}+A_{32}^{ver}\right)e^{-jk_{zj}h}(e^{-jk_{zj}z}-\tilde{R}_{TM}^{j,j+1}P_3e^{jk_{zj}z})}{2\varepsilon_j k_{zi}}\\
\tilde{G}_7(k_\rho,z) &= \mu_j \frac{A_j^{TM}\left(1+A_{33}^{ver}\right)\left(e^{-jk_{zj}z}+\tilde{R}_{TM}^{j,j+1}P_3e^{jk_{zj}z}\right)}{2jk_{zi}}\\
\tilde{G}_8(k_\rho,z) &= \frac{-\left(A_{31}^{ver}+A_{32}^{ver}\right)e^{-jk_{zj}h}jk_{zj}\left(-e^{-jk_{zj}z}-\tilde{R}_{TM}^{j,j+1}P_3e^{jk_{zj}z}\right)}{2\varepsilon_j k_{zi}}
\end{aligned}
\tag{A.16}
$$

where

$$
\begin{aligned}
A_{31}^{hor} &= \left(1+\tilde{R}_{TE}^{i,i-1}e^{-jk_{zi}2h}\right)M_i^{TE}\\
A_{32}^{hor} &= \left(1-\tilde{R}_{TM}^{i,i-1}e^{-jk_{zi}2h}\right)M_i^{TM}\\
A_{33}^{hor} &= A_j^{TM}A_{32}^{hor}k_{zi}k_{zj}-(\mu_{ri}/\mu_{rj})A_j^{TE}A_{31}^{hor}k_j^2\\
A_{34}^{hor} &= \left(-A_j^{TM}A_{32}^{hor}\tilde{R}_{TM}^{j,j+1}k_{zi}k_{zj}-(\mu_{ri}/\mu_{rj})A_j^{TE}A_{31}^{hor}\tilde{R}_{TE}^{j,j+1}k_j^2\right)P_3\\
A_{35}^{hor} &= (\mu_{ri}/\mu_{rj})A_j^{TE}A_{31}^{hor}k_{zj}/k_{zi}-A_j^{TM}A_{32}^{hor}\\
A_{36}^{hor} &= \left(-(\mu_{ri}/\mu_{rj})A_j^{TE}A_{31}^{hor}\tilde{R}_{TE}^{j,j+1}k_{zj}/k_{zi}-A_j^{TM}A_{32}^{hor}\tilde{R}_{TM}^{j,j+1}\right)P_3\\
A_{31}^{ver} &= A_j^{TM}\left(1+\tilde{R}_{TM}^{i,i-1}\tilde{R}_{TM}^{i,i+1}e^{-jk_{zi}2d_i}M_i^{TM}\right)k_{zj}e^{jk_{zj}h}\\
A_{32}^{ver} &= A_j^{TM}\tilde{R}_{TM}^{i,i-1}k_{zj}e^{j(k_{zj}-2k_{zi})h}M_i^{TM}\\
A_{33}^{ver} &= \tilde{R}_{TM}^{i,i-1}e^{-jk_{zi}h}\left(e^{-jk_{zi}h}+\tilde{R}_{TM}^{i,i+1}e^{-jk_{zi}(2d_i-h)}\right)M_i^{TM}\\
P_3 &= e^{-jk_{zj}2(z_m+d_i-h)}
\end{aligned}
\tag{A.17}
$$

A.4 Spatial Domain Green's Functions for layered media

In this section, the spatial domain Green's functions for fields are provided for 2 and 3 dimensional geometries. This is done by combining the spectral domain Green's functions in section A.3 with the appropriate wave natures in the lateral direction and integrating the resulting formulae by the definitions provided here.

Integration definitions for 2D geometries

In 2D, $k_\rho = k_x$ is used for the spectral domain Green's functions defined in A.3, since the only lateral direction in 2D is x. Note that if $k_\gamma = 0$, the line sources will only produce in-plane waves (i.e. $G^{y,y}_{E,2D} \neq 0$, $G^{x,y}_{H,2D} \neq 0$ and $G^{z,y}_{H,2D} \neq 0$), when $k_\gamma \neq 0$ all the field components are coupled and become nonzero, according to the formulae provided below.

$$\begin{aligned}
G^{\mathbf{x},\mathbf{y}}_{E,2D}(x,z) &= \frac{k_\gamma}{\omega} S_1^{2D}\left\{\tilde{G}_2(k_x,z)\right\} \\
G^{\mathbf{y},\mathbf{y}}_{E,2D}(x,z) &= j\omega S_0^{2D}\left\{\tilde{G}_1(k_x,z)\right\} + \frac{k_\gamma^2}{j\omega} S_0^{2D}\left\{\tilde{G}_2(k_x,z)\right\} \\
G^{\mathbf{z},\mathbf{y}}_{E,2D}(x,z) &= \omega k_\gamma S_0^{2D}\left\{\tilde{G}_3(k_x,z)\right\} + \frac{k_\gamma}{\omega} S_0^{2D}\left\{\tilde{G}_4(k_x,z)\right\} \\
G^{\mathbf{x},\mathbf{y}}_{H,2D}(x,z) &= -\frac{1}{\mu_j}\left(S_0^{2D}\left\{\tilde{G}_5(k_x,z)\right\} - k_\gamma^2 S_0^{2D}\left\{\tilde{G}_3(k_x,z)\right\}\right) \\
G^{\mathbf{y},\mathbf{y}}_{H,2D}(x,z) &= \frac{jk_\gamma}{\mu_j} S_1^{2D}\left\{\tilde{G}_3(k_x,z)\right\} \\
G^{\mathbf{z},\mathbf{y}}_{H,2D}(x,z) &= \frac{1}{\mu_j} S_1^{2D}\left\{\tilde{G}_1(k_x,z)\right\}
\end{aligned} \tag{A.18}$$

with the following integration definitions:

$$\begin{aligned}
S_0^{2D}\left\{f(k_x)\right\} &= \frac{1}{2\pi}\int_{-\infty}^{\infty} f(k_x) e^{-jk_x x} dk_x \\
S_1^{2D}\left\{f(k_x)\right\} &= \frac{1}{2\pi}\int_{-\infty}^{\infty} -jk_x f(k_x) e^{-jk_x x} dk_x
\end{aligned} \tag{A.19}$$

Integration definitions for 3D geometries

In 3D, $k_\rho^2 = k_x^2 + k_y^2$ and $\rho = x^2 + y^2$ are used, since the lateral direction lies on the XY plane.

$$\begin{aligned}
G_{E,3D}^{\mathbf{x},\mathbf{x}}(x,y,z) &= -j\omega S_0^{3D}\left\{\tilde{G}_1(k_\rho,z)\right\} + \frac{1}{j\omega}S_2^{3D}\left\{\tilde{G}_2(k_\rho,z)\right\} \\
G_{E,3D}^{\mathbf{y},\mathbf{x}}(x,y,z) &= \frac{1}{j\omega}S_3^{3D}\left\{\tilde{G}_2(k_\rho,z)\right\} \\
G_{E,3D}^{\mathbf{z},\mathbf{x}}(x,y,z) &= -j\omega x S_1^{3D}\left\{\tilde{G}_5(k_\rho,z)\right\} + \frac{x}{j\omega}S_1^{3D}\left\{\tilde{G}_4(k_\rho,z)\right\} \\
G_{E,3D}^{\mathbf{x},\mathbf{z}}(x,y,z) &= \frac{x}{j\omega}S_1^{3D}\left\{\tilde{G}_6(k_\rho,z)\right\} \\
G_{E,3D}^{\mathbf{y},\mathbf{z}}(x,y,z) &= \frac{y}{j\omega}S_1^{3D}\left\{\tilde{G}_6(k_\rho,z)\right\} \\
G_{E,3D}^{\mathbf{z},\mathbf{z}}(x,y,z) &= -j\omega S_0^{3D}\left\{\tilde{G}_7(k_\rho,z)\right\} + \frac{1}{j\omega}S_0^{3D}\left\{\tilde{G}_8(k_\rho,z)\right\} \\
G_{H,3D}^{\mathbf{x},\mathbf{x}}(x,y,z) &= \frac{1}{\mu_j}S_3^{3D}\left\{\tilde{G}_3(k_\rho,z)\right\} \\
G_{H,3D}^{\mathbf{y},\mathbf{x}}(x,y,z) &= \frac{1}{\mu_j}\left(S_0^{3D}\left\{\tilde{G}_5(k_\rho,z)\right\} - S_2^{3D}\left\{\tilde{G}_3(k_\rho,z)\right\}\right) \\
G_{H,3D}^{\mathbf{z},\mathbf{x}}(x,y,z) &= -\frac{y}{\mu_j}S_1^{3D}\left\{\tilde{G}_1(k_x,z)\right\} \\
G_{H,3D}^{\mathbf{x},\mathbf{z}}(x,y,z) &= \frac{y}{\mu_j}S_1^{3D}\left\{\tilde{G}_7(k_\rho,z)\right\} \\
G_{H,3D}^{\mathbf{y},\mathbf{z}}(x,y,z) &= -\frac{x}{\mu_j}S_1^{3D}\left\{\tilde{G}_7(k_\rho,z)\right\} \\
G_{H,3D}^{\mathbf{z},\mathbf{z}}(x,y,z) &= 0
\end{aligned} \tag{A.20}$$

with the following integration definitions:

$$\begin{aligned}
S_0^{3D}\left\{f(k_\rho)\right\} &= \frac{1}{4\pi}\int_{-\infty}^{\infty} f(k_\rho)H_0^{(2)}(k_\rho\rho)k_\rho dk_\rho \\
S_1^{3D}\left\{f(k_\rho)\right\} &= -\frac{1}{4\pi}\int_{-\infty}^{\infty} f(k_\rho)\frac{k_\rho H_1^{(2)}(k_\rho\rho)}{\rho}k_\rho dk_\rho \\
S_2^{3D}\left\{f(k_\rho)\right\} &= \frac{1}{4\pi}\int_{-\infty}^{\infty} f(k_\rho)\left(\frac{2k_\rho x^2 H_1^{(2)}(k_\rho\rho)}{\rho^3} - \frac{k_\rho^2 x^2 H_0^{(2)}(k_\rho\rho)}{\rho^2}\cdots\right. \\
&\quad \left.\cdots - \frac{k_\rho H_1^{(2)}(k_\rho\rho)}{\rho}\right)k_\rho dk_\rho \\
S_3^{3D}\left\{f(k_\rho)\right\} &= \frac{1}{4\pi}\int_{-\infty}^{\infty} f(k_\rho)\left(\frac{2k_\rho xy H_1^{(2)}(k_\rho\rho)}{\rho^3} - \frac{k_\rho^2 xy H_0^{(2)}(k_\rho\rho)}{\rho^2}\right)k_\rho dk_\rho
\end{aligned} \tag{A.21}$$

Bibliography

[1] K. Iizuka, "History of optics," in *Engineering Optics*, Ser. Springer Series in Optical Sciences. Springer Berlin Heidelberg, 1987, Vol. 35, pp. 1–26. [Online]. Available: http://dx.doi.org/10.1007/978-3-540-36808-3_1

[2] O. Darrigol, *A history of optics from Greek antiquity to the nineteenth century.* OUP Oxford, 2012. [Online]. Available: http://ukcatalogue.oup.com/product/9780199644377.do#.UcB4hZyO7Pp

[3] M. I. Stockman, "Nanoplasmonics: The physics behind the applications," *Physics Today*, Vol. 64, No. 2, pp. 39–44, 2011. [Online]. Available: http://link.aip.org/link/?PTO/64/39/1

[4] A. Zayats, "Perspective: A glint of the future," *Nature*, Vol. 495, No. 7440, 2013. [Online]. Available: http://dx.doi.org/10.1038/495S7a

[5] M. Faraday, "Experimental relations of gold (and other matals) to light," *Phil. Trans. R. Soc. Lond.*, Vol. 147, pp. 145–181, 1857. [Online]. Available: http://www.jstor.org/stable/108616

[6] G. Mie, "Elektrische wellen an zwei parallelen drähten," *Annalen der Physik*, Vol. 307, No. 6, pp. 201–249, 1900. [Online]. Available: http://onlinelibrary.wiley.com/doi/10.1002/andp.19003070602/abstract

[7] D. Kaklamani and H. Anastassiu, "Aspects of the method of auxiliary sources (MAS) in computational electromagnetics," *Antennas and Propagation Magazine, IEEE*, Vol. 44, No. 3, pp. 48–64, 2002. [Online]. Available: http://dx.doi.org/10.1109/MAP.2002.1028734

[8] C. Hafner, *Post-Modern Electromagnetics: Using Intelligent Maxwell Solvers.* John Wiley and Sons, 1999.

[9] J. Z. Buchwald, *The creation of scientific effect: Heinrich Hertz.* The University of Chicago Press, 1994. [Online]. Available: http://press.uchicago.edu/ucp/books/book/chicago/C/bo3636276.html

[10] T. Sarkar and D. L. Sengupta, "An appreciation of J.C. Bose's pioneering work in millimeter waves," *Antennas and Propagation Magazine, IEEE*, Vol. 39, No. 5, pp. 55–62, 1997. [Online]. Available: http://ieeexplore.ieee.org/xpl/articleDetails.jsp?reload=true&arnumber=637106

[11] F. Braun, "Wireless electric transmission of signals over surfaces," USA Patent US 750 429, Jan. 26, 1904. [Online]. Available: http://www.google.com/patents/US750429

[12] G. Marconi, "Wireless telegraphy," *Electrical Engineers, Journal of the Institution of*, Vol. 28, No. 139, pp. 273–290, 1899. [Online]. Available: http://ieeexplore.ieee.org/xpls/abs_all.jsp?arnumber=5309193

[13] J. Kraus, "Antennas since Hertz and Marconi," *Antennas and Propagation, IEEE Transactions on*, Vol. 33, No. 2, pp. 131–137, 1985. [Online]. Available: http://dx.doi.org/10.1109/TAP.1985.1143550

[14] R. E. Colin, "Hertzian dipole radiating over a lossy earth or sea: Some early and late 20th-century controversies," *Antennas and Propagation Magazine, IEEE*, Vol. 46, No. 2, pp. 64–79, Apr. 2004. [Online]. Available: http://dx.doi.org/10.1109/MAP.2004.1305535

[15] J. Zenneck, "Über die fortpflanzung ebener elektromagnetischer wellen längs einer ebenen leiterfläche und ihre beziehung zur drahtlosen telegraphie," *Annalen der Physik*, Vol. 328, No. 10, pp. 846–866, 1907. [Online]. Available: http://dx.doi.org/10.1002/andp.19073281003

[16] A. Sommerfeld, "Über die ausbreitung der wellen in der drahtlosen telegraphie," *Annalen der Physik*, Vol. 333, No. 4, pp. 665–736, 1909. [Online]. Available: http://onlinelibrary.wiley.com/doi/10.1002/andp.19093330402/abstract

[17] H. Weyl, "Ausbreitung elektromagnetischer wellen ber einem ebenen leiter," *Annalen der Physik*, Vol. 365, No. 21, pp. 481–500, 1919. [Online]. Available: http://onlinelibrary.wiley.com/doi/10.1002/andp.19193652104/abstract

[18] A. V. Oppenheim, A. S. Willsky, and S. H. Nawab, *Signals & systems (2nd ed.)*. Upper Saddle River, NJ, USA: Prentice-Hall, Inc., 1996.

[19] R. F. Harrington, *Field Computation by Moment Methods*. Florida: Robert E. Krieger Publishing Company, 1982.

[20] J. R. Mosig, "Arbitrarily shaped microstrip structures and their analysis with a mixed potential integral equation," *Microwave Theory and Techniques, IEEE Transactions on*, Vol. 36, No. 2, pp. 314–323, Feb 1988. [Online]. Available: http://dx.doi.org/10.1109/22.3520

[21] K. A. Michalski and D. Zheng, "Electromagnetic scattering and radiation by surfaces of arbitrary shape in layered media: I. theory," *Antennas and Propagation, IEEE Transactions on*, Vol. 38, No. 3, pp. 335–344, Mar 1990. [Online]. Available: http://dx.doi.org/10.1109/8.52240

[22] L. Alatan, M. I. Aksun, K. Mahadevan, and T. Birand, "Analytical evaluation of the mom matrix elements," *Microwave Theory and Techniques, IEEE Transactions on*, Vol. 44, No. 4, pp. 519–525, Apr 1996. [Online]. Available: http://dx.doi.org/10.1109/22.491019

[23] N. Kinayman, "A novel CAD algorithm for the analysis of printed circuits," PhD. thesis, Bilkent University, 1997.

[24] M. J. Tsai, F. D. Flavis, O. Fordharn, and N. G. Alexopoulos, "Modeling planar arbitrarily shaped microstrip elements in multilayered media," *Microwave Theory and Techniques, IEEE Transactions on*, Vol. 45, No. 3, pp. 330–337, Mar 1997. [Online]. Available: http://dx.doi.org/10.1109/22.563330

[25] J. D. Joannopoulos, P. R. Villeneuve, and S. Fan, "Photonic crystals," *Solid State Communications*, Vol. 102, No. 2-3, pp. 165–173, 1997, highlights in Condensed Matter Physics and Materials Science. [Online]. Available: http://www.sciencedirect.com/science/article/B6TVW-3SP68WM-7H/2/36c7658507bdbbc4a692dd9c0445f406

[26] S. G. Johnson, S. Fan, P. R. Villeneuve, J. D. Joannopoulos, and L. A. Kolodziejski, "Guided modes in photonic crystal slabs," *Phys. Rev. B*, Vol. 60, No. 8, pp. 5751–5758, Aug 1999. [Online]. Available: http://link.aps.org/doi/10.1103/PhysRevB.60.5751

[27] N. Vasilantonakis, K. Terzaki, I. Sakellari, V. Purlys, D. Gray, C. M. Soukoulis, M. Vamvakaki, M. Kafesaki, and M. Farsari, "Three-dimensional metallic photonic crystals with optical bandgaps," *Advanced Materials*, Vol. 24, No. 8, pp. 1101–1105, 2012. [Online]. Available: http://dx.doi.org/10.1002/adma.201104778

[28] M. A. Green and S. Pillai, "Harnessing plasmonics for solar cells," *Nature Photonics*, Vol. 6, No. 3, pp. 130 – 132, Mar. 2012. [Online]. Available: http://dx.doi.org/10.1038/nphoton.2012.30

[29] P. Reineck, G. P. Lee, D. Brick, M. Karg, P. Mulvaney, and U. Bach, "A solid-state plasmonic solar cell via metal nanoparticle self-assembly," *Advanced Materials*, Vol. 24, No. 35, pp. 4750–4755, 2012. [Online]. Available: http://dx.doi.org/10.1002/adma.201200994

[30] V. Myroshnychenko, J. Nelayah, G. Adamo, N. Geuquet, J. Rodrguez-Fernndez, I. Pastoriza-Santos, K. F. MacDonald, L. Henrard, L. M. Liz-Marzn, N. I. Zheludev, M. Kociak, and F. J. Garca de Abajo, "Plasmon spectroscopy and imaging of individual gold nanodecahedra: A

combined optical microscopy, cathodoluminescence, and electron energy-loss spectroscopy study," *Nano Letters*, Vol. 12, No. 8, pp. 4172–4180, 2012. [Online]. Available: http://pubs.acs.org/doi/abs/10.1021/nl301742h

[31] E. Boyer-Provera, A. Rossi, L. Oriol, C. Dumontet, A. Plesa, L. Berguiga, J. Elezgaray, A. Arneodo, and F. Argoul, "Wavelet-based decomposition of high resolution surface plasmon microscopy v (z) curves at visible and near infrared wavelengths," *Opt. Express*, Vol. 21, No. 6, pp. 7456–7477, Mar 2013. [Online]. Available: http://www.opticsexpress.org/abstract.cfm?URI=oe-21-6-7456

[32] M. E. Stewart, C. R. Anderton, L. B. Thompson, J. Maria, S. K. Gray, J. A. Rogers, R. G. Nuzzo, *et al.*, "Nanostructured plasmonic sensors," *Chemical reviews*, Vol. 108, No. 2, p. 494, 2008. [Online]. Available: http://rogers.matse.illinois.edu/files/2008/plasmonschemrev.pdf

[33] S. M. Borisov and O. S. Wolfbeis, "Optical biosensors," *Chemical Reviews*, Vol. 106, No. 2, pp. 423–461, 2008. [Online]. Available: http://www.lic.vnu.edu.vn/website/data/scopus/magnetic020.pdf

[34] J. Song, X. Luo, X. Tu, M. K. Park, J. S. Kee, H. Zhang, M. Yu, G.-Q. Lo, and D.-L. Kwong, "Electrical tracing-assisted dual-microring label‑free optical bio/chemical sensors," *Opt. Express*, Vol. 20, No. 4, pp. 4189–4197, Feb 2012. [Online]. Available: http://www.opticsexpress.org/abstract.cfm?URI=oe-20-4-4189

[35] D. K. Gramotnev and S. I. Bozhevolnyi, "Plasmonics beyond the diffraction limit," *Nature Photonics*, Vol. 4, No. 2, pp. 83 – 91, Jan 2010. [Online]. Available: http://dx.doi.org/10.1038/nphoton.2009.282

[36] M. I. Stockman, "Nanoplasmonics: past, present, and glimpse into future," *Opt. Express*, Vol. 19, No. 22, pp. 22 029–22 106, Oct 2011. [Online]. Available: http://www.opticsexpress.org/abstract.cfm?URI=oe-19-22-22029

[37] P. Mühlschlegel, H. Eisler, O. J. F. Martin, B. Hecht, and D. W. Pohl, "Resonant Optical Antennas," *Science*, Vol. 308, pp. 1607–1609, June 2005. [Online]. Available: http://www.sciencemag.org/content/308/5728/1607.abstract

[38] S. A. Maier, *Plasmonics: Fundamentals and Applications*. NY, USA: Springer, 2007.

[39] L. Novotny and N. van Hulst, "Antennas for light," *Nature Photonics*, Vol. 5, No. 2, pp. 83 – 90, 2012. [Online]. Available: http://dx.doi.org/10.1038/nphoton.2010.237

[40] L. Novotny, "Effective wavelength scaling for optical antennas," *Phys. Rev. Lett.*, Vol. 98, No. 26, p. 266802, Jun 2007. [Online]. Available: http://link.aps.org/doi/10.1103/PhysRevLett.98.266802

[41] F. Neubrech, T. Kolb, R. Lovrincic, G. Fahsold, A. Pucci, J. Aizpurua, T. W. Cornelius, M. E. Toimil-Molares, R. Neumann, and S. Karim, "Resonances of individual metal nanowires in the infrared," *Applied Physics Letters*, Vol. 89, No. 25, pp. 253 104 –253 104–3, dec 2006. [Online]. Available: http://link.aip.org/link/?APL/89/253104/1

[42] L. Novotny, "Light propagation and light confinement in near-field optics," PhD. thesis, ETH Zürich, 1996.

[43] D. K. Cheng, *Field and Wave Electromagnetics*, 2nd Ed. Addison Wesley, 1989.

[44] D. J. Griffiths, *Introduction to Electrodynamics (3rd Edition)*. Benjamin Cummings, 1998.

[45] A. Alparslan, *Layered Media Green's Functions: Derivation and Approximation Techniques for all Ranges and Materials*. Saarbrücken: Lampert Publishing, 2011.

[46] C. Hafner, *MaX-1 A Visual Electromagnetics Platform for PCs*. John Wiley, Chichester, 1998.

[47] V. D. Miljkovic, T. Shegai, M. Käll, and P. Johansson, "Mode-specific directional emission from hybridized particle-on-a-film plasmons," *Optics Express*, Vol. 19, No. 14, pp. 12 856–12 864, 2011. [Online]. Available: http://www.opticsexpress.org/abstract.cfm?URI=oe-19-14-12856

[48] OpenMaX, *version 2013A*, 2013. [Online]. Available: http://openmax.ethz.ch/

[49] A. Sommerfeld, *Partial Differential Equations in Physics*, 2nd Ed. New York: Academic Press, 1953.

[50] M. Paulus, P. Gay-Balmaz, and O. J. Martin, "Accurate and efficient computation of the Green's tensor for stratified media," *Physical Review E*, Vol. 62, No. 4, p. 5797, 2000. [Online]. Available: http://link.aps.org/doi/10.1103/PhysRevE.62.5797

[51] A. Alparslan and C. Hafner, "Analysis of photonic structures by the multiple multipole program with complex origin layered geometry Green's functions," *J. Comput. Theor. Nanosci.*, Vol. 9, No. 3, pp. 479–485, Mar. 2012. [Online]. Available: http://www.ingentaconnect.com/content/asp/jctn/2012/00000009/00000003/art00024

[52] K. A. Michalski, "Extrapolation methods for sommerfeld integral tails," *Antennas and Propagation, IEEE Transactions on*, Vol. 46, No. 10, pp. 1405–1418, Oct 1998. [Online]. Available: http://dx.doi.org/10.1109/8.725271

[53] D. C. Fang, J. J. Yang, and G. Y. Delisle, "Discrete image theory for horizontal electric dipoles in a multilayered medium," *Proceedings, IEEE*, Vol. 135, No. 5, pp. 297–303, Oct 1988. [Online]. Available: http://ieeexplore.ieee.org/xpls/abs_all.jsp?arnumber=6720

[54] M. I. Aksun, "A robust approach for the derivation of closed-form Green's functions," *Microwave Theory and Techniques, IEEE Transactions on*, Vol. 44, No. 5, pp. 651–658, May 1996. [Online]. Available: http://dx.doi.org/10.1109/22.493917

[55] C. Tokgoz and G. Dural, "Closed-form Green's functions for cylindrically stratified media," *Microwave Theory and Techniques, IEEE Transactions on*, Vol. 48, No. 1, pp. 40–49, Jan 2000. [Online]. Available: http://dx.doi.org/10.1109/22.817470

[56] A. Alparslan, M. I. Aksun, and K. A. Michalski, "Closed-form Green's functions in planar layered media for all ranges and materials," *Microwave Theory and Techniques, IEEE Transactions on*, Vol. 58, No. 3, pp. 602–613, Mar. 2010. [Online]. Available: http://dx.doi.org/10.1109/TMTT.2010.2040354

[57] E. P. Karabulut, A. T. Erdogan, and M. I. Aksun, "Discrete complex image method with automatic order selection," *Microwave Theory and Techniques, IEEE Transactions on*, Vol. 59, No. 10, pp. 2385–2393, 2011. [Online]. Available: http://dx.doi.org/10.1109/TMTT.2011.2163804

[58] W. C. Chew, *Waves and Fields in Inhomogeneous Media.* New York: Van Nostrand Reinhold, 1990.

[59] N. Kinayman and M. I. Aksun, *Modern Microwave Circuits.* Norwood, MA: Artech House, 2005.

[60] N. Kinayman and M. I. Aksun, "Efficient use of closed-form Green's functions for the analysis of planar geometries with vertical connections," *Microwave Theory and Techniques, IEEE Transactions on*, Vol. 45, No. 5, pp. 593–603, May 1997. [Online]. Available: http://dx.doi.org/10.1109/22.575574

[61] T. Onal, M. I. Aksun, and N. Kinayman, "A rigorous and efficient analysis of 3-D printed circuits: vertical conductors arbitrarily distributed in multilayer environment," *Antennas and Propagaton, IEEE Transactions on*, Vol. 55, No. 12, pp. 3726–3729, Dec 2007. [Online]. Available: http://dx.doi.org/10.1109/TAP.2007.910498

[62] I. Elshafiey, L. Udpa, and S. Udpa, "Scattering from two-dimensional objects embedded in multilayered media," *Magnetics, IEEE Transactions on*, Vol. 30, No. 5, pp. 3160 –3163, sep 1994. [Online]. Available: http://dx.doi.org/10.1109/20.312608

[63] P. Zhou and Q. Li, "Computation electromagnetic scattering in an anisotropic dielectric cylinder by the DDM/FEM/BEM method," in *Computer Modeling and Simulation, 2010. ICCMS '10. Second International Conference on*, Vol. 3, jan. 2010, pp. 412 –415. [Online]. Available: http://ieeexplore.ieee.org/xpls/abs_all.jsp?arnumber=5421255

[64] M. I. Aksun and G. Dural, "Clarification of issues on the closed-form Green's functions in stratified media," *Antennas and Propagation, IEEE Transactions on*, Vol. 53, No. 11, pp. 3644–3653, Nov. 2005. [Online]. Available: http://dx.doi.org/10.1109/TAP.2005.858571

[65] A. Alparslan and M. Aksun, "Thickness dependent behavior of surface plasmon polaritons in layered media," in *Proceedings, PhotonicsGlobal@Singapore*, Dec. 2008, pp. 1–4. [Online]. Available: http://ieeexplore.ieee.org/xpls/abs_all.jsp?arnumber=4781349

[66] P. B. Johnson and R. W. Christy, "Optical constants of the noble metals," *Phys. Rev. B*, Vol. 6, pp. 4370–4379, Dec 1972. [Online]. Available: http://link.aps.org/doi/10.1103/PhysRevB.6.4370

[67] A. Boag and R. Mittra, "Complex multipole beam approach to electromagnetic scattering problems," *Antennas and Propagation, IEEE Transactions on*, Vol. 42, No. 3, pp. 366 –372, mar 1994. [Online]. Available: http://dx.doi.org/10.1109/8.280723

[68] L. B. M. N. Felsen, *Radiation and Scattering of Waves*. John Wiley and Sons, 1994.

[69] C. Hafner, "Beiträge zur berechnung der ausbreitung elektromagnetischer wellen in zylindrischen strukturen mit hilfe des point-matching - verfahrens," PhD. thesis, ETH Zürich, 1980.

[70] C. Hafner, *Generalized multipole technique for computational electromagnetics*, Ser. Artech House Antenna library. Boston, MA: Artech House, 1990.

[71] L. H. Bomholt, "MMP-3D : a computer code for electromagnetic scattering based on the GMT," PhD. thesis, ETH Zürich, 1990.

[72] J. Fröhlich, "Evolutionary optimization for computational electromagnetics," PhD. thesis, ETH Zürich, 1997.

[73] M. Gnos, "Berechnung statischer, quasistatischer und dynamischer feldprobleme mit MMP," PhD. thesis, ETH Zürich, 1997.

[74] G. Klaus, "3-D streufeldberechnungen mit hilfe der MMP-methode," PhD. thesis, ETH Zürich, 1985.

[75] P. B. Leuchtmann, "Automatisierung der funktionenwahl bei der MMP-methode," PhD. thesis, ETH Zürich, 1987.

[76] E. M. Soriano, "MMP modeling and optimization of photonic crystals, optical devices, and nanostructures," PhD. thesis, ETH Zürich, 2002.

[77] A. Alparslan and C. Hafner, "Using layered geometry Green's functions in the Multiple Multipole Program," *J. Comput. Theor. Nanosci.*, Vol. 8, No. 8, pp. 1600–1608, Aug. 2011. [Online]. Available: http://www.ingentaconnect.com/content/asp/jctn/2011/00000008/00000008/art00033

[78] A. Alparslan and C. Hafner, "Eigenvalue analysis of plasmonic waveguides in layered geometries," *Proc. SPIE 8564, Nanophotonics and Micro/Nano Optics*, pp. 856 416–856 416–7, 2012. [Online]. Available: http://dx.doi.org/10.1117/12.981865

[79] C. Hafner, *2D MMP: Two-Dimensional Multiple Multipole Software and User's Manual*. Artech House, Boston, 1990.

[80] C. Hafner and L. Bomholt, *The 3D Electrodynamic Wave Simulator*. John Wiley, Chichester, 1993.

[81] J. Smajic, C. Hafner, L. Raguin, K. Tavzarashvili, and M. Mishrikey, "Comparison of numerical methods for the analysis of plasmonic structures," *Journal of Computational and Theoretical Nanoscience*, Vol. 6,

No. 3, pp. 763–774, 2009. [Online]. Available: http://www.ingentaconnect.com/content/asp/jctn/2009/00000006/00000003/art00048

[82] J. Hoffmann, C. Hafner, P. Leidenberger, J. Hesselbarth, and S. Burger, "Comparison of electromagnetic field solvers for the 3d analysis of plasmonic nanoantennas," *Proc. SPIE 7390, Modeling Aspects in Optical Metrology II*, pp. 73 900J–73 900J–11, 2009. [Online]. Available: http://dx.doi.org/10.1117/12.828036

[83] C. Hafner and J. Smajic, "Eigenvalue analysis of lossy dispersive waveguides," *Journal of Modern Optics*, Vol. 58, No. 5-6, pp. 467–479, 2011. [Online]. Available: http://www.tandfonline.com/doi/abs/10.1080/09500340.2010.524317

[84] M. Karamehmedović, R. Schuh, V. Schmidt, T. Wriedt, C. Matyssek, W. Hergert, A. Stalmashonak, G. Seifert, and O. Stranik, "Comparison of numerical methods in near-field computation for metallic nanoparticles," *Opt. Express*, Vol. 19, No. 9, pp. 8939–8953, Apr 2011. [Online]. Available: http://www.opticsexpress.org/abstract.cfm?URI=oe-19-9-8939

[85] J. Cooper, V. Hombach, and A. Schiavoni, "Comparison of computational electromagnetic codes applied to a sphere canonical problem," *Microwaves, Antennas and Propagation, IEE Proceedings*, Vol. 143, No. 4, pp. 309–316, Aug. 1996. [Online]. Available: http://dx.doi.org/10.1049/ip-map:19960499

[86] M. Wang, C. Engstrom, K. Schmidt, and C. Hafner, "On high-order fem applied to canonical scattering problems in plasmonics," *Journal of Computational and Theoretical Nanoscience*, Vol. 8, No. 8, pp. 1564–1572, 2011. [Online]. Available: http://www.ingentaconnect.com/content/asp/jctn/2011/00000008/00000008/art00030

[87] P. Leuchtmann, "Automatic computation of optimum origins of the poles in the multiple multipole method (MMP-method)," *Magnetics, IEEE Transactions on*, Vol. 19, No. 6, pp. 2371–2374, 1983. [Online]. Available: http://dx.doi.org/10.1109/TMAG.1983.1062869

[88] E. D. Palik, *Handbook of Optical Constants of Solids: Index*. Academic Press, 1998.

[89] J. D. Jackson, *Classical Electrodynamics*, 3rd Ed. Wiley, Aug. 1998.

[90] J. Smajic and C. Hafner, "Numerical analysis of a snom tip based on a partially cladded optical fiber," *Opt. Express*, Vol. 19,

No. 23, pp. 23 140–23 152, Nov 2011. [Online]. Available: http://www.opticsexpress.org/abstract.cfm?URI=oe-19-23-23140

[91] C. Hafner, "Multiple multipole (MMP) computations of guided waves and waveguide discontinuities," *International Journal of Numerical Modelling: Electronic Networks, Devices and Fields*, Vol. 3, No. 4, pp. 247–257, 1990. [Online]. Available: http://dx.doi.org/10.1002/jnm.1660030405

[92] J. Jin, *The finite element method in electromagnetics.* New York: Wiley, 2002.

[93] A. Taflove and S. C. Hagness, *Computational Electromagnetics: The Finite Difference Time Domain Method*, 3rd Ed. Norwood, MA: Artech House, 2005.

[94] *COMSOL Multiphysics versions 4.2a (Build 4.2.1.166) and 4.3a (Build 4.3.1.161)*, Stockholm, Sweden, 2013. [Online]. Available: http://www.comsol.com

[95] JCMWave, *version 2.6.3*, Berlin, Germany, 2012. [Online]. Available: http://www.jcmwave.com/

[96] H.-G. Beyer and H.-P. Schwefel, "Evolution strategies - a comprehensive introduction," *Natural Computing*, Vol. 1, No. 1, pp. 3–52, 2002. [Online]. Available: http://dx.doi.org/10.1023/A%3A1015059928466

[97] M. Esslinger, "Near-field optical interactions of nano-plasmonic particle assemblies," PhD. thesis, ETH Zürich, 2013. [Online]. Available: http://infoscience.epfl.ch/record/186586/files/EPFL_TH5666.pdf

[98] D. Pozar, *Microwave Engineering, 3Rd Ed.* Wiley India Pvt. Limited, 2009.

List of Publications

Book

P1 A. Alparslan, *Layered Media Green's Functions: Derivation and Approximation Techniques for all Ranges and Materials.* Saarbrücken: Lampert Publishing, 2011.

Journal papers

P2 A. Alparslan and Ch. Hafner, "Eigenvalue analysis of plasmonic waveguides in layered geometries", *in preparation.*

P3 A. Alparslan and Ch. Hafner, "Analysis of photonic structures by the Multiple Multipole Program with complex origin layered geometry Green's functions", *J. Comput. Theor. Nanosci.*, Vol. 9, No. 3, pp. 479–485, Mar. 2012.

P4 A. Alparslan and Ch. Hafner, "Using layered geometry Green's functions in the Multiple Multiple Program", *J. Comput. Theor. Nanosci.*, Vol. 8, No. 8, pp. 1600–1608, Aug. 2011.

P5 A. Alparslan, M. I. Aksun, and K. Michalski, "Closed-form Green's functions in planar layered media for all ranges and materials", *Microwave Theory and Techniques, IEEE Transactions on*, Vol. 58, No. 3, pp. 602–613, Mar. 2010.

P6 M. I. Aksun, A. Alparslan, E. P. Karabulut, E. Erci and V. B. Ertürk, "Determining the effective constitutive parameters of finite periodic structures: photonic crystals and metamaterials", *Microwave Theory and Techniques, IEEE Transactions on*, Vol. 56, No. 6, pp. 1423–1434, Jun. 2008.

Conference & Workshop papers

P7 A. Alparslan and Ch. Hafner, "MMP Analysis of plasmonic structures in layered media: a review", *9th Workshop on Numerical Methods for Optical Nano Structures*, Zürich, Switzerland, Jul. 2013.

P8 M. Wang, K Schmidt, A. Alparslan and Ch. Hafner, "High-order FEM implementation of PML in the study of plasmonic particles in layered media", *9th Workshop on Numerical Methods for Optical Nano Structures*, Zürich, Switzerland, Jul. 2013.

P9 S. Schnepp, J. Niegemann, A. Alparslan and Ch. Hafner, "On the numerical modeling of sharp metallic tips", *4th International Conference from Nanoparticles and Nanomaterials to Nanodevices and Nanosystems*, Corfu, Greece, Jun. 2013.

P10 A. Alparslan and Ch. Hafner, "Analysis of layered media plasmonic waveguides by Multiple Multipole Program", *XXI. Int. Workshop on Optical Wave and Waveguide Theory and Numerical Modeling (OWTNM 2013)*, Enschede, The Netherlands, Apr. 2013.

P11 A. Alparslan and Ch. Hafner, "Eigenvalue analysis of plasmonic waveguides in layered geometries", *SPIE-COS Photonics Asia*, Beijing, China, Nov. 2012.

P12 A. Alparslan and Ch. Hafner, "Analysis of photonic structures in layered geometries by MMP", *Scientific Computing in Electrical Engineering (SCEE2012)*, Zürich, Switzerland, Sep. 2012.

P13 A. Alparslan and Ch. Hafner, "Numerical simulations of plasmonic waveguides in layered media", *8th Workshop on Numerical Methods for Optical Nano Structures*, Zürich, Switzerland, Jul. 2012.

P14 A. Alparslan and Ch. Hafner, "Semi analytical numerical analysis of plasmonic structures in layered geometries", *SPIE Optics + Photonics*, San Diego, USA, Sep. 2011.

P15 A. Alparslan and Ch. Hafner, "Complex origin layered media Green's functions for the MMP analysis of photonic structures", *7th Workshop on Numerical Methods for Optical Nano Structures*, Zürich, Switzerland, Jul. 2011.

P16 A. Alparslan and Ch. Hafner, "Numerical analysis of photonic structures in layered geometries by Multiple Multipole Program", *Workshop on Advanced Techniques in Computational Electromagnetics (ATCEM'11)*, Glasgow, Scotland, Jun. 2011.

P17 A. Alparslan and Ch. Hafner, "Simulating photonic structures in layered geometries by the Multiple Multipole Program", *SPIE Modeling Aspects in Optical Metrology III*, Munich, Germany, May 2011.

P18 A. Alparslan and Ch. Hafner, "Using layered media Green's Functions in the Multiple Multipole Method for optical applications", *IV LEMA-EPFL Workshop on Integral Techniques for Electromagnetics*, Les Diablerets, Switzerland, Oct. 2010.

P19 A. Alparslan and Ch. Hafner, "Layered media Green's functions: a new expansion for OpenMaX", *6th Workshop on Numerical Methods for Optical Nano Structures*, Zürich, Switzerland, Jul. 2010.

P20 M. I. Aksun, A. Alparslan and K. A. Michalski, "Current Status of closed-form Greens functions in layered media composed of natural and artificial materials", *Electromagnetics in Advanced Applications 2009. ICEAA '09*, Torino, Italy, Sep. 2009.

P21 A. Alparslan, M. I. Aksun and K. A. Michalski, "Closed-form Greens functions in planar layered media for all ranges and materials", *III LEMA-EPFL Workshop on Integral Techniques for Electromagnetics*, Istanbul, Turkey, Sep. 2009.

P22 A. Alparslan, "Application of closed-form Green's functions with special emphasis on wave constituents", *5th Workshop on Numerical Methods for Optical Nano Structures*, Zürich, Switzerland, Jul. 2009.

P23 A. Alparslan and M. I. Aksun, "Thickness dependent behavior of surface plasmon polaritons in layered media", *IEEE Photonics Global*, Singapore, Singapore, Dec. 2008.

P24 M. I. Aksun, A. Alparslan and K. A. Michalski, "Study of Green's functions in layered media composed of right-handed, left-handed materials and metals", *III LEMA-EPFL Workshop on Integral Techniques for Electromagnetics*, Chiclana de la Frontera, Spain, Oct. 2008.

P25 K. A. Michalski, M. I. Aksun and A. Alparslan, "Recent progress in the development of the closed-form Green's functions", *III LEMA-EPFL Workshop on Integral Techniques for Electromagnetics*, Chiclana de la Frontera, Spain, Oct. 2008.

P26 A. Alparslan, "Thickness dependent behavior of surface waves in layered media", *4th Workshop on Numerical Methods for Optical Nano Structures*, Zürich, Switzerland, Jul., 2008.

Curriculum Vitae

Personal data

Name:	Aytaç Alparslan
Nationality:	Turkish
Date of birth:	January 23, 1983
E-mail:	aalparslan@gmail.com

Education

2008 – present:	**ETH Zurich**, Zurich, Switzerland Laboratory for Electromagnetic Fields and Microwave Electronics PhD., Doctor of Science, ETH Zürich *Analysis of nano structures in layered geometries* (PhD thesis)
2006 – 2008:	**Koç University**, Istanbul, Turkey Departement of Electrical and Electronics Enginnering M.S. in Electrical and Computer Engineering *Study of Green's functions of potentials and fields in layeres media composed of left-handed and right-handed materials* (Master thesis)
2001 – 2006:	**Koç University**, Istanbul, Turkey Departement of Electrical and Electronics Enginnering B.S. in Electrical and Electronics Engineering
1998 – 2001:	**Çanakkale Scientific High School**, Çanakkale, Turkey

Work and Academic Experience

2008 – present:	**ETH Zurich**, Zurich, Switzerland Laboratory for Electromagnetic Fields and Microwave Electronics Research and teaching Assistant
2006 – 2008:	**Koç University**, Istanbul, Turkey Departement of Electrical and Electronics Enginnering Research and teaching assistant